RVC-2001

Quad-plane Design for Autonomous Cargo Delivery

A Major Qualifying Project Report
Submitted to the Faculty of the
WORCESTER POLYTECHNIC INSTITUTE
In Partial Fulfillment of the Requirements for the
Degree of Bachelor of Science
in Aerospace Engineering

By
Duncan Driscoll

x Duncan Driscoll

Brian Ferrarotti

x Brian Ferrarotti

Jason Karlin

x

Rushab Patil

x Rushab Patil

April 5, 2020

Approved by: _____

Raghvendra V. Cowlagi, Advisor
Professor, Aerospace Engineering Program
WPI

Abstract

WPI-AE conducted a cargo delivery aircraft design competition in which this project participated. The competition rules provided design requirements, constraints, and performance metrics. The design was required to have electric propulsion and vertical take-off and landing (VTOL) capability. The constraints included a total weight limit of 3kg, an onboard power limit of 1000 W, and an onboard battery energy limit of 2200 mAh. The performance metrics were based on the weight of cargo payload, accuracy of delivery, duration of flight, and autonomy.

This report discusses the design, analysis, construction, and flight testing of an aircraft that conforms to the competition rules. For VTOL capability, the aircraft is a fixed-wing/quadrotor hybrid design with a wingspan of 1.54m. A fifth rotor in pusher configuration provides thrust during flight in the fixed-wing mode. The aircraft wing is constructed using expanded polystyrene foam with a carbon fiber spar, with a 3D-printed fuselage and wind-body linkages. Onboard autonomy is achieved using optical- and depth sensors and the ArduPilot off-the-shelf autopilot. The autopilot is implemented on a PixHawk Pix32 microcontroller, which includes an inertial measurement unit and a GPS receiver. Higher level autonomous capabilities including vision-based target detection and guidance are implemented on a NVidia Jetson Nano single-board computer. Analysis of the aircraft's aerodynamic and structural properties are conducted using the XFLR5 and SolidWorks software packages, respectively. Simulation of the aircraft's performance is developed using MATLAB. Whereas the final competition was cancelled due to unavoidable circumstances, preliminary flight tests were conducted, and are discussed in this report. Simulated flights indicated that the designed aircraft achieves high performance via accurate delivery and autonomy.

Acknowledgments

This project would not have been possible without the help of several important people.

Zachary Zolotarevsky, who's insight from his work on the 2019 VTOL MQP was an invaluable source of guidance for this project.

Professor Raghvendra Cowlagi, for his constant support that helped keep the project on schedule.

The Millis RC club, for allowing us to perform flight tests on their field and for giving suggestions on future changes.

Table of Authorship

Chapter	Technical Work	Writing
Chapter 1: Background and Introduction		
Section 1.1: Literature Review	All	JK, BF, RP
Section 1.2: Project Goals		JK
Section 1.3: Project Design Requirements, Constraints and Other Considerations		JK, RP
Section 1.4: Project Management		All
Section 1.5: Project Broader Impact		JK
Chapter 2: System Design		
Section 2.1: Mission and Simulation	BF	BF
Section 2.2: Aerodynamics and Structures	JK, DD	JK, DD
Section 2.3: Autonomy and Control	RP	RP
Section 2.4: Power and Propulsion	JK, RP	JK, RP
Chapter 3: Design Analysis		
Section 3.1: Mission and Simulation	BF	BF
Section 3.2: Aerodynamics and Structures	All	JK, DD, BF
Section 3.3: Autonomy and Control	RP	RP
Section 3.4: Power and Propulsion	JK, RP	JK, RP
Chapter 4: Experimental Results		
Section 4.1: Glide Testing	All	RP, JK
Section 4.2: Design Modifications	All	BF, JK
Section 4.3: Bench Testing	RP	JK
Section 4.4: Flight Testing	JK, RP, BF	BF, JK
Section 4.5: Conclusions		All
Section 4.6: Recommendations for Future Work		BF, JK

Chapter 5: References		All
Appendices		
Appendix A: Power Draw Estimates	BF	RP, BF
Appendix B: 2020 WPI UAV Competition Rules		
Appendix C: Hover Test Information	JK, RP, BF	JK
Appendix D: Bench Test Information	JK, RP	JK

Contents

Table of Figures

Table of Tables

1. Background and Introduction

The purpose of this project was to design and manufacture an aircraft to compete in the Worcester Polytechnic Institute (WPI) 2020 Unmanned Aerial Vehicle (UAV) Competition. This competition presented the challenge of designing an aircraft that can take off and deliver a payload to a target area. In recent years, delivery companies and retail stores have researched using vertical takeoff and landing (VTOL) aircraft for package delivery (Xu, 2017). Current quadcopters used for package delivery have limited range (Lin et al. 2018). The final design selected was an autonomous quad-plane, an aircraft that is a combination of a quadcopter and a fixed-wing aircraft (ArduPilot, 2019). This would take advantage of fixed wing flight to increase the range and the quadcopter ability to take off/land from a confined area.

1.1. Literature Review

Several designs for VTOL UAVs were explored. The two most common mechanisms for VTOL are tail lift and belly lift aircraft. Tail lift aircraft take off vertically from landing legs in the rear of the aircraft and transition to horizontal flight by pitching forward. Belly lift aircraft take off horizontally and transition to horizontal flight without a maneuver (Waterman et al. 2019). It was decided that due to the unstable transition from vertical to horizontal flight, tail lift aircraft were unfavorable to build (Waterman et al, 2019). This project focused on belly lift aircraft. Some design configurations used to implement belly lift are the quadcopter, tiltrotor, and quad-plane. Several commercial VTOL UAVs that used belly mechanism were researched as a basis for this project's design.

1.1.1 Quadcopters

Quadcopters achieve VTOL with a set of fixed vertical motors, usually with no airfoils to aid in horizontal motion. This results in a simple design that is not capable of high endurance flights. One such VTOL UAV used for package delivery is the Icelandic company's Aha, depicted in Figure 1. By modifying a commercially available DJI quadcopter with Global Positioning System (GPS) trackers, the company has been able to significantly reduce food delivery times to locations across the city of Reykjavik (Ross, 2018). These vehicles lack

cameras or the ability to actively avoid obstacles, requiring the company to limit their initial delivery locations and constantly survey the city to ensure new construction does not interfere with their routes (Ross, 2018).

Figure 1: A Flytrex delivery UAV used by AHA (Flytrex)

1.1.2 Tiltrotor aircraft

The DHL Parcelcopter 4.0 is intended for situations that mesh poorly with established infrastructures or where standard delivery methods are unfeasible (DHL ParcelCopter, 2019). This aircraft is depicted in Figure 2. Natural barriers, like mountains and water bodies, do not restrict airborne deliveries. DHL Parcelcopter is designed to improve the lives of inhabitants in remote areas. To cover the maximum area possible, the current Parcelcopter utilizes tiltrotors and fixed wings to achieve a range of 65 kilometers. This range is significantly larger than that of its predecessors, which had a range from 1 km to 8.3 km (DHL ParcelCopter, 2019).

Figure 2: The DHL ParcelCopter (DHL ParcelCopter, 2019)

Uber Eats has designed a hexa-copter design with VTOL capabilities. This aircraft has a range of 18 miles and a flight time of 18 minutes. The aircraft uses a tilt-rotor mechanism to transition from vertical to horizontal flight and is depicted in Figure 3.

Figure 3: UberEats delivery drone (TechCrunch, 2019)

1.1.3 Quad-planes

The Alphabet Wing is a commercial VTOL fixed wing UAV depicted in Figure 4. Initially a GoogleX project, the Wing became an independent business, offering customers their aircraft for delivery purposes (Wing, 2019**)**. Seeing a need to develop a flexible delivery service, the project created an autonomous delivery UAV to increase access to goods, reduce traffic in cities, and reduce CO2 emissions attributed to delivery services (Wing, 2019). The design uses twelve motors for VTOL flight and two counter-rotating motors for horizontal flight. This design has an innovative payload carrying mechanism that allows the payload to be partially tucked up into the airframe of the aircraft, thus reducing payload movement in flight. Its fixed wing allows it to take advantage of aerodynamic forces to reduce battery drain in the cruise leg of its mission.

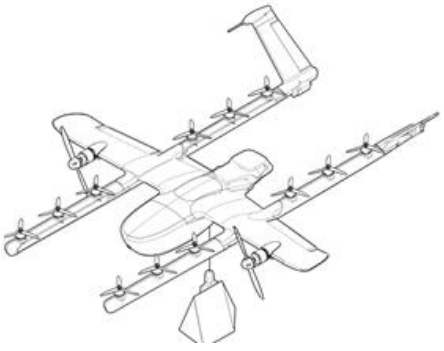

Figure 4: Alphabet Wing (Wing, 2019)

Another design for commercial use is the ALTI Ascend, shown in Figure 5. This aircraft was designed to have long-endurance flight, a modular payload bay, achieve autonomous flight, and to conduct payload delivery. The ALTI Ascend can also be used for surveillance and surveying. Like the Alphabet Wing, ALTI has developed a VTOL design based off a quadcopter design, using four vertical motors and one horizontal gas-powered motor and wingtips to decrease drag (ALTI, 2019). To enable the aircraft's use in difficult to reach locations, ALTI can be assembled and flown within ten minutes of arriving onsite to a location. In addition, the aircraft can take off in a 4-meter by 6-meter area.

Figure 5: The ALTI Ascend (ALTI, 2019)

1.1.4 Tail Lift Aircraft

Wingtra is a fixed winged aircraft utilizing the tail lift configuration to achieve VTOL capabilities, seen in Figure 6. It does a pitching maneuver after takeoff to transition to horizontal flight. By using two motors for both flight modes, Wingtra is able to reduce the weight of the overall aircraft.

Figure 6. The Wingtra VTOL UAV (Wingtra, 2019)

1.1.5 Other Delivery Aircraft

Even if they lack VTOL capabilities, some other UAV designs have had success in package delivery. Zipline is one of the most established UAV delivery networks with over 25,000 successful deliveries as of December 2019 (Zipline, 2019). Zipline's UAVs are fixed wing aircrafts designed for autonomous flight, precision delivery, and to achieve long range (see Figure 7). Zipline's aircraft does not have VTOL capabilities, but unique factors like modular electronics reduce the average assembly time to 5 minutes. Zipline's delivery service was launched in Rwanda in 2016 and is fulfilling deliveries on a regular basis (Zipline, 2019).

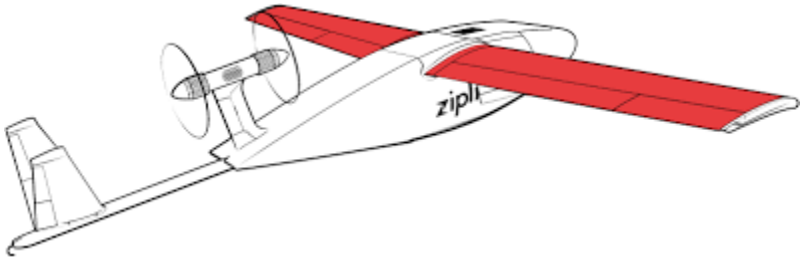

Figure 7: The Zipline Delivery UAV (Zipline, 2019)

1.2. Project Goals

The goal of this project was to develop and construct an aircraft to partake in the 2020 WPI UAV Competition and achieve a high score. The rules for this competition are contained in Appendix B: 2020 WPI UAV Competition Rules. This goal was divided into several design objectives.

1. Maximize score from autonomy points.
2. Maximize score from the payload to weight fraction.
3. Increase score by maximizing endurance (flight time).

Autonomous capabilities were divided in the competition rules into five parts: autopilot, waypoint guidance, no-fly zone avoidance, target detection, and payload drop. Due to the necessity of carrying additional motors and increased power consumption to conduct VTOL instead of a conventional takeoff and landing, autonomy was determined to be the most effective way to maximize overall score. To gain these points the aircraft was designed to have the ability to conduct each leg of the mission autonomously.

After autonomy, the focus of the team was to develop an aircraft with a high payload to empty weight ratio. The gross takeoff weight of the aircraft was limited and it was desired to carry as much payload as possible. As a result, the payload the aircraft could carry was dependent on the empty weight of the aircraft. Lastly, the team focused on creating an aircraft with a longer flight time. This was due to part of the score being proportional to the product of payload fraction and flight time.

1.3. Project Design Requirements, Constraints and Other Considerations

The 2020 WPI UAV Competition required the takeoff from a specified area, maintained flight for a certain time period, delivering a payload to a target location, and then landing within the original takeoff area (2020 WPI UAV). The WPI 2020 UAV Competition outlined several constraints that must be met for the aircraft to be eligible for the competition. These constraints are as follows:

1. The maximum power that can be used by the aircraft is limited to 1000 watts.
2. The aircraft must be able to avoid a no-fly zone and other obstacles during its flight.
3. The mass of the aircraft and payload must not exceed 3 kilograms.
4. Battery selection is limited to a 2200 mAh, 3 cell battery.

Each action conducted during the flight was assigned a point value that determined the final score through Equation (1).

$$Score = \lambda_1 \frac{w_{payload}}{w_{empty}} t_{flight} v_{avg} + \lambda_2 \Delta + \lambda_3 \sum_n A_n + P \quad (1)$$

The first term of the scoring equation represented the ratio of payload weight to empty weight of the aircraft, the time of flight and average velocity. The second term described the points awarded depending on the drop accuracy of the payload. The summation of points awarded by autonomy is described by the third term, and the points awarded by originality described by the final term. The variables in Equation (1) are described in Table 1.

Table 1: Variables in the scoring equation

Variable	Description
λ_i	Constants; $\lambda_1 = 0.01$, $\lambda_2 = 3$, and $\lambda_3 = 35$
$W_{payload}$	Weight of the payload carried by the aircraft, N
W_{empty}	Weight of the aircraft without payload, N
t_{flight}	Time of flight from take-off to payload drop, s
v_{avg}	Average groundspeed of the aircraft during flight, m/s
Δ	Defined by δ, the distance between the target location and actual payload drop point: $\Delta = \begin{cases} 1 & 0 < \delta < 1\ m \\ 0 & 1\ m \leq \delta \leq 3.5\ m \\ -1 & 3.5\ m < \delta \end{cases}$
A_n	Points for successfully demonstrating autonomy capability n $A_1 = A_2 = A_5 = 1$ $A_3 = 3$ $A_4 = 5$
P	Originality score, on a scale from 0 to 10

1.4. Project Management

The main tasks of the project were divided into several sections: Structures and Aerodynamics, Power and Propulsion, and Control and Autonomy. Each team member was assigned to two sections. During the first term, team members conducted research in their respective areas and gave weekly updates to the rest of the team. Presentations were given weekly to update the advisor, Professor Cowlagi, on the status of the project. Each team member updated the presentations with their own work.

Duncan continuously revised the SolidWorks® assembly. This led to a 1:1 realistic model that would be referenced during the final UAV's construction. The fuselage was designed around the circuit design and models of the components. With dimensions referenced by an external text file, he was able to update changes to the parametric assembly while balancing the motors around the center of gravity. He was also responsible for placing orders for components and ensuring that everything could be 3D printed and assembled correctly.

Brian's work primarily involved developing simulations of the aircraft behavior. This work consisted of developing the mathematical equations and MATLAB® code necessary to estimate the energy consumption of the aircraft during takeoff, transitions to and from horizontal

flight, and landing. Additionally, he performed static and dynamic stability analyses of the aircraft through MATLAB® and XFLR5. As a result, he was the main team member involved in sizing the aircraft's tail. He also assisted with the fabrication of some of the components for the glide test prototype and final aircraft.

Jason was responsible for aerodynamics, power and propulsion. This work entailed selecting the airfoil used for the aircraft using historical data and XFLR5, planning and conducting the wind tunnel test, and building the wing for the aircraft. Jason built a scale model of the aircraft and test bed for electronic testing. He was also responsible for comparing a variety of motors and selected one type of motor to be used for the aircraft. Jason also conducted research on batteries and selected the battery to be used on the aircraft. During C term, Jason cut the foam wings used on the final design of the aircraft. He helped to assemble the final aircraft and modify the internal arrangement of electronics. Jason also helped with verifying the stability calculations done by Brian. In addition, Jason assisted with several flight tests and bench tests of onboard systems.

Rushab was responsible for stability, control, and autonomy of the aircraft. He designed a system architecture and mission plan that explained how the hardware and software worked coherently to achieve the objectives. He also finalized the avionics of the aircraft and continuously updated the circuit design to accommodate the new features or components in the aircraft design. Rushab worked with Duncan on the fuselage design to accommodate electronic circuit design. He was also responsible for designing the aircraft control surfaces, using MATLAB® for the control surface sizing analysis. He assisted the team with the manufacturing and assembling the scale model, glide test model, and final models. Rushab also assembled and fabricated, if necessary, the parts required for electronic circuits on the aircraft. He was the primary team member performing bench tests of the electronics an embedded system to ensure the autonomy objectives could be satisfied prior to the final assembly of the aircraft.

1.5. Project Broader Impacts

UAVs play an essential role in the economy that will only grow with time. UAVs are divided into two categories, Small and Large, by the Government Accountability Office (GAO). Small UAVs operate below 500 ft in altitude and weigh less than 55 lbs., while Large UAVs operate up to 60,000 ft and weigh more than 55 lbs. Both classes can have two mission types, within visual line of sight and beyond visual line of sight (FAA Continues. 2016). As seen in Figure 8, there are a variety of potential uses for UAVs, from surveying crops, search and rescue missions, and package delivery. Due to their potential uses, United States government agencies have begun to investigate how UAV technology will be integrated into the national airspace.

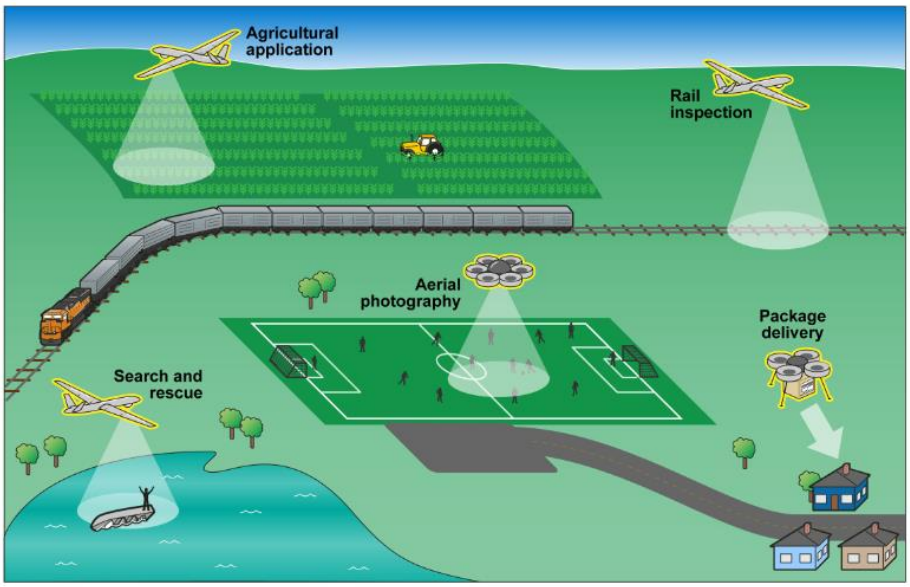

Figure 8: Uses for UAVs (FAA Continues. 2016)

In 2013 the FAA outlined how it would go about integrating unmanned aerial systems (UAS) into the United States' airspace. The three-phased plan consisted of an Accommodation phase, Integration phase, and Evolution phase. The plan begins with creating test areas, validating safety cases, and determining the airworthiness of UAS. The second phase details the need for defining more regulations and establishing standards for UAS. Lastly, the plan called for publishing FAA standards for UAS equipment and having undisrupted UAS operation in the United States' airspace (FAA Continues. 2016).

1.5.1 UAVs for Package Delivery

A major inspiration for the development of UAVs for package delivery is the demand for increasingly short delivery times. Nearly three quarters of surveyed individuals would be somewhat likely to ask for a UAV to deliver their order within an hour of purchase (Connolly. 2016). However, as UAVs do not require a human operator, they can reduce long-term labor costs, which would be beneficial where wages are high. FedEx, Amazon, and DHL have investigated using UAVs for the final stage of delivery (Connolly. 2016). Amazon reports that 85% of its deliveries are packages weighing less than 2.26 kilograms (Keeney. 2015). Keeney, of ARK Investments, found that Amazon has the potential to offer $1 UAV delivery (Keeney. 2015). This assessment was based off predicting the infrastructure, labor, and scaling of the service, which would cost $480 million in the first year. (Keeney. 2015). One potential market is using UAVs to deliver medicine. In 2014, 90% of prescription orders were delivered through mail orders. UAVs could deliver medicine to urban and medically underserved rural areas (Lin et al. 2018).

Package delivering UAVs have the potential to reduce transportation carbon emissions. In 2018, truck transportation contributed nearly a quarter of the greenhouse emissions generated by the United States (Stolaroff et al. 2018). Figure 9 shows a comparison between different modes of transportation and energy used per distance traveled. UAVs have a low energy footprint but are lighter compared to trucks. The type of electrical grid and the proximity of the UAV depots to the delivery points can vary the efficiency of UAV delivery (Stolaroff et al. 2018). Fixed wing aircraft are more energy efficient and can have longer ranges compared to quadcopters. Currently, quadcopters have an average flight time of 10-15 minutes. However, fixed wing aircraft require runways for takeoff and landing. A hybrid design, such as a quad-plane, capable of hovering and fixed wing flight could combine the advantages of quadcopters and fixed wing aircraft.

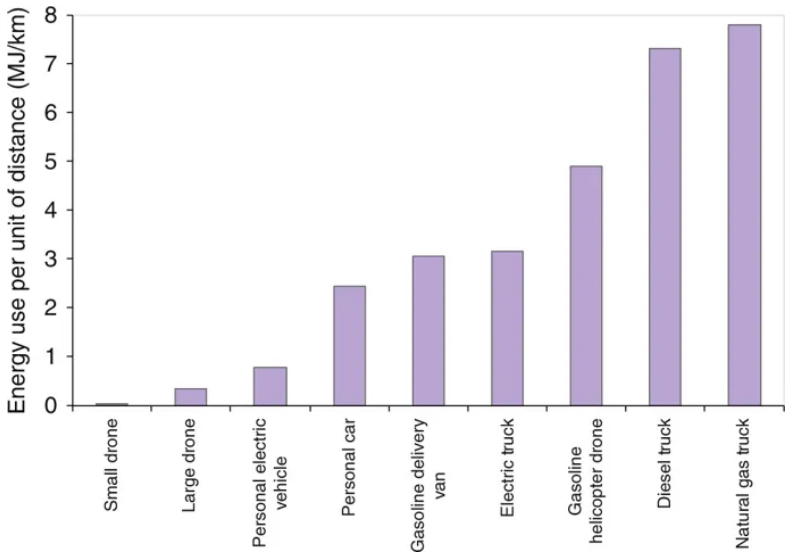

Figure 9: Energy per Distance Traveled (Stolaroff et al. 2018)

1.5.2 UAVs for Aerial Imaging

In addition to delivering payloads, UAVs have been used extensively for their ability to carry cameras to provide a different perspective of the world. Prior to the use of UAVs, companies that desired aerial photographs could primarily source images from either satellites or airplanes. However, while both options can more quickly cover a larger area than UAVs, they are also both significantly more expensive to either purchase or operate, while also having inferior image resolution compared to low-flying UAVs (Price wars, 2020). Thanks to the lower costs of UAVs, both companies and individuals have access to aerial photography on a new scale. This has led to UAVs becoming the foundation for aerial photography service companies. One such company, Drone Base, has conducted over 100,000 flights for customers in over 70 countries (Drone Base, 2020). Due to these advantages, it is expected that UAVs will play a growing role in commercial life.

1.5.3 Challenges

Overall, major questions about the safety of UAS remain. The FAA, over a four-year period ending in 2018, collected 6,117 reports of hazardous uses of UAVs, a majority of which were UAV sightings by pilots near airports and have not included collisions (Small Unmanned, 2018). As the presence of UAVs near airports can cause safety issues and costly delays, the

ability for UAVs to obey no-fly zones is critical as they become more prevalent. A survey found that while the public opinion of delivery UAVs was positive, the potential hazard of malfunctioning UAVs or privacy violations was a common concern amongst the public (Yoo et al. 2018). UAVs must have reliable sensors, navigation, and signal processing to navigate urban and rural terrain. Precipitation could blind sensors, wind could prevent flight or blow a UAV off course (Connolly. 2016). Certifying these systems for reliability has been a major obstacle preventing the proliferation of UAV technology (Chahl. 2015). For UAVs to become more widespread, they must pass rigorous safety tests and become a proven technology.

2. System Design

The final aircraft design is depicted in the SolidWorks® render seen in Figure 10. The aircraft was designed to have five motors, with four vertical motors like a quadcopter and one additional motor for horizontal flight. The aircraft has a rectangular wing. The payload of the aircraft, along with the battery, was carried underneath the fuselage. The wing links, supporting the landing legs and connecting rods for the tail, were 3D printed with PLA. PLA was also used in the wingtips and the motor mounts. Carbon fiber tubes were selected as the support rods for the tail and main wing of the aircraft. The final weight of the designed aircraft was determined using SolidWorks®.

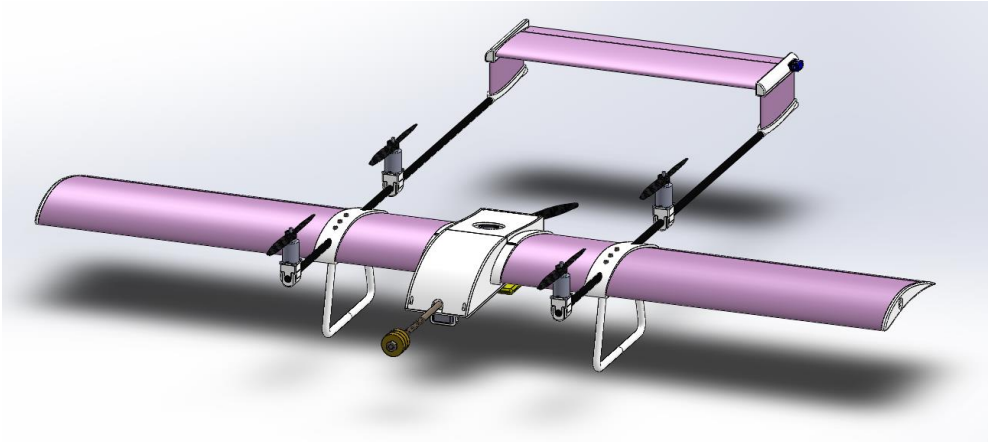

Figure 10: Render of aircraft in SolidWorks®

Figure 11 depicts the final constructed aircraft.

Figure 11: Fully Assembled Aircraft

Front, side, and top views of the aircraft can be seen in Figure 12, Figure 13, and Figure 14 respectively.

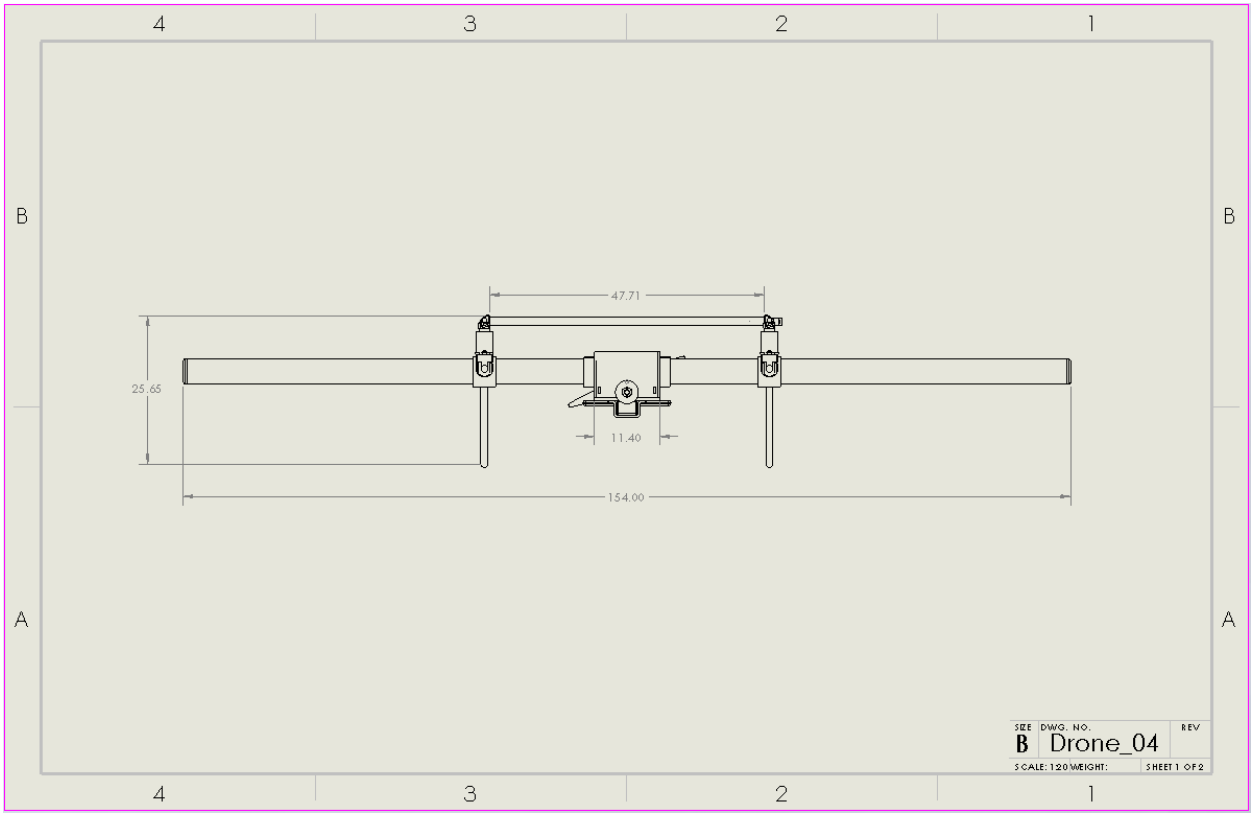

Figure 12: Front view of aircraft

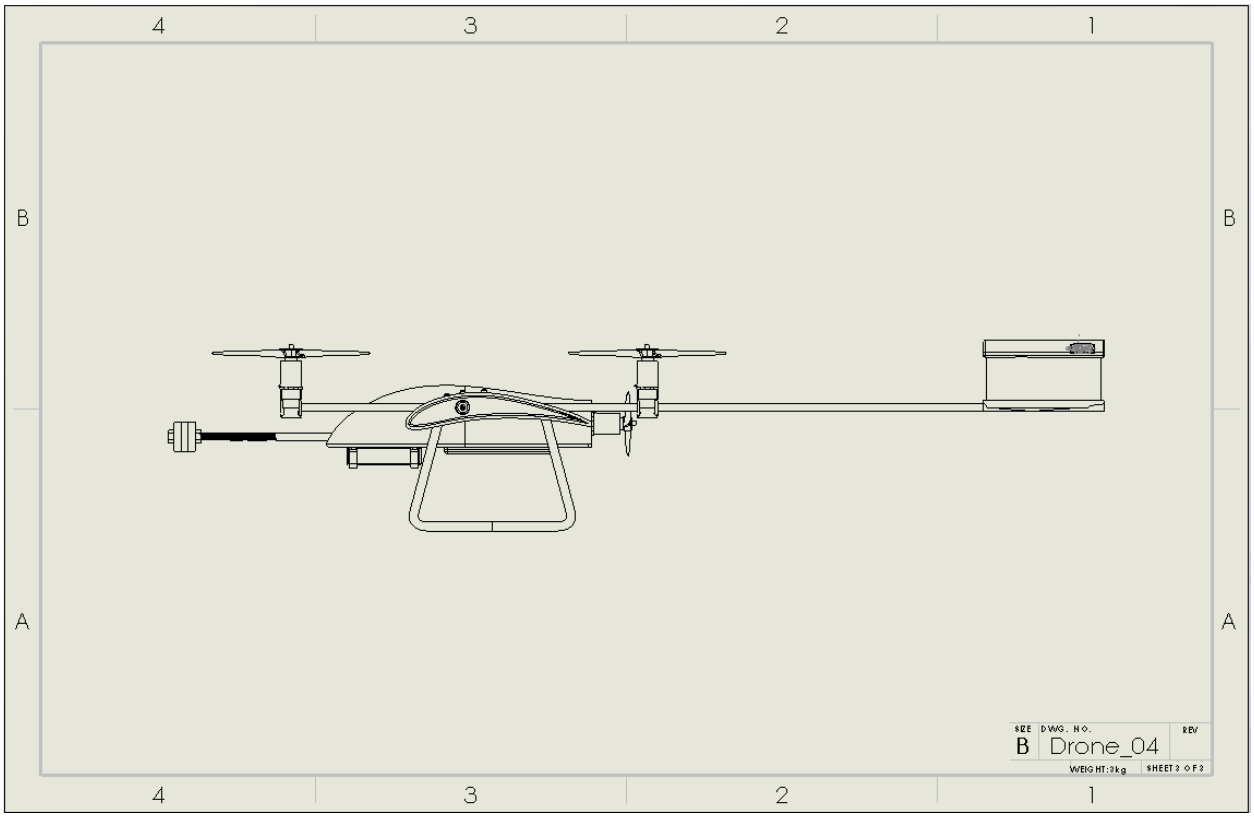

Figure 13: Side view of aircraft

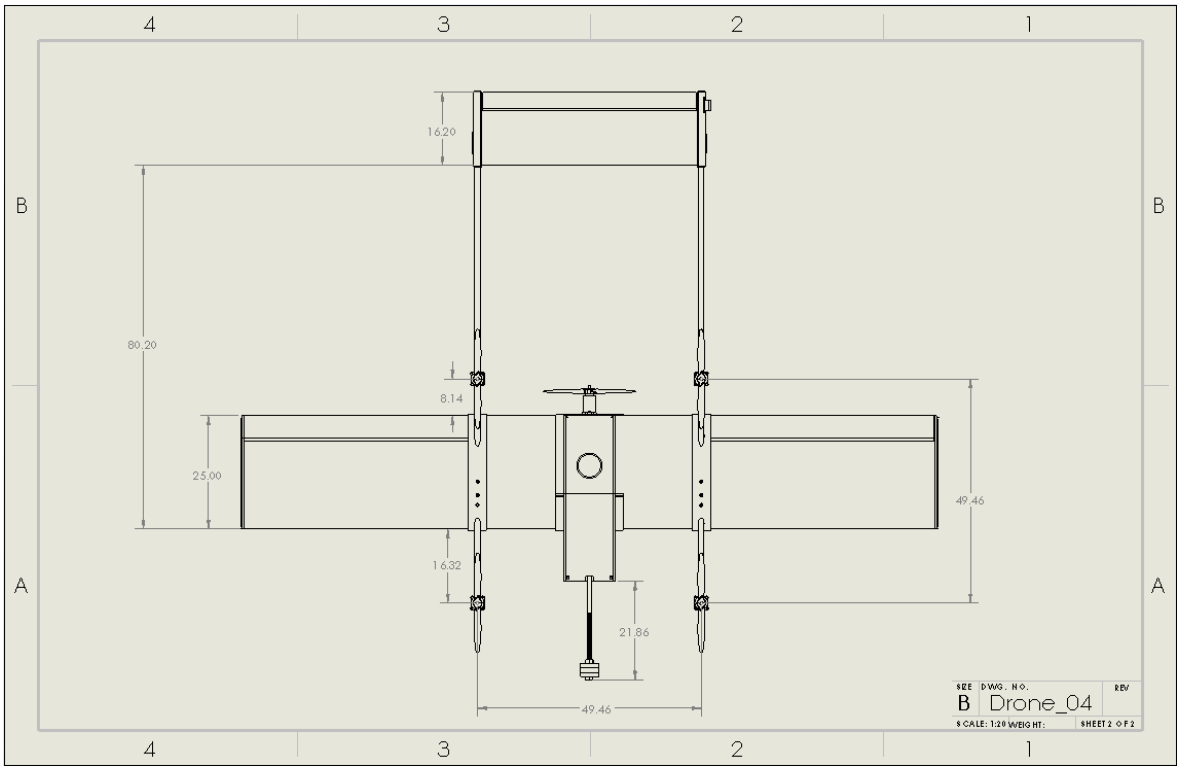

Figure 14: Top view of aircraft

Table 2 lists some of the main design features of the aircraft.

Table 2: Summary of Aircraft Data

Characteristic	Initial Design Items	Final Design Items
Wingspan	1.54 m	1.54 m
Wing Airfoil	E423	E423
Empty Mass	2700 g	2950.00 g
Battery Capacity	2200 mAh	2200mAh
Battery Output (continuous and burst)	45-90 C	45-90 C
Motor	T-Motor AT-2317	T-Motor AT-2317
Motor KV	1400	1400
Propeller	9” x 6”	10” x 6”
Mean Wing Aerodynamic Chord	0.25 m	0.25 m
Static Margin	0.26 m	0.26 m
Moment of Inertia Matrix, Unloaded:	$\begin{bmatrix} 0.1700 & 0.0012 & 0.0128 \\ 0.0012 & 0.2130 & 0.0002 \\ 0.0128 & 0.0002 & 0.3750 \end{bmatrix} kg\ m^2$	$\begin{bmatrix} 0.1700 & 0.0012 & 0.0128 \\ 0.0012 & 0.2130 & 0.0002 \\ 0.0128 & 0.0002 & 0.3750 \end{bmatrix} kg\ m^2$
Loaded:	$\begin{bmatrix} 0.1700 & 0.0012 & 0.0128 \\ 0.0012 & 0.2130 & 0.0002 \\ 0.0128 & 0.0002 & 0.3750 \end{bmatrix} kg\ m^2$	$\begin{bmatrix} 0.1700 & 0.0012 & 0.0128 \\ 0.0012 & 0.2130 & 0.0002 \\ 0.0128 & 0.0002 & 0.3750 \end{bmatrix} kg\ m^2$

Characteristic	Initial Design Items	Final Design Items
Wing Material	Expanded Polystyrene Foam	Expanded Polystyrene Foam
Wing Link Material	PLA	PLA
Wing Tip Material	PLA	PLA
Support Rod Material	Carbon Fiber	Carbon Fiber

The intended layout of the components inside the aircraft's fuselage is depicted in Figure 15. A discussion of these components can be found in Section 2.3.

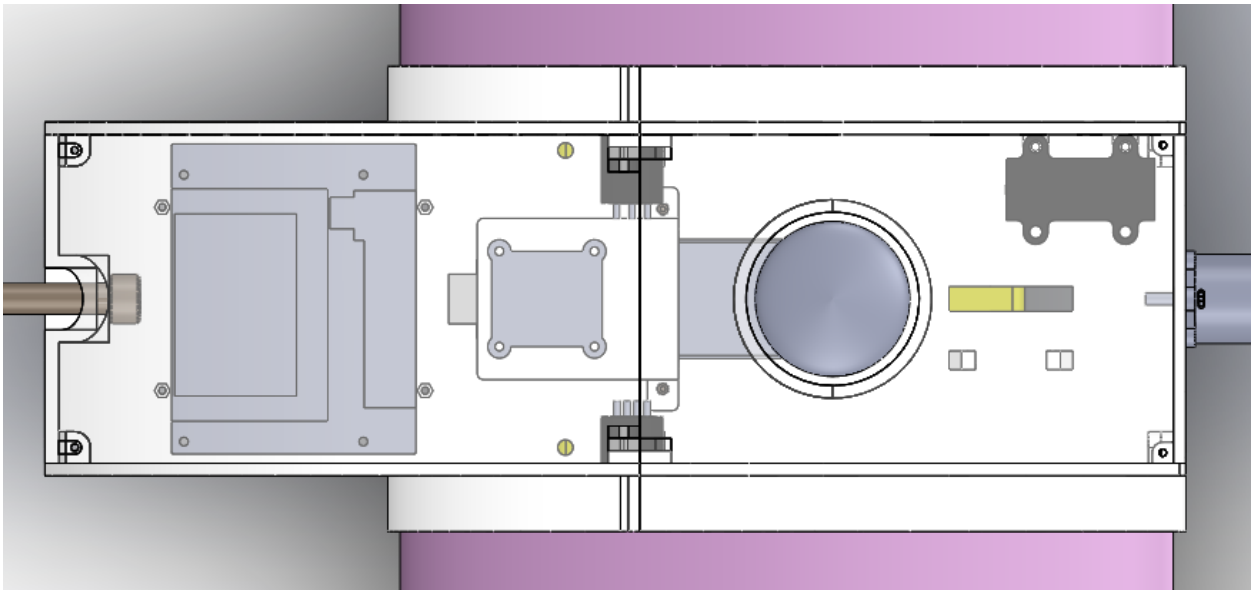

Figure 15: Interior of Aircraft

2.1. Mission and Simulation

The project aircraft was designed to conduct the mission broken up into the legs described in Table 3, with the total aircraft mission seen in Figure 16. The Ardupilot modes are further described in Section 2.3.3.

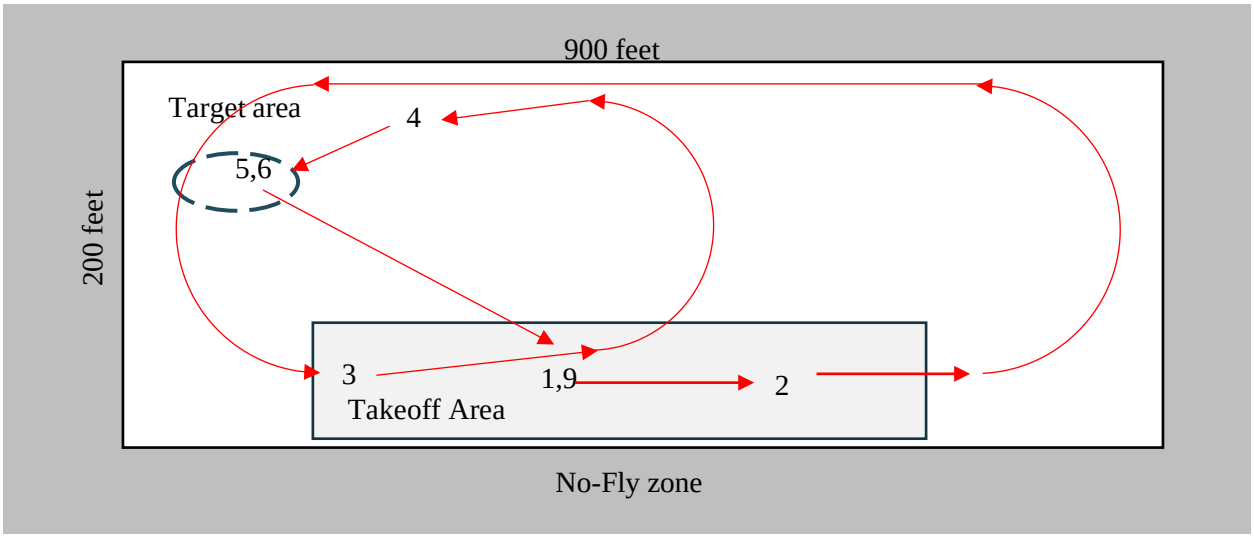

Figure 16: Mission Diagram

Table 3: Flight Leg Description

Flight Leg	Description	Ardupilot Mode
1.	Perform vertical takeoff.	QHOVER
2.	Accelerate horizontally to cruising speed.	FBWA
3.	Fly several laps of the flight zone until the battery has been drained to a predetermined level.	QGUIDED
4.	Fly to the general area of the payload drop zone.	QGUIDED
5.	Decelerate to a hover and locate the exact location of the drop zone.	QGUIDED
6.	Drop the payload.	QGUIDED
7.	Accelerate back to horizontal flight in the direction of the takeoff/landing zone	FBWA
8.	Decelerate to a hover.	FBWA
9.	Perform vertical landing.	QLAND

Additionally, the aircraft was designed to demonstrate the autonomy capabilities listed below.

- Maintain steady flight (in this case maintaining constant altitude and airspeed) during the portions of Leg 3 that do not require turning.
- Navigate through a set of waypoints during Leg 3 of the mission
- Avoid no-fly zones defined by GPS coordinates during Leg 3 of the mission
- Autonomously detect the drop target in Leg 5 of the mission
- Autonomously drop the payload in Leg 6 of the mission

2.2. Aerodynamics and Structures

2.2.1 Aerodynamics

Based on prior literature, several airfoils were selected for comparison. These were the NACA 4412, S1223, E423, MH114, and SD7026 airfoils. The coefficient of lift and moment at a zero angle of attack and varying speeds were calculated using XFLR5. From this, the E423 was selected as the airfoil to be used for the quad-plane wing based on the following analysis. This airfoil is depicted in Figure 17.

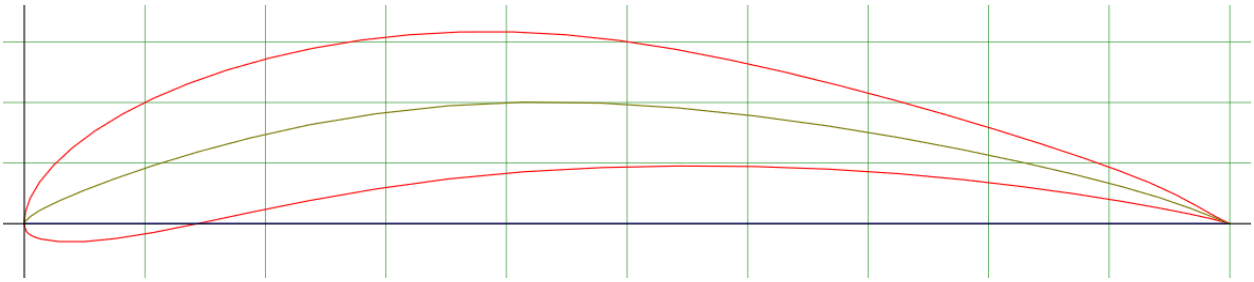

Figure 17. E423 airfoil (Airfoiltools, 2019)

Using XFLR5, the camber, and thickness, a model of each airfoil was created. With these models, the coefficient of lift, coefficient of moment, and coefficient of drag was found for each airfoil. These values were calculated for varying Reynolds numbers to test each airfoil at varying flight speeds. An example of the analysis can be seen below in Table 4, which shows a variety of airfoils at varying cruise speeds assuming a wing chord of 0.25 meters.

Table 4. Airfoil Coefficient of Lifts for Varying Velocities

Airfoil	NACA4412	S1223	E423	MH114	SD7026
10m/s	0.4085	0.7955	0.8607	0.6397	0.3504

Airfoil	NACA4412	S1223	E423	MH114	SD7026
15m/s	0.4164	0.8169	0.8809	0.6572	0.3577
20m/s	0.4220	0.8330	0.8978	0.6719	0.3629
25m/s	0.4261	0.8450	0.9117	0.6839	0.3667

This information, in addition to moment data and maximum coefficient of lift data, was added to a MATLAB® script for future analysis. Due to their high lift coefficients, S1223, E423 and MH114 were examined further. Using data from XFLR5, several plots were made to compare each airfoil's characteristics at 15m/s, which are shown in Figure 18. E423 was selected for the final wing due to its high coefficient of lift. Further details on the aerodynamic analysis is discussed in Section 3.2.1.

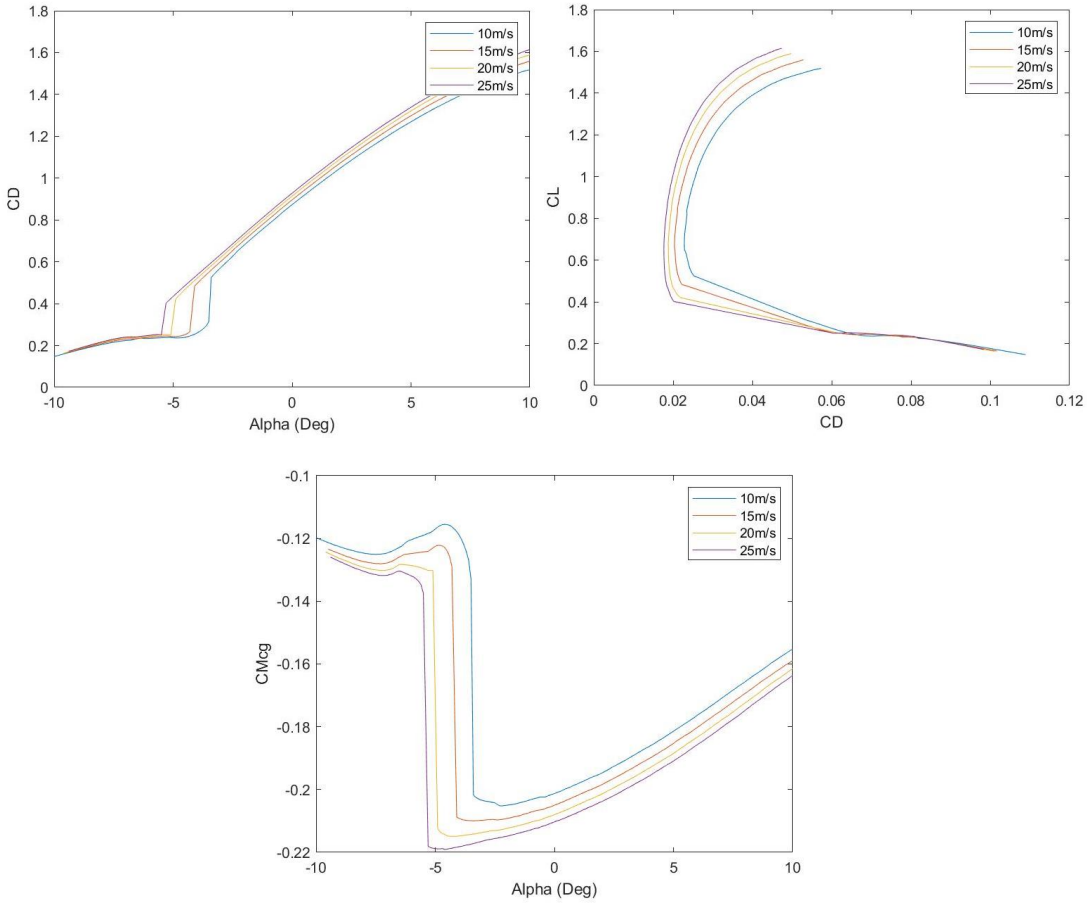

Figure 18. S1223, E423, and MH114 Airfoil Characteristics at 15m/s. Clockwise from top left: plot of lift-to-drag ratios, plot of lift versus angle of attack, plot of moment versus angle of attack

The design constraints for selecting the airfoil was maintaining an aspect ratio between six and eight (Raymer. 2019). With this information, the cruise speed of the aircraft was varied to find different characteristics of the wing at varying speeds. These characteristics are shown in

Table 5. The red rows indicate the values inserted from XFLR5 simulations. For this project, a cruise speed of 12 m/s was selected since this velocity would allow the wing aspect ratio to be close to 6.

Table 5. Characteristics of E423 with a chord of 0.25 m at an angle of attack of 0° at varying cruise velocities

Velocities	V	m/s	10	11	12	15	20	25
Reynold's Number	Re		1.65E+05	1.81E+05	1.98E+05	2.47E+05	3.29E+05	4.12E+05
Max Coef. of Lift	C_{Lmax}		1.449	1.460	1.470	1.493	1.524	1.551
Coef. of Lift	C_L		0.861	0.865	0.865	0.881	0.898	0.912
Wingspan	b	m	2.233	1.836	1.543	0.970	0.535	0.337
Aspect Ratio	AR		8.932	7.343	6.170	3.879	2.141	1.349
Coef. of Drag	C_{di}		0.104	0.128	0.152	0.250	0.471	0.770
Coef. of Moment	C_m		-0.149	-0.15	-0.151	-0.153	-0.155	-0.157
Span Loading	SL	N/m	13.180	16.032	19.080	30.350	54.990	87.253
Induced Drag	D_i	N	0.90	1.10	1.31	2.13	3.93	6.33
Stall Speed	V_{stall}	m/s	7.71	8.47	9.20	11.5	15.3	19.2
Lift to Drag Ratio	L/D		32.6	26.6	22.4	13.8	7.49	4.65
Power	P	W	9.03	12.1	15.8	31.9	78.6	158
Wing Area	S	m^2	0.558	0.459	0.386	0.242	0.134	0.084
Required Thrust to Weight Ratio	T/W		3.07E-02	3.75E-02	4.47E-02	7.23E-02	1.34E-01	2.15E-01
Wing Loading Factor	W/S	N/m^2	52.718	64.130	76.320	121.399	219.961	349.010

After selecting the E423 as the main airfoil for the project, a 3D printed model was created for wind tunnel testing. The size of the testing area was 2 feet (0.6096 m) wide by 2 feet tall, with the wind tunnel having a maximum speed of 55m/s. Therefor the airfoil was scaled down to have a span of 0.431 m and a chord of 0.07 m, with a flight speed of 43 m/s needed to ensure a Reynolds number of $1.98 * 10^5$, the same as the full sized wing. The results were plotted against the theoretically determined expected values of the test, determined using the

XFLR5 data and moment calculated about the leading edge to the connection point of the wing to the test rig (see Figure 19). Testing found that the experimental lift and moment were higher than the theoretically calculated values. This may be due to the instability of the testing bed, which tilted up at higher speeds.

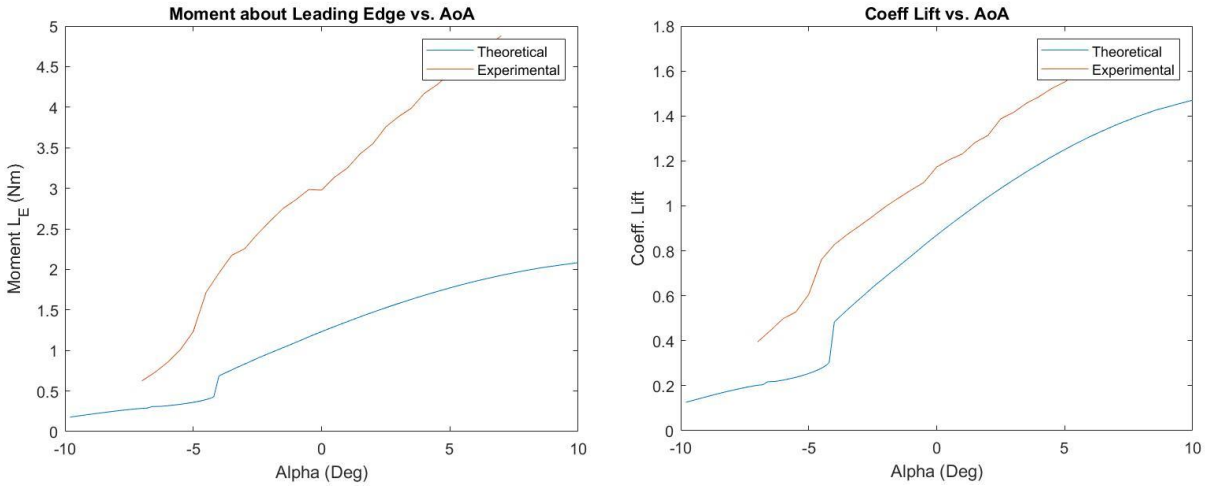

Figure 19: Wind Tunnel Test Data Compared to Theoretical Calculations

2.2.2 Structures

The project team selected a rectangular wing with a constant chord for the aircraft. Compared to a tapered wing, this simplified construction of the aircraft. Expanded polystyrene was chosen as the material of the aircraft's wings. These wings would be supported by carbon fiber tubes inside the wings. This design avoided the use of ribs and curved wing tips, reducing the time required to build the wing during assembly and reduced the overall weight of the empty aircraft. In order to manufacture the complex designs of parts such as the wing links and landing gear, these parts were 3D printed with PLA with a low infill percentage. This minimized the empty space within the fuselage while properly positioning all the mounted equipment. These prints were used to link the foam wings and the tail components to the carbon fiber supports. The fuselage also consists of 10 separate parts that are combined with nuts, bolts, and threaded inserts soldered into 3D prints. Overall, these materials are what contribute to the component masses shown in Table 6, which contains a breakdown of the structural mass of the aircraft.

Table 6: Frame Component Masses

Frame Component	Material Density (g/cm^3)	Quantity	Mass per Component (g)	Net Mass (g)
PLA Fuselage	1.24	1	597	597
Foam Wing Base	0.026	2	22.32	44.64
PLA Wing Link	1.24	2	134	268
Foam Wing Length	0.026	2	57.94	115.88
PLA Wing Straight Tip	1.24	2	24	48
PLA Tail Base	1.24	2	23	46
PLA Tail Corner	1.24	2	29.5	59
Carbon Fiber Front Rod	1.78	2	15.39	30.78
Carbon Fiber Tail Rod	1.78	2	43.76	87.52
Carbon Fiber Wing Support	1.78	2	77.81	155.62
Foam Horizontal Tail	0.026	1	18.23	18.23
Foam Vertical Tail	0.026	2	2.78	5.56
PLA Motor Mount	1.24	4	17.91	71.64
Total Mass				1547.87

Table 7 contains a breakdown of the mass of the loaded aircraft. The total frame mass comes from the summation of parts performed in Table 6.

Table 7 : UAV Hardware Masses

Part	Name	Quantity	Part Mass, g
Frame		1	1547.87
Motors	AT2317	5	101
Propellers	APC 9x6	5	21.38
Microcontroller	Jetson Nano	1	49.7
Flight Controller	Pixhawk Pix32	1	15.8
Power Distribution Board	Airbot PDB	1	10.5
ESCs	Turnigy Multistar	5	9
Battery	Turnigy Nanotech 45-90C	1	201
Altimeter	LeddarOne	1	4
Computer Vision	Raspberry Pi Camera V2	1	3
GPS Module	Pixhawk	1	16.23
BECs 5v	Micro BEC 5v	1	10
Ballast	Counterweight	1	95
Miscellaneous	Fasteners	1	50
Miscellaneous	Wires	1	215
Payload	Beanbags	1	125
Total Mass			3000

2.3. Autonomy and Control

An aircraft achieves autonomy when it accomplishes the mission without any human interference (VTOL MQP, 2019). Autonomy requires sensors that observe the current state of

the aircraft and record changes in its surroundings. There is a variety of hardware required to get this data, process it, and alter the aircraft state to finish the assigned mission. The following subsection gives the overview of the system. Section 3.3 goes over how the software and hardware were selected to work cohesively and achieve all the objectives.

2.3.1 Hardware

Figure 20 depicts the system hardware diagram.

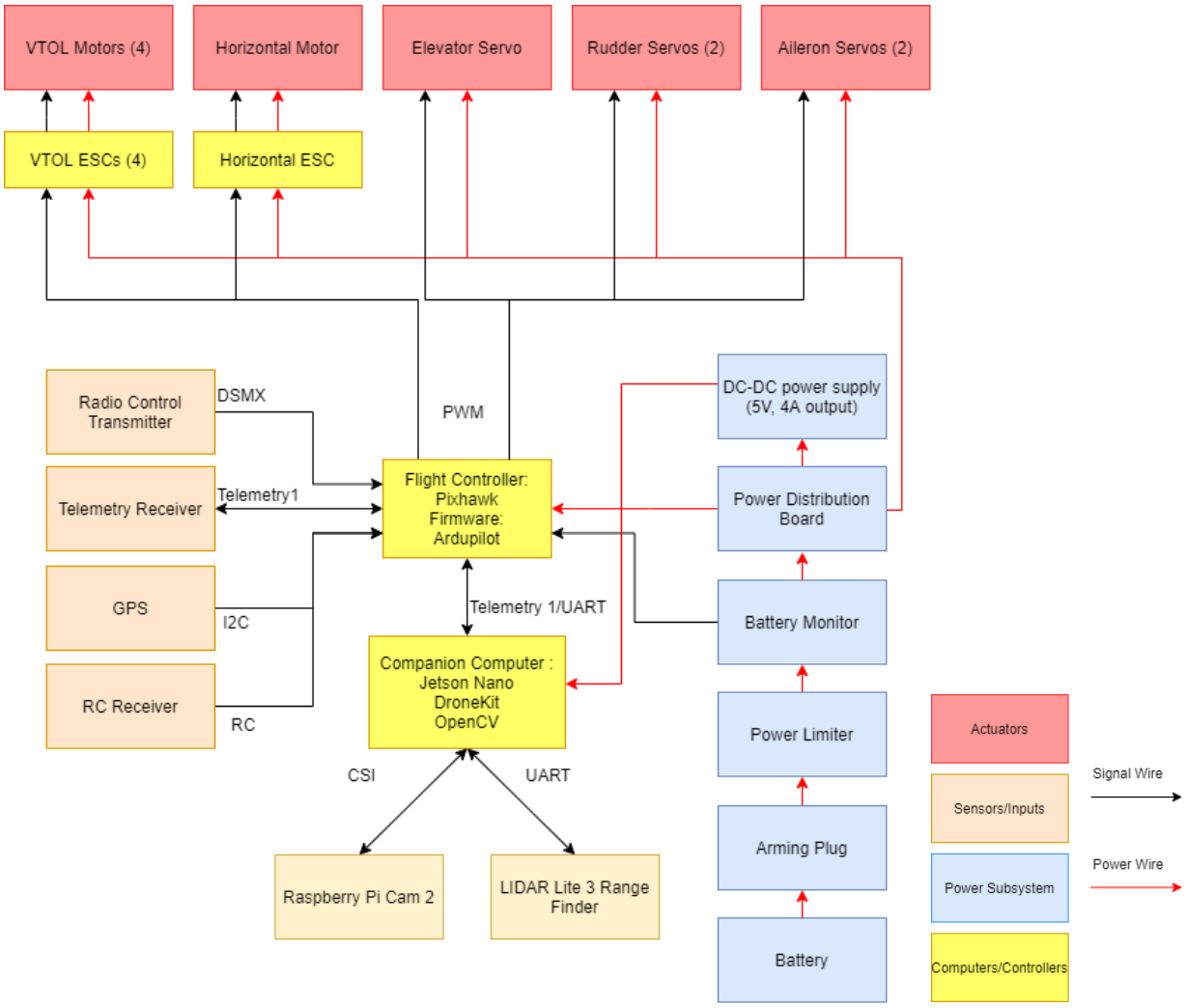

Figure 20: Hardware Flowchart and key

A Pixhawk HkPilot32, depicted in Figure 21, was selected as the flight controller for the autonomous system. This variant was available through the MQP lab, as the VTOL MQP 2019

team used this flight controller, which saved funds compared to buying a new flight controller (VTOL MQP 2019).

Figure 21: Pixhawk HkPilot32 (Holybro, 2019)

Companion computers are used to implement artificial intelligence and robotics technologies with a flight controller. For this project, a Jetson Nano was selected as a companion computer to run computer vision and path planning on board the aircraft. This computer is shown in Figure 22. According to the data from benchmarking tests mentioned in Section 3.3, the Jetson Nano performed the best for this project's application. The Jetson Nano also comes with the Camera Serial Interface (CSI) for connecting cameras. This interface allows image data transfer of 800 megabytes per second (MB/s) which is significantly faster than that of USB 3.0, which is capable of 650 MB/s (Stackexchange-Raspberry Pi, 2019).

Figure 22: Jetson Nano Developer Kit (NVIDIA, 2019)

A camera and LIDAR were used with the Jetson Nano to get the data required for implementation of computer vision and path planning algorithms. For the camera, a Raspberry Pi Cam Version 2.0, shown in Figure 23, was selected because it had the specifications required to fulfill the objectives of the project. This camera was also lightweight, adding only 3 g to the aircraft.

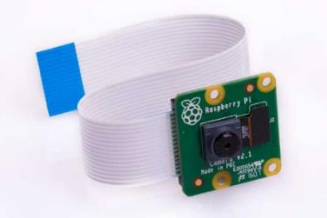

Figure 23: Raspberry Pi Cam V2 (Camera Module V2, 2019)

The Garmin LIDAR vision L3 lite was used by the 2019 VTOL MQP team to measure the altitude of their aircraft. This sensor is shown in Figure 24, and was selected for the 2020 project since it is compatible with the Jetson Nano, has an accuracy of 5cm and operating range of 40 meters (Garmin, 2019

Figure 24: Garmin LIDAR Vision L3 Lite (LIDAR-Lite, 2019)

A power supply circuit was used to provide power to all the components of the circuit during the flight mission. This project's power supply is discussed in Section 2.4. A propulsion subsystem was created with motors and electronic speed controllers. This project used total of five AT2317 motors. Each brushless motor used a Turnigy 30A electronic speed controller (ESC) to control the speed of a motor. This subsystem is discussed in detail in Section 2.4. For navigation, a GPS Compass was used to provide navigation information. A GPS Compass was found in the MQP lab and used for this project.

2.3.2 Software

Figure 25 depicts an overview of the aircraft's software.

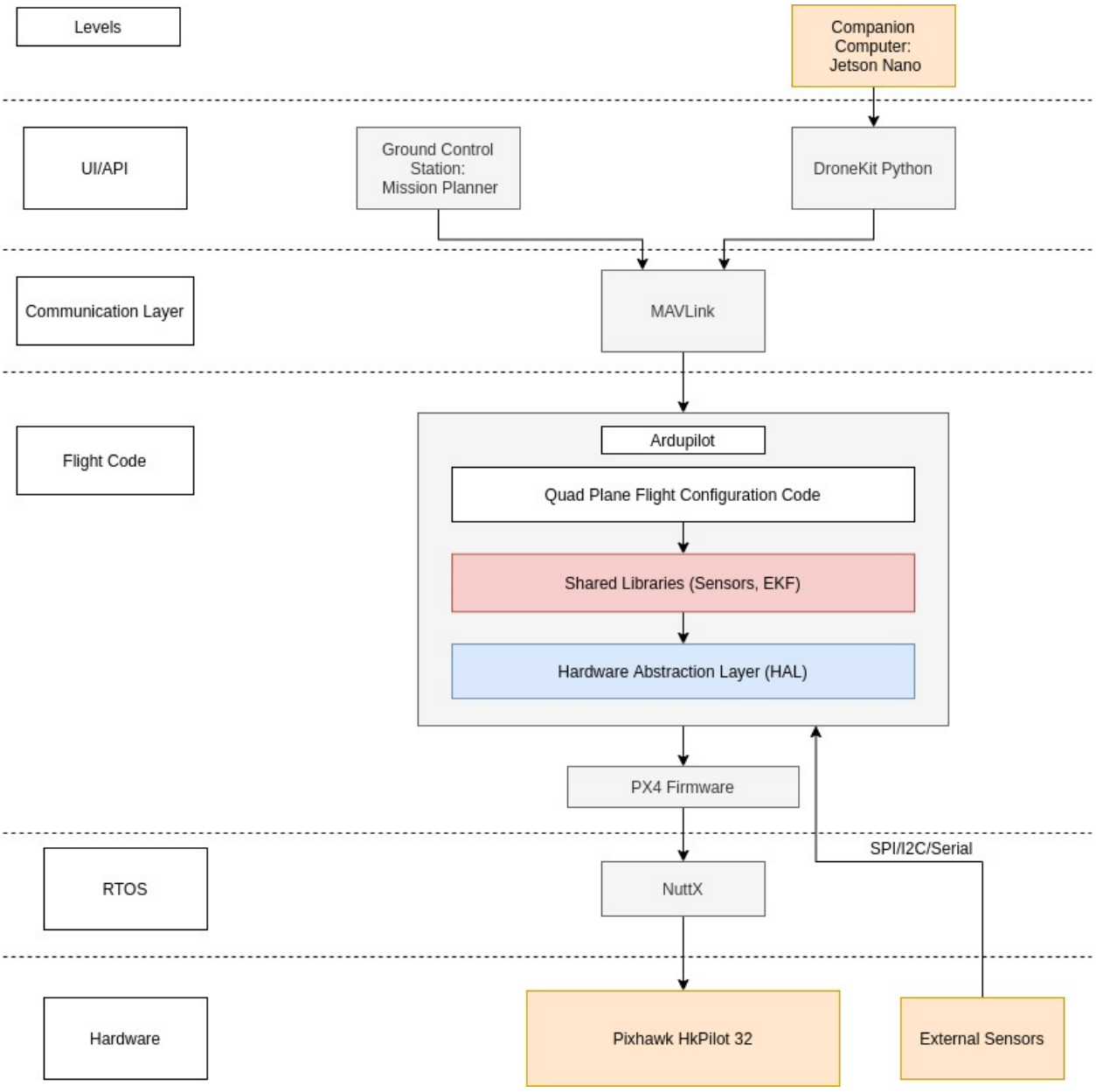

Figure 25: System Overview

The basic software structure of the aircraft can be represented in five levels:

1. User Interface / Application Programming Interface (UI / API): A User Interface and Application Programming Interface is a software layer that provides a user-friendly tool set and options to implement waypoint guidance, geofencing, sensor calibration, and program the companion computer. An API also gives a mode to

connect the companion computer with the flight controller. For this project, Mission Planner: Ardupilot was selected.

2. Communication Layer: The communication layer is used to establish communication between the UI/API and the flight controller. Depending on the application, this communication can be wired or wireless. Wired communication is usually implemented through USB. Wireless communication is dictated by the range of communication required. For a range less than 10 km, WIFI connection and radio telemetry is used. Application with range larger than 10 km uses cellular connection or long-range radio telemetry kits (ArduPilot, 2019).
3. Flight Code: Flight code is further divided into three main layers:
    a. Vehicle code: Flight code is specific to a type of aircraft. In this project, Arduplane, a plane variant of ArduPilot firmware, is used on this level of the software system. Since Arduplane firmware gives a further option of specifying an aircraft configuration, the Quad Plane flight configuration code was used for this project.
    b. Libraries: Libraries were used to reduce the number of programs that had to be written from scratch. These libraries include sensor drivers, attitude and position estimation (Extended Kalman Filters) and control code (i.e. PID controllers) (ArduPilot, 2019).
    c. Hardware Abstraction Layer (HAL): The Hardware Abstraction Layer is a set of libraries for interfacing with different flight controllers in the market, for example Pixhawk, ArduPilot Mega, and Snapdragon Flight Controller. This increases the number of compatible flight controllers with the choice of firmware.
4. Real-Time Operating System (RTOS): Since Pixhawk HkPilot32 was selected for this project, a PX4 firmware, inbuilt in the Arduplane firmware, is used to interface with the Pixhawk. This PX4 firmware is built on a real-time operating system called NuttX.
5. Hardware: The hardware level of the system specifies the hardware that will be used in the system. This hardware level is discussed in the Section 2.3.1.

2.3.3 Communications

The aircraft's communication systems are responsible for the numerous hardware and software components of the Quad-Plane to work in harmony. Communication systems allow the Quad-Plane and its operator to achieve specific tasks during operational flight (Bats Wireless Communications, 2020). Without successful communication systems, not only the unmanned flight but also the data transfer within the system required for autonomous navigation would be impossible. The communication systems are further categorized in wireless and wired communication.

1. Wireless Communication

There were two methods to control the aircraft wirelessly, through the Ground Control Station and a hand-held transmitter.

Radio Frequency (RF) communications is considered to be the most optimized solution for UAV communication systems (Bats Wireless Communications, 2020). It was used to send commands to the Quad-plane's flight controller from the ground control station. This radio frequency communication was established using a telemetry radio kit, which used the US standard radio frequency of 915 MHz (Ardupilot, 2020). The Telemetry Radio kit included two antennas that acted as both a transmitter and a receiver, depicted in Figure 26. One of these two antennas were used at each communication point, the Pixhawk and the Ground Control Station.

Figure 26: Telemetry radio kit (Readytosky, 2020)

The hand-held transmitter used a DSMX radio communication (RC) protocol to communicate with the aircraft using a receiver. To establish this protocol, a Spektrum DX8 transmitter and an AR receiver that supported DSMX protocol were used, both of which are depicted in Figure 27. DSMX RC protocol uses 2.4 GHz frequency for communications.

Figure 27: Spectrum DX8 transmitter (left) and AR receiver (right)(Spektrumrc, 2020)

2. Wired Communication

The wired communication system was responsible for relaying information between Pixhawk and Jetson Nano, and peripheral sensors and Jetson Nano.

The data flow between Pixhawk and Jetson Nano was established using the MAVLink protocol. MAVLink is a communication protocol that communicates data between two nodes regardless of the underlying physical communication interface used. For physical communication interfacing, the serial connection was established using the “Telem 2” serial port on Pixhawk. The MAVLink interfacing between the Jetson Nano and Pixhawk was enabled on the serial port by setting the “SERIAL2_PROTOCOL” parameter equal to 2 in Mission Planner (Arduplane, 2020).

The Jetson Nano received data from two sensors: a camera and a single-segment Lidar. Getting a reliable data from these sensors during the flight was required for target detection and package delivery during the mission. The camera was connected to the Jetson Nano using a CSI Interface. GStreamer, a multimedia library used for complex audio and video processing, was used to process the live stream and retrieve image data for vision-based applications (GStreamer, 2020). The Lidar was connected to Jetson Nano using I2C communication protocol. An I2C protocol library, libi2c, was used for establishing this connection.

2.3.4 Flight Control

To achieve autonomous flight, the aircraft had to switch between Quad-Copter mode and Fixed-Wing mode. The ArduPlane firmware had this feature inbuild in form of Quad-Plane configuration code shown in Figure 25. This code was enabled by setting the QENABLE parameter in Mission Planner to 1 (QENABLE=1). Enabling the code gave access to flight modes that allowed the Quad - Copter and Fixed-Wing characteristics to coexist and transition between them. Using the transmitter, it was possible to switch between flight modes manually. Several of the flight modes that were used are listed below.

1. QSTABILIZE: Stabilizes the aircraft around the roll and pitch axis.
2. QHOVER: Maintains the altitude of the aircraft while hovering.
3. QLOITER: Maintains the aircraft's altitude while circling around a given position.
4. QLAND: Lands the aircraft using VTOL in a desired location.
5. FBWA (Fly-By-Wire A): Assists in flying in Fixed Wing mode. For this mission this mode would be used to transition to and perform horizontal flight.

2.3.5 Vision Based Navigation

Vision based navigation allowed the Quad-plane to detect the target location for dropping the delivery package, navigate to the location, and drop it using dropping mechanism. Below is the vision system description.

1. Physical System Connection

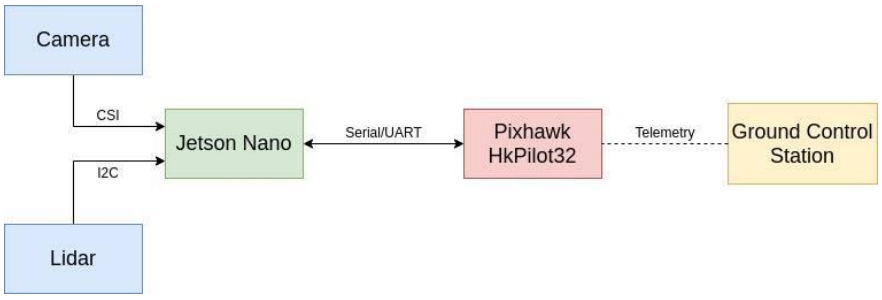

Figure 28: Physical System Connections

The physical system involved the Pixhawk, Jetson Nano, peripheral sensors (Camera and Lidar), and ground control station (laptop in this project). The flow chart in Figure 28 shows different communication interfaces used to relay data within the system.

2. Data Flow Overview

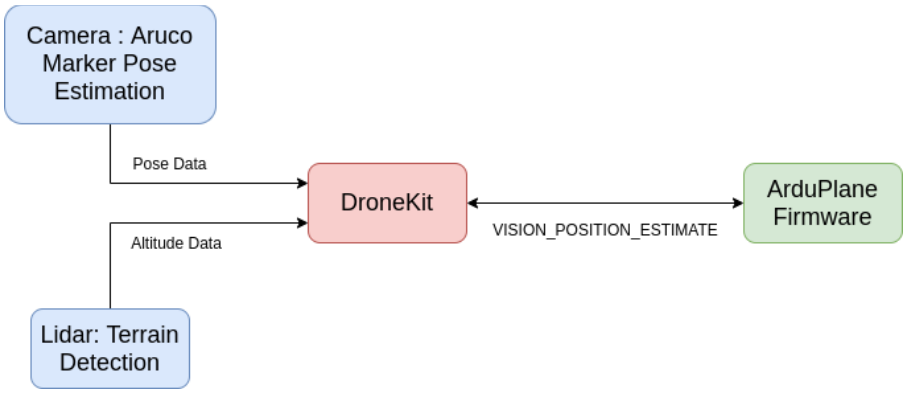

Figure 29: Vision-based navigation data flow

Vision based navigation required data from external sensors. This data flow is depicted in Figure 29. Camera and single-segment Lidar were two main sensors used in this project. The camera provided 3d pose of the the target with respect to the Quad-plane and Lidar provided the altitude data. This data was sent to the mission application developed in DroneKit API. Dronekit API allowed the connection between Jetson Nano and Pixhawk. Through this connection, users are allowed to update different flight parameters in the flight controller. In this case, VISION_POSITION_ESTIMATE paramer, which takes in pose from external sensors, was updated based on data from th camera and Lidar. To fuse this incoming data with position data from onboard sensors like gyroscope and GPS, an inbuilt EKF had to be used. There are total four EKFs built in the Arduplane firmware, as shown in Figure 25., and for this case EKF2 was used, since it is mainly designed to work with data from external sensors (Ardupilot, 2020). EKF2 had to be enabled in ArduPlane through Mission Planner before the external data can be used or any applications. For EKF2 to run, the home location had to be set at the beginning of the mision. The workflow process explains how the vision based navigation can be initiated and run the autonomous mission.

3. Workflow Process

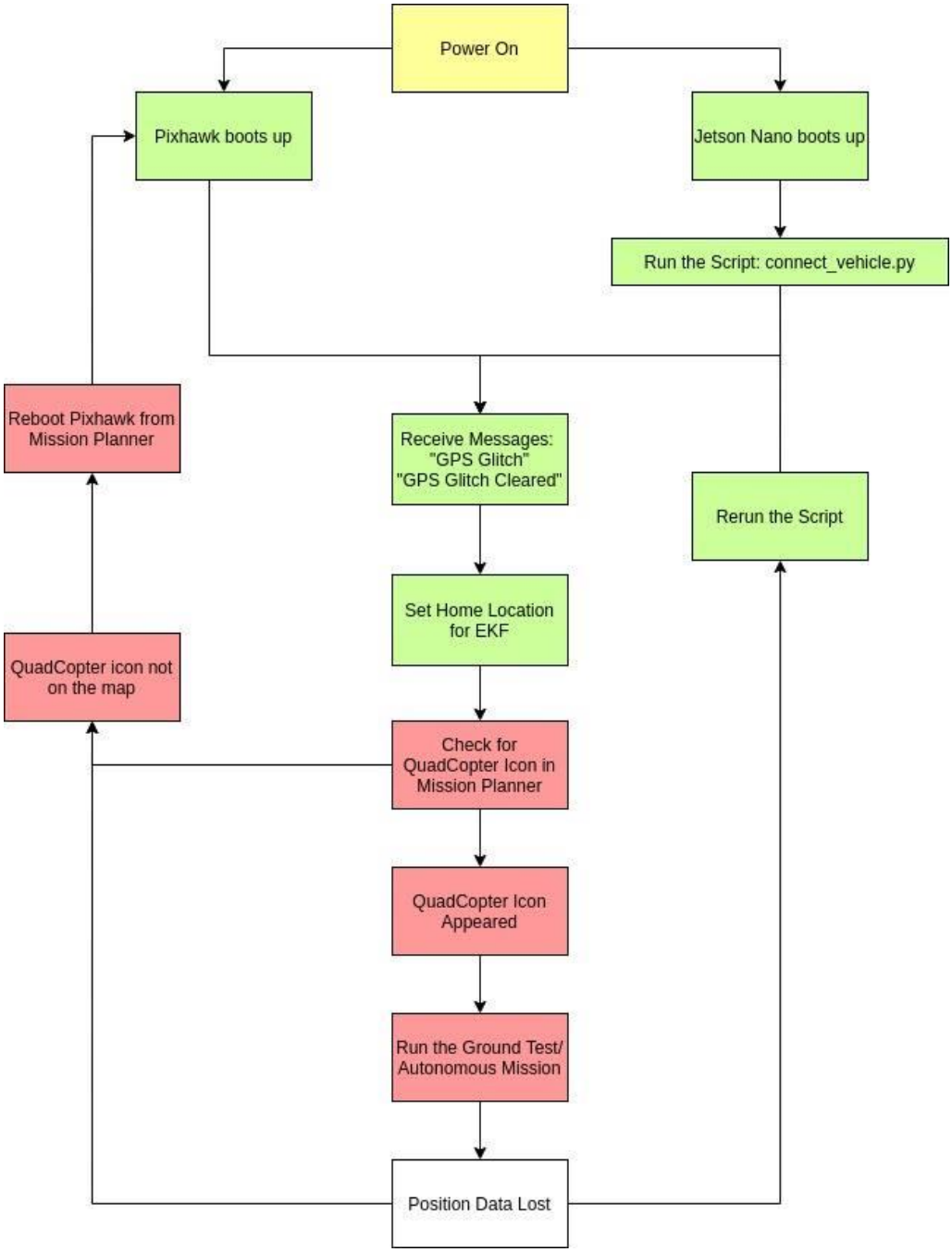

Figure 30: Workflow process

The workflow process explains how the system goes from switched off to executing the flight mission uploaded in the aircraft. Following are the steps from the chart above:

1. Turn on the power to the Quad-plane. The Jetson Nano and the Pixhawk controller boot up. The Jetson Nano runs the script *connect_vehicle.py*, which established MAVLink connection between the Jetson Nano and Pixhawk and started receiving data from the external sensors.
2. Once the VISION_POSITION_ESTIMATE parameter was updated in the aircraft firmware, the "GPS Glitch" and "GPS Glitch cleared" messages were seen on the screen. This confirmed that the external localization data were being received by the flight controller.
3. After this the aircraft icon appeared and then the autonomous mission to deliver the package was started.
4. The software was designed in a way that if the position data was lost at any moment *connect_vehicle.py* script was rerun to reestablish the MAVLink connection between Jetson Nano and Pixhawk.

If the icon of the aircraft disappeared from the map, then the Pixhawk was rebooted from Mission Planner.

2.4. Power and Propulsion

WPI competition rules required a 1000 W power limiter, as shown in Figure 31, meaning the aircraft could not use power above 1000 W if provided by the battery. Additionally, the competition allowed for a maximum battery capacity of 2200 mAh. As a larger battery capacity would allow for a longer duration flight, only batteries with this capacity were compiled in Table 20 in Section 3.2. The battery selected was the Turnigy Nano-Tech 45-90C 2200 mAh, which supplies 1098.9 W, depicted in Figure 32.

Figure 31: A NeuMotors 1000-watt power limiter (NeuMotors, 2019)

Figure 32: Turnigy Nano-Tech 45-90C 2200 mAh battery (HobbyKing, 2019)

The maximum current rating needed for the Power Distribution Board (PDB) for the aircraft was 125A, which is the combined maximum current draw from all five motors. The Airbot PDB, depicted in Figure 33, was selected because it is rated at 200A and had 8 pairs of soldering pads.

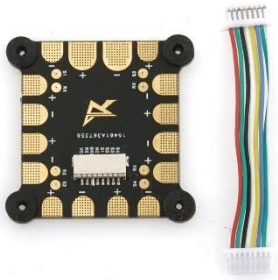

Figure 33: Airbot 200A PDB (Original Airbot, 2019)

After the battery was selected, motors were examined. Table 21 in Section 3.4.2 displays data on motors that would allow the aircraft to hover at roughly 70% throttle. The AT2317 was selected due to its ability to generate 945 grams of thrust, its low weight, and high efficiency. Section 3.4 includes additional information on the motor analysis.

For the motor, AT2317, the current drain at full throttle is 25A (Tmotor, 2019). To ensure the circuitry could handle this maximum current draw, the Multistar Turnigy 30A Electronic Speed Controller (ESC) was selected. This component is rated for a maximum current of 30A and is depicted in Figure 34.

Figure 34: Multistar Turnigy 30A ESC (Turnigy, 2019)

3. Design Analysis and Rationale

3.1. Mission and Simulation

3.1.1 Competition Scoring

A toolbox was developed to estimate the score based on given design parameters. This would allow for design iterations to maximize the score of the aircraft. Placement in the WPI competition is based on Equation (1), the scoring equation from Section 1.1, again listed below.

$$Score = \lambda_1 \frac{W_{payload}}{W_{empty}} t_{flight} V_{avg} + \lambda_2 \Delta + \lambda_3 \sum_n A_n + P \quad (1)$$

The inputs taken by the toolbox are listed below:

- Wing and tail airfoils and geometry
- Aircraft flight speed
- Aircraft fuselage geometry
- Motors for Vertical flight and horizontal flight
- Battery
- Aircraft empty mass

From these parameters, the following performance aspects of the aircraft were calculated:

- Aerodynamic coefficients of the airfoil based on XFLR5 simulation of the airfoil geometry
- Minimum energy required for vertical takeoff or landing based on motor thrust vs. power data and aircraft mass
- Aircraft parasitic drag coefficient C_{D_o} based on aircraft geometry
- Minimum energy required to transition to horizontal flight based on motor thrust vs. power data, airfoil aerodynamic coefficients and aircraft weight
- Power required for horizontal flight based on aircraft geometry, airfoil aerodynamic coefficients and motor thrust vs. power data

Finally, the overall mission score is calculated based on the aircraft's performance, the autonomy capabilities achieved, and the design's originality. See Section 2.1 for the list of autonomy capabilities. The final score of the aircraft design for this project is calculated in the next section.

3.1.2 Performance Optimization

As a VTOL aircraft, this vehicle had a shorter endurance than a standard fixed-wing aircraft. This is due to motors being required to counteract the weight of the aircraft during hover. To reduce this disparity, this design aimed to minimize power usage during the costly periods of hover and transition to horizontal flight while avoiding these flight regimes whenever possible. This was accomplished using a linear-quadratic regulator (LQR).

For a given linear system $\dot{x} = Ax + Bu$, with the control effort defined as $u = -Kx$, the gain matrix K can be found by using the cost function Equation (2).

$$J(u) = \int_0^\infty (x^T Q x + u^T R u + 2x^T N u) dt \tag{2}$$

Where Q, R, and N are matrices used to weigh the costs of state error, control effort, and the cross relation of these two, respectively. The matrix N was set to 0 for all simulations conducted. The value of K is given by Equation (3).

$$K = R^{-1}(B^T S + N^T) \tag{3}$$

Where S is the solution to the algebraic Riccati equation, Equation (4).

$$A^T XE + E^T XA + E^T XGXE - (E^T XB + S)R^{-1}(B^T XE + S^T) + Q = 0 \tag{4}$$

In the above equation, the original x corresponding to the model is replaced with the equivalent state-space model in Equation (5) with the nonsingular matrix E.

$$\dot{X} = E^{-1}AX + E^{-1}Bu \tag{5}$$

LQR was used on a simplified linear model of the aircraft dynamics in the scenarios of vertical takeoff or landing and transition between hover and horizontal flight. For each scenario, the optimal gain matrix K was determined based on the model and the cost matrices using the 'lqr' function in the MATLAB® Control Systems Toolbox. The scenarios were then simulated in

MATLAB® for a given set of initial conditions, with the control effort at each time step converted to the corresponding required thrust from each motor on the aircraft. Using linear interpolation, the thrust requirements were translated into the power consumed by each motor based on thrust curves provided by the motor manufacturer. The thrust was limited to ensure the motors were not loaded past the manufacturer limits and to also remain under the aircraft power limits mandated by the WPI competition rules. Power consumption was numerically integrated from the beginning of the simulation until the settling time of the system to yield a total energy consumption for each scenario. The settling time could then be used as an input by the flight controller, which was capable of performing these maneuvers autonomously.

3.1.2.1 Takeoff Performance

For this simulation, the state space model of the aircraft dynamics is Equation (6).

$$\dot{X} = \begin{bmatrix} 0 & 1 \\ 0 & 0 \end{bmatrix} X + \begin{bmatrix} 0 \\ 1 \end{bmatrix} u(t) \tag{6}$$

Here, x_1 is the vertical distance from the target altitude in meters and x_2 is the vertical velocity in meters per second. This model results in $K = [k_p \quad k_d]$, with the control gain values k_p and k_d affected by the choice of Q and R. The resulting control effort is determined by Equation (7).

$$u(t) = -k_p x_1 - k_d x_2 \tag{7}$$

The aircraft is assumed to be going slow enough to neglect drag forces. Thus, the total control force is equivalent to the acceleration along the vertical axis due to the combination of the thrust from the vertical motors and gravity, shown in Equation (8).

$$u(t) = \frac{T_{vert}}{m} - g \tag{8}$$

$$T_{vert} = \sum_i T_i \tag{9}$$

Where T_i is the thrust generated by vertical motor i. As this simulation did not involve attitude control, all values of T_i in Equation (9) were equal at each time step. Each motor's thrust was capped at the maximum value listed in manufacturer data.

A range of Q matrices were tried, with the intention of finding the scale factor $\lambda_{takeoff}$ in Equation (10) that minimized total energy consumption. R was held constant, with $R = 1$.

$$Q = \lambda_{takeoff} \begin{bmatrix} 1 & 0 \\ 0 & 1 \end{bmatrix} \tag{10}$$

Finally, the initial conditions for this simulation of takeoff, x_0, are in Equation (11).

$$x_0 = \begin{bmatrix} -alt_{des} \\ 0 \end{bmatrix} \tag{11}$$

Here, alt_{des} was set to be 6 meters. After obtaining the gain matrix K by using the MATLAB® LQR function, the system was simulated with the MATLAB® numerical differential equation solver 'ode45'. The individual motor thrust at each time step was converted to power consumption by linearly interpolation of manufacturer thrust curve data. The settling time was defined as the point after which the altitude error no longer exceeded 2% of the initial error from the desired altitude. Finally, the minimum energy consumption of all the scale factors was found. By changing the sign of the initial altitude error $x_0(1)$, this scenario was also used as a landing energy optimization.

The graphs in Figure 35 depict the states and motor power consumption during a simulated takeoff of a 3 kg aircraft with 4 AT2317 motors with APC 9"x6" propellers installed for vertical flight. The target altitude was set at 6 meters.

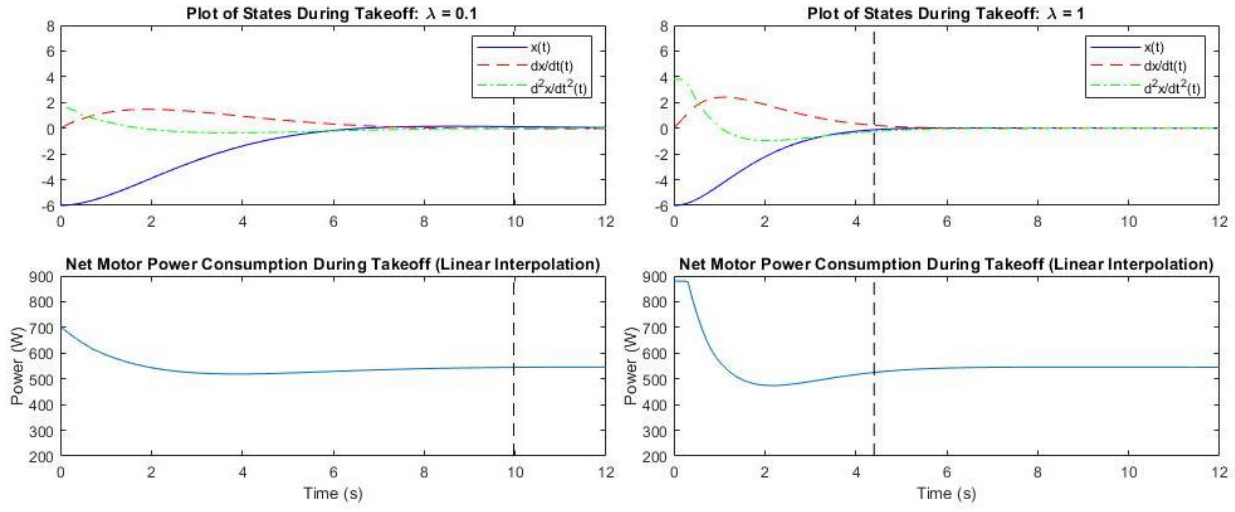

Figure 35: Simulated vertical takeoff for a λ of 0.1 (left) and 1 (right)

With a $\lambda_{takeoff}$ of 0.1, the system settles in 9.97 seconds and requires 1.04 watt-hours to takeoff, while a $\lambda_{takeoff}$ of 1 causes the system to settle in 4.34 seconds while requiring 0.46 watt-hours to reach the target altitude. Scaling Q higher while holding R constant reduces the settling time and decreases the total energy required for takeoff. In this situation, it is not desirable to minimize control effort $u(t)$ rather than the state error, as a control effort of 0 still corresponds to a nonzero power consumption. However, this requires a slightly higher max vertical velocity and a significantly higher initial thrust. Furthermore, the motors max out at a finite thrust due to their limits and the power limitations of the aircraft. This effect can be further seen in Table 8 below, which compares the system behavior for a greater variety of scale factors.

Table 8: Takeoff Simulations with Varying Scale Factors

$\lambda_{takeoff}$	0.1	0.5	1	2
Settling Time, s	9.97	4.48	4.34	4.15
Total Energy Consumed, Wh	1.04	0.48	0.46	0.44
Max Power Consumption, W	723	900	734	900

It is apparent that total energy consumption is roughly proportional to the altitude settling time, which is reasonable as during each second of takeoff the motors must at a minimum counteract the force of gravity. Given the system does not change with $\lambda_{takeoff}$ (as the motor power consumption and aircraft weight are constant), the average power consumption would not vary significantly between each $\lambda_{takeoff}$ apart from the brief initial extreme power consumption.

The empty aircraft's landing performance is depicted in Figure 36 below. Here the total mass is only 2.3 kg due to the payload already having been dropped.

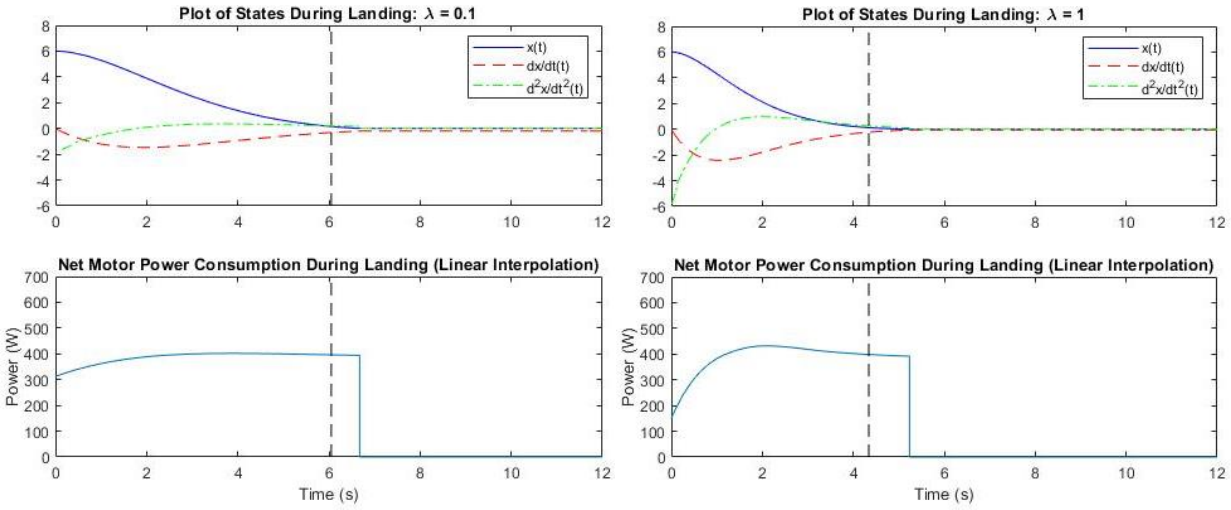

Figure 36: Simulated vertical landing for a λ of 0.1 (left) and 1 (right)

With a $\lambda_{landing}$ of 0.1, the system settles in 6.05 seconds and takes 0.47 watt-hours to land, while a $\lambda_{landing}$ of 1 causes the system to settle in 4.34 seconds and take 0.34 watt-hours to reach the ground. Scaling Q has a similar effect on landing on takeoff. Landing requires less energy as the motors do not need to completely counteract gravity for the entire maneuver. This effect can be further seen in Table 9 below, which compares the system behavior for the same range of $\lambda_{landing}$ values used in Table 8. As with takeoff, shorter settling times result in less energy consumption, albeit while requiring slightly higher maximum power consumption.

Table 9: Landing Simulations with Varying Scale Factors

$\lambda_{landing}$	0.1	0.5	1	2
Settling Time, s	6.05	4.48	4.34	4.14
Total Energy Consumed, Wh	0.45	0.33	0.33	0.31
Max Power Consumption, W	281	294	303	313

Once the aircraft has left the ground, it needs to accelerate horizontally so the fixed wing can generate lift. This transition was modeled assuming the aircraft maintained a fixed angle of attack of 0 degrees, as this is the trim angle of attack. It is also assumed that the aircraft can perfectly observe its states so it can estimate the resulting lift and drag forces. The state space model is defined in Equation (12).

$$\dot{X} = \begin{bmatrix} 0 & 1 & 0 \\ 0 & 0 & 0 \\ 0 & 0 & 0 \end{bmatrix} X + \begin{bmatrix} 0 & 0 \\ 0 & 1 \\ 1 & 0 \end{bmatrix} \begin{bmatrix} h(t) \\ u(t) \end{bmatrix} \tag{12}$$

Here, x_1 is the vertical distance from cruise altitude in meters, x_2 is the vertical velocity in meters per second, and x_3 is the horizontal velocity in meters per second. The structure of the gain matrix K is in Equation (13).

$$K = \begin{bmatrix} 0 & 0 & k_{horz} \\ k_p & k_d & 0 \end{bmatrix} \tag{13}$$

In this simulation, the vertical acceleration $u(t)$ has the same control structure used in Section 3.1.2.1 in Equation (7). However, the vertical acceleration also includes a lift force as the horizontal speed increases, resulting in Equation (14). All of the vertical motors are again assumed to generate equal amounts of thrust.

$$u(t) = \frac{T_{vert}+L}{m} - g \tag{14}$$

This lift force comes from Equation (15).

$$L = \frac{1}{2}\rho V^2 C_L S \tag{15}$$

Here, ρ is the air density, V is the horizontal aircraft velocity, C_L is the coefficient of lift of the aircraft, and S is the total aircraft wing area.

This simulation also involves a horizontal acceleration due to the balance between horizontal thrust T_{horz} and drag D in Equation (16).

$$h(t) = \frac{T_{horz}-D}{m} \tag{16}$$

The drag equation has the same structure as Equation (15), only with C_L replaced with the coefficient of drag C_D. This relationship is shown in Equation (17).

$$D = \frac{1}{2}\rho V^2 C_D S \tag{17}$$

The horizontal control effort $h(t)$ is proportional to the difference in the aircraft's horizontal speed from its desired speed v_{des}, shown in Equation (18).

$$h(t) = -k_{horz}(x_3 - v_{des}) \tag{18}$$

Rather than weigh all the states equally, in this scenario the vertical states can be weighed less, as a slight loss in altitude during the transition is acceptable. This results in Q matrices of the form shown in Equation (19), where $Q_1 = Q_2 \leq Q_3$.

$$Q = \begin{bmatrix} Q_1 & 0 & 0 \\ 0 & Q_2 & 0 \\ 0 & 0 & Q_3 \end{bmatrix} \tag{19}$$

As this simulation contains two control efforts, the weight matrix R was held constant at $R = \begin{bmatrix} 1 & 0 \\ 0 & 1 \end{bmatrix}$. The same process of converting the control efforts to motor power consumption was used for this transition energy optimization as the takeoff energy optimization. The settling time was defined as the point when the aircraft's horizontal velocity reached within 2% of its target velocity. Although this simulation only models a transition from hover to horizontal flight, it is assumed that the same transition in reverse will consume a similar amount of energy.

The graphs in Figure 37 depict the states and energy consumption for a transition of the loaded aircraft with the diagonal of Q equal to [1, 1, 1]. With this relatively small magnitude, the horizontal motor runs at maximum throttle for nearly 2 seconds. This transition consumes a total of 0.40 Wh, taking 4.41 seconds to settle to the target velocity.

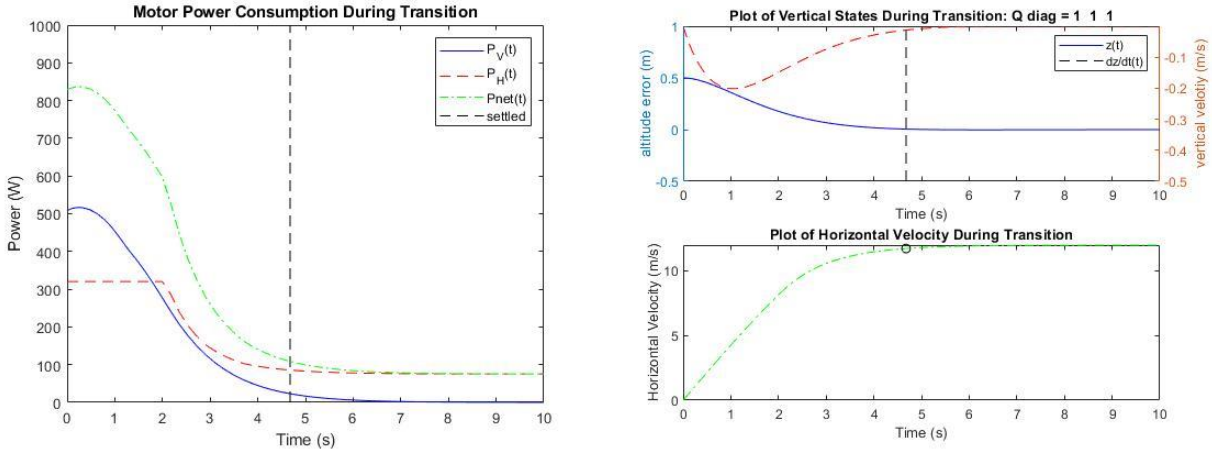

Figure 37: Transition states (left) and power consumption (right) with Q diagonal = [1, 1, 1]

In comparison, the transition with the diagonal of Q equal to [100, 100, 100] is depicted in Figure 38. This transition settles to the target velocity far faster, taking 0.36 Wh and 2.57

seconds to reach it. This is due to the horizontal motor running at full speed for the full duration of the transition.

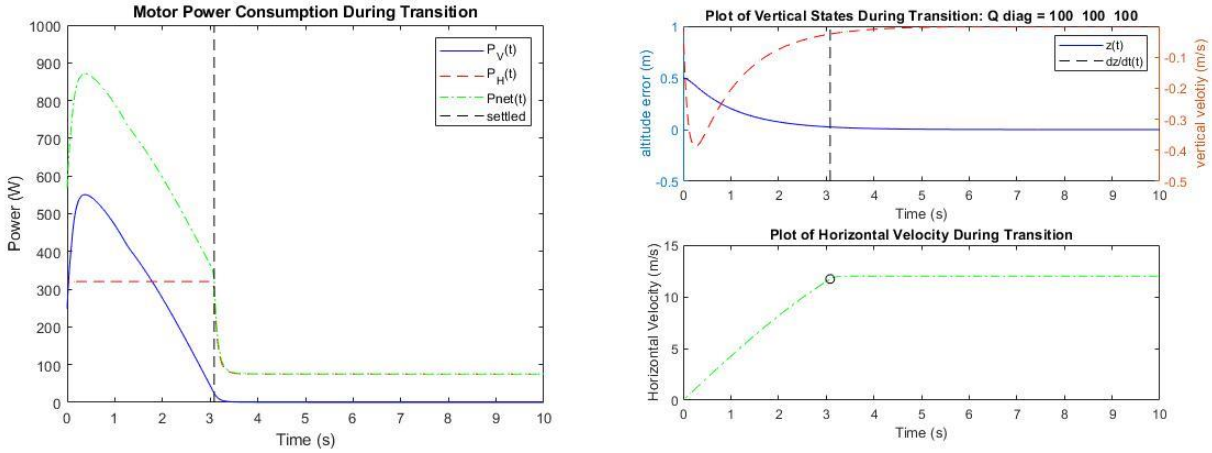

Figure 38: Transition states (left) and power consumption (right) with Q diagonal = [100, 100, 100]

Unsurprisingly, reducing the aircraft mass allows it to transition to horizontal flight while consuming less energy, as it corresponds to a greater thrust-to-weight ratio in both the vertical and horizontal direction. In Figure 39, it can be seen that the peak power consumption of the combined vertical motors is about 100 W lower for the empty aircraft for the same Q diagonal as seen in Figure 38 for the full aircraft. Additionally, running the horizontal motor at maximum throttle causes the empty aircraft to reach cruise speed faster. In all, the empty aircraft settles to cruising speed in 1.97 seconds, consuming 0.23 Wh of energy in the process.

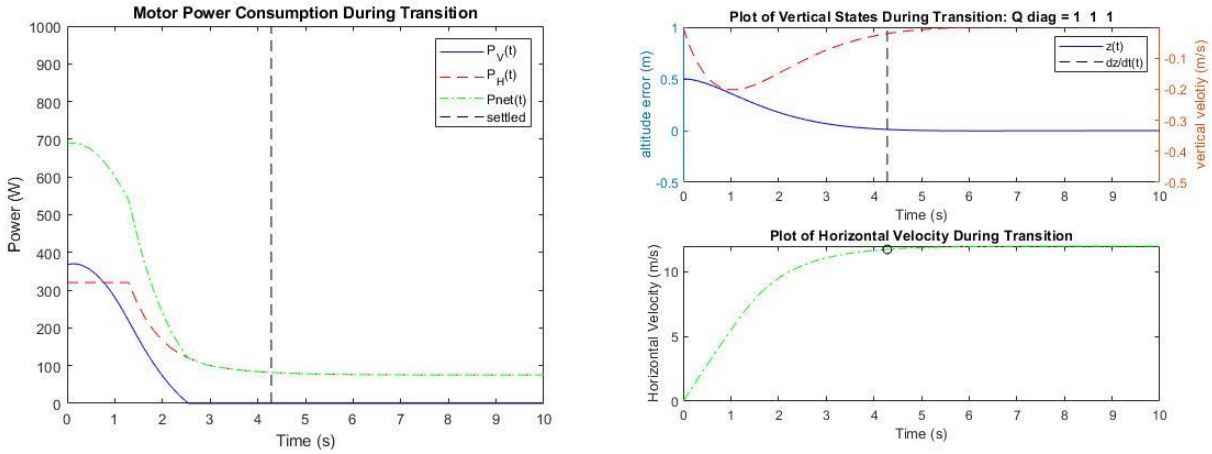

Figure 39: Transition states (left) and power consumption (right) of the empty aircraft with Q diagonal = [100, 100, 100]

3.1.2.3 Range Estimation

With the previous two components of the aircraft mission well established, the next step is to develop an estimation of the aircraft's endurance during level flight. This will be estimated with two different methods.

A margin of the total battery capacity is not allotted to the mission. This is done in order to reserve energy to return to the landing zone, while also to avoid completely draining the battery to preserve its lifespan. Any energy not used during takeoff, landing, transitions or saved for this margin is allotted to horizontal flight. This is summarized in Equation (20).

$$E_{flight} = marginE_{capacity} - E_{takeoff} - E_{landing} - E_{transitions} \quad (20)$$

The first method of estimating aircraft endurance relies only on the aircraft's power consumption during level flight. During level flight, horizontal thrust T_{horz} must equal aerodynamic drag D, resulting in Equation (21).

$$T_{horz} = D = \frac{1}{2}\rho V^2 S C_D \quad (21)$$

The power required for this thrust is found through linear interpolation in manufacturer thrust curve data. Dividing the energy allotted to horizontal flight by this power results in an upper estimate of the aircraft endurance from Equation (22).

$$t_{flight} = \frac{E_{flight}}{P_{level}} \quad (22)$$

The second method of estimating aircraft endurance simulates the flight of the aircraft modeled as a particle. The purpose of this simulation is to verify that the magnitude of the previous estimation of total flight time is correct, while also to provide a more realistic estimate that accounts for the limited flight region.

This simulation begins after the aircraft has transitioned to level flight. The aircraft travels in a straight line until the distance to the boundary of the flight area it is facing is equal to its minimum radius of turn. At this point, it makes a 90-degree turn to stay in the area, following a clockwise path around the field.

As the turns are level turns at constant speed V and minimum radius of turn R_{turn}, they will also have a constant derivative of heading angle as calculated by Equation (23).

$$\dot{\psi} = \frac{V}{R_{turn}} = const. \tag{23}$$

Starting with the equation for minimum turning radius, Equation (24).

$$R_{turn,min} = \frac{V^2}{g\sqrt{n_{min}^2 - 1}} \tag{24}$$

The value of n_{min} is the minimum of two load factor equations. The first load factor—$n_{max,t}$—accounts for the effect of maximum horizontal thrust T_{max} and parasitic drag C_{D_o}. This relationship is shown in Equation (25).

$$n_{max,t} = \sqrt{\frac{Q}{K(W/S)}\left(\frac{T_{max}}{W} - \frac{QC_{D_0}}{(W/S)}\right)} \tag{25}$$

In Equation (25), W is the loaded weight of the aircraft. Q is the dynamic pressure at cruise, which is found via Equation (26).

$$Q = \frac{1}{2}\rho V^2 \tag{26}$$

K is a coefficient that characterizes induced drag, and is obtained via Equation (27), based on the wing aspect ratio AR and the Oswald efficiency factor e.

$$K = \frac{4}{3}\frac{1}{\pi e AR} \tag{27}$$

The second load factor—$n_{max,\alpha}$—is determined by the maximum lift coefficient that the aircraft wing can provide, $C_{L_{max}}$, via Equation (28).

$$n_{max,\alpha} = \frac{QC_{L_{max}}}{(W/S)} \tag{28}$$

A third load factor—$n_{max,s}$—accounts for the structural load limitations of the aircraft. However, this factor can be assumed to be larger than either of the two calculated factors. The smaller of the load factors is then converted back to a corresponding coefficient of lift in Equation (29), which is obtained by rearranging Equation (28). This coefficient of lift is used in

the drag polar equation, listed below as Equation (30), to approximate the coefficient of drag experienced for this radius of turn.

$$C_L = \frac{n_{min} W}{QS} \tag{29}$$

$$C_D = C_{D0} + K C_L^2 \tag{30}$$

The drag experienced by the aircraft is equated to thrust in both turning and level flight. From here, the motor power consumption during flight can found from linear interpolation in manufacturer thrust curve data. Finally, the estimated power of the flight computer and other electronics is added to yield the total power consumption during turns and level flight.

For a 3-cell 2200 mAh battery, a total of 24.42 Wh of energy is available. Using only 75% of the battery's total capacity, the energy for flight is found by using the minimum takeoff and landing energy calculated previously, along with the minimum loaded and empty transition energy. It is assumed the aircraft makes 4 transitions during its flight, 2 of which are after the payload has been dropped (thus they are conducted by the empty aircraft). As a result, the energy usable for flight is found in Equation (31). Assuming only horizontal flight, which for the current aircraft design requires 75 W of power to be supplied to the horizontal motor, the aircraft has an upper estimate of range of 561 seconds.

$$E_{flight} = 0.8 * 24.42 - 0.68 - 0.60 - (2 * 0.58 + 2 * 0.51) = 14.85\ Whr \tag{31}$$

Simulating the mission results in the aircraft following the clockwise trajectory shown in Figure 40 below, starting at the red circle and ending at the black circle after completing 9 full laps of the flight area.

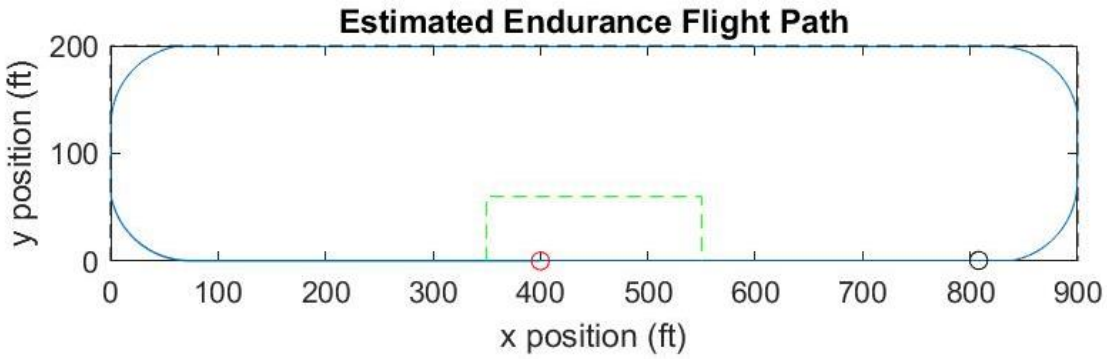

Figure 40: Aircraft flight trajectory (blue). The green dotted line indicates the takeoff and landing zone, while the outer black dotted line is the total permitted flight zone.

Due to the increased power consumption of turning, this trajectory consumes the allotted power after 520 seconds. The unused 25% of the battery is useful in the above situation, as the aircraft would need to expend energy to travel from the black circle to the payload drop target, which would be at roughly $(x, y) = (100, 150)$. Even so, this aspirational flight time does not account for any period of hovering that would be necessary for the aircraft to locate the target.

Using the more conservative flight time estimation, the aircraft's goal score can be calculated. First, it is assumed that all the autonomy objectives can be satisfied. Additionally, the aircraft can get maximum points for payload drop while carrying 1 kg of payload and receiving an originality score of 2. This low originality score is assumed because the design draws heavily from this project's literature review while not being overly ambitious. This team's aspirational score is found in Equations (32) and (33).

$$Score = 0.01\frac{0.2}{2.8} * 520 * 12 + 35 * 1 + 35 * (1 + 1 + 3 + 5 + 1) + 2 \quad (32)$$

$$Score = 391\ pts \quad (33)$$

Much of this aspirational score come from autonomy or payload drop related sources. Of the total score of 391 points, 350 come from satisfying autonomy objectives, while 35 come from an accurate payload drop and only 6 points come from carrying a payload during the cruise phase. This is again due to the inherent range and payload shortfall of a VTOL vehicle versus a conventional fixed-wing aircraft.

3.1.3 Stability Analysis

Stability is a desirable trait for aircraft, as it reduces the control effort necessary to restore the states of the aircraft after a disturbance. There are two main components of stability: static stability and dynamic stability.

It is preferable to have an aircraft with a positive longitudinal static stability, meaning the aircraft would trend towards returning to its original state after a disturbance about the pitch axis. This is primarily analyzed about the longitudinal axis through ensuring that the neutral point of the aircraft is in front of the center of gravity. The position of the neutral point relative to the leading edge of the wing is found with Equation (34):

$$h_{NP} = h_{nWB} + \frac{at}{a}\bar{V}_H\left(1 - \frac{\partial\epsilon}{\partial\alpha}\right) \tag{34}$$

Where the horizontal tail volume ration $\bar{V}_H$ is found by Equation (35).

$$\bar{V}_H = \frac{\bar{l}_t S_t}{\bar{c}S} \tag{35}$$

Table 10 below contains the definitions of the above variables along with their values for the aircraft.

Table 10: Summary of aircraft properties relevant to location of neutral point

Variable	Definition and Units	Value
h_{nWB}	location of the aerodynamic center of the wing, fraction of the mean wing chord	0.250
a_t	lift-curve slope of the horizontal tail, $radians^{-1}$	3.432
a	lift-curve slope of the wing, radians^{-1}	4.779
$\bar{V}_H$	horizontal tail volume ratio	0.552
$\bar{l}_t$	horizontal distance between the horizontal tail aerodynamic center and the wing aerodynamic center, m	0.698
S_t	wetted area of the horizontal tail, m^2	0.076
$\bar{c}$	mean wing chord, m	0.250
S	area of the wing, m^2	0.386
$\frac{\partial\epsilon}{\partial\alpha}$	partial derivative of the downwash angle on the horizontal tail with respect to the aircraft angle of attack	0.321

The values for the lift-curve slopes and the partial downwash partial derivative were calculated with equations from Napolitano's *Aircraft Dynamics: From Modeling to Simulation* (Napolitano, 2012).

Using the above equation, the neutral point was found to be 0.126 meters behind the leading edge of the wing. In comparison, conducting a stability analysis of the aircraft in XFLR5 resulted in the neutral point being 0.143 meters behind the leading edge. As a result, keeping the center of gravity less than 0.1 meters behind the wing leading edge will result in a statically stable aircraft according to both analyses. Using the smaller neutral point distance and this assumed location of the aircraft center of gravity, the aircraft has a static margin of 0.26 meters.

Dynamic stability corresponds to the long-term behavior of a system after a disturbance. It was desired to have positive dynamic stability, where any long-term oscillations after a disturbance would decay in amplitude over time. This project's analysis relied on small-disturbance theory, where the aircraft dynamics are linearized about trim conditions. Likewise, it can also be assumed that the longitudinal and lateral motion can be decoupled due to the structure of the aircraft's moment of inertia matrix (see Table 2 in Chapter 2). This results in Equations (36)-(39), differential equations for the rates of change in the aircraft states based on their small changes from trim conditions.

$$\dot{X}_{Long} = A_{Long} X_{Long} \tag{36}$$

$$\dot{X}_{Lat} = A_{Lat} X_{Lat} \tag{37}$$

$$X_{Long} = [\Delta u \quad \Delta w \quad \Delta q \quad \Delta \theta]^T \tag{38}$$

$$X_{Lat} = [\Delta v \quad \Delta p \quad \Delta r \quad \Delta \phi]^T \tag{39}$$

Where:

$\begin{bmatrix} u \\ v \\ w \end{bmatrix}$ is the wind-relative velocity of the aircraft in the aircraft body frame in meters per second

$\begin{bmatrix} p \\ q \\ r \end{bmatrix}$ is the angular velocity of the aircraft in the aircraft body frame in radians per second

θ is the wind-relative pitch angle of the aircraft in radians

ϕ is the wind-relative roll angle of the aircraft in radians

The values of both A_{Long} and A_{Lat} are determined from the equations for the aircraft stability derivatives from Napolitano's *Aircraft Dynamics: From Modeling to Simulation* (Napolitano, 2012). These stability derivatives and eigenvalues were cross-referenced with a stability analysis conducted in XFLR5. Figure 41 is a screenshot of the aircraft airfoils rendered in XFLR5.

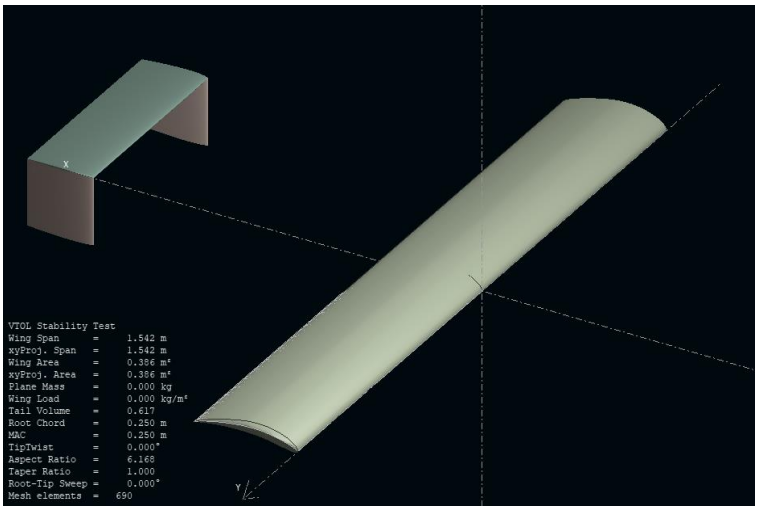

Figure 41: Render of aircraft airfoils in XFLR5

The stability derivatives relevant to longitudinal stability are listed in Table 11, along with their values according to both Napolitano's empirical equations and the XFLR5 stability analysis.

Table 11: Summary of aircraft longitudinal stability derivatives

Stability Derivative	Value from Equations	Value from XFLR5
C_{x_u}	-0.228	-0.084
C_{x_α}	0.330	0.623
$\boldsymbol{C_{z_u}}$	-1.732	0
C_{L_a}	5.183	4.850
C_{L_q}	8.597	7.996
C_{m_u}	0	0.003
C_{m_a}	-0.318	-0.834
C_{m_q}	-10.899	-15.121

It can be seen that the stability derivatives from both sources are within an order of magnitude of each other, the notable exception being C_{Z_u}, which is bolded above. The forces on

the z-axis of the aircraft in level flight are dominated by lift. As the lift force is proportional to velocity squared (of which u, the velocity along the x-axis of the aircraft's body frame, is the dominant component), a change in velocity should have a noticeable effect on forces in the z-axis. For this reason, the value of C_{Z_u} from XFLR5 should be ignored. With this in mind, the results below correspond to three different scenarios:

1. The results exclusively according to the equations from Napolitano (2012)
2. The results exclusively according to the XFLR5 stability analysis
3. The results according to the XFLR5 stability analysis but with the value of C_{Z_u} and any other stability derivatives not provided by XFLR5 taken from Napolitano's equations. In particular, the wind-relative linear acceleration of the aircraft along the aircraft's z-axis, $\dot{w}$, results in the dimensional derivatives $Z_{\dot{w}}$ and $M_{\dot{w}}$ that are not listed after XFLR5's analysis but can be found with the equations utilized in Scenario 1.

The A_{Long} matrices from each of the three scenarios are listed in Table 12 along with their respective eigenvalues. An aircraft is dynamically stable if all of the eigenvalues of both A_{Long} and A_{Lat} have negative real parts. Although the real and imaginary parts of the eigenvalues vary between scenarios, in all cases the aircraft is found to be dynamically stable about the longitudinal axis.

Table 12: Comparison of Longitudinal A matrices for different scenarios

Scenario	A_{Long}				Eigenvalues
1	-0.210	0.241	0	-9.81	-9.074 + 2.597i
	-2.744	-5.349	12.005	0	-9.074 - 2.597i
	0.623	-1.697	-12.762	0	-0.086 + 0.462i
	0	0	1	0	-0.086 - 0.462i
2	-0.087	0.639	0	-9.81	-11.14 - 7.34i
	-1.505	-9.239	12.009	0	-11.14 - 7.34i
	-0.024	-1.413	-17.314	0	-0.051 + 0.791i
	0	0	1	0	-0.051 - 0.791i
3	-0.087	0.639	0	-9.81	-13.227 + 0.761i
	-2.744	-9.239	12.009	0	-13.227 - 0.761i
	0.651	-1.413	-17.314	0	-0.093 + 0.738i
	0	0	1	0	-0.093 - 0.738i

A dynamic stability analysis of the aircraft's lateral motion can be performed in the same manner. The relevant stability derivatives from both Napolitano's empirical equations and the XFLR5 analysis are in Table 13.

Table 13: Summary of aircraft lateral stability derivatives

Stability Derivative	Value from Equations	Value from XFLR5
C_{y_β}	-0.502	-0.280
$\boldsymbol{C_{y_p}}$	-0.052	0.050
C_{y_r}	0.470	0.290
$\boldsymbol{C_{l_\beta}}$	-0.027	-0.001
C_{l_p}	-0.278	-0.458
C_{l_r}	0.285	0.202
C_{n_β}	0.081	0.131
C_{n_p}	-0.124	-0.134
C_{n_r}	-0.551	-0.136

It can again be seen that in general the XFLR5 and the Napolitano equations agree in the sign and magnitude of the resultant stability derivatives, with the exceptions in bold. The first exception is in the dependence of the lateral force on the aircraft rolling rate, C_{y_p}. This coefficient is equivalent to the dependence of the lateral force on the aircraft sideslip angle due to the vertical tail, $C_{y_{\beta V}}$, multiplied by the vertical tail's lever arm on the aircraft center of gravity. $C_{y_{\beta V}}$ is the dominant portion of C_{y_β}. As the aircraft's wing and horizontal tail have dihedral angles equal to 0, and the wing is aligned with the centerline of the fuselage, this is the only non-zero portion of C_{y_β} for the aircraft (Napolitano, 2012). The lever arm is a positive distance, C_{y_p} and C_{y_β} should therefore have the same sign, which is the case for the equations and not the results from XFLR5. For this reason, the result from Napolitano's equations is assumed to be a more accurate representation of the system behavior.

Similarly, the effect of the sideslip angle on the aircraft rolling moment, C_{l_β}, was found to be different from these two sources. This dihedral effect should be significant, even though the aircraft's aerodynamic surfaces have no dihedral angles, as this coefficient represents the cross-coupling of rolling and yawing aircraft motion. Due to this, the XFLR5 value is considered to be untrustworthy in comparison to the value from Napolitano's equations.

In the same manner as the longitudinal states, three scenarios are examined for the lateral states. Scenarios 1 and 2 correspond to the results from Napolitano's equations and XFLR5, respectively. Scenario 3 corresponds to replacing the values of C_{y_p} and C_{l_β} obtained from XFLR5 with those from Napolitano's equations, as that was deemed to be a better source for these values. The state matrices and their eigenvalues for these scenarios are in Table 14.

Table 14: Comparison of Lateral A matrices for different scenarios

Scenario	A_{Lat}				Eigenvalues
1	-0.514	-0.041	-12.661	9.81	-3.582 + 4.122i
	-0.669	-5.626	5.540	0	-3.582 – 4.122i
	1.340	-1.342	-5.800	0	-5.009
	0	1	0	0	0.233
2	-0.287	0.040	-12.806	9.81	-1.568 – 5.805i
	0.021	-9.253	4.017	0	-1.568 +5.805i
	2.402	-2.051	-1.866	0	-8.577
	0	1	0	0	0.307
3	-0.287	-0.041	-12.806	9.81	-1.408 + 5.935i
	-0.644	-9.239	4.017	0	-1.408 – 5.935i
	2.3827	-2.051	-1.866	0	-8.825
	0	0	1	0	0.250

Although the magnitudes of the real parts of the eigenvalues are not consistent between scenarios, in all cases the same lateral modes are stable. Each scenario results in an unstable spiral mode, as indicated by the positive eigenvalue in each scenario. However, the real part has a small magnitude, meaning this is a slow mode that can be easily accounted for by the flight controller.

3.2. Aerodynamics and Structures

3.2.1 Aerodynamics

A suitable airfoil for the main wing was selected following criteria described in this section. After examining prior research papers, a chord of 0.25m was selected to do calculations to determine the airfoil for the aircraft (Waterman et al. 2019). After selecting this chord, the Reynold's number at varying cruise speeds could be calculated using Equation (40), from Anderson's *Fundamentals of Aerodynamics* (Anderson. 2011).

$$Re = \frac{V\rho c}{\mu} \tag{40}$$

Where μ is the viscosity of air at sea level and 25 °C and c is the mean wing chord. For the analysis of different airfoils, an angle of attack of 0 degrees was assumed. The Reynolds number was calculated using an assumed aircraft velocity of 10m/s, 12m/s, 15m/s, 20m/s, and 25m/s. The wingspan needed to carry the aircraft with payload was determined using Equation (41).

$$F = mg_y \tag{41}$$

Where g_y is the acceleration due to gravity and m is the max aircraft weight of 3 kg, resulting in 29.43 N of required lift. Thus, with a known required lift, coefficient of lift of the airfoil from XFLR5, and an assumed chord for the aircraft, the wingspan of the aircraft—b—could be calculated. This was done by solving for b with Equation (42).

$$L = \frac{1}{2} C_L v^2 bc \tag{42}$$

After calculating b, the aspect ratio could be calculated via Equation (43).

$$AR = \frac{b^2}{S} \tag{43}$$

Where S is the wetted area of the wing. After this, the span loading of the wing could be calculated. This was used to determine the induced drag on the aircraft and was calculated by Equation (44), where e is the Oswald Efficiency.

$$C_{di} = \frac{C_l^2}{ARe} \tag{44}$$

The stall speed for the airfoil was calculated, as seen in Equation (45). This used the weight of the aircraft, area of the airfoil, and maximum coefficient of lift.

$$V_{stall} = \frac{2L}{\rho S C_{L,Max}} \tag{45}$$

The tail of the aircraft was sized to ensure the resultant aircraft was statically and dynamically stable, as discussed in Section 3.1.3. Additionally, it was desired to have the horizontal tail to be higher than the main wing, as this reduces the effect of propeller downwash

on the aerodynamics of the aircraft (Bouquet and Vos, 2017). The resulting tail has the characteristics in Table 15.

Table 15: Properties of Aircraft Tail

Feature	Horizontal Tail	Vertical Tail
Airfoil	NACA 0009	NACA 0009
Chord, m	0.16	0.16
Span, m	0.477	0.16
Distance between aerodynamic center and wing aerodynamic center, m	0.695	0.695
Vertical distance from wing aerodynamic center, m	0.16	0
Horizontal distance from aircraft centerline, m	0	0.239

3.2.2 Control Surface Sizing

The control surfaces of the aircraft were designed based a combination of the requirements dictated by the mission and typical sizes on other aircraft. Ailerons control the rolling motion of an aircraft. One of the driving requirements for sizing the ailerons was the maximum rolling rate required to satisfy the mission. Due to the size of the airfield used in the competition, there were two ends of the flight path where the aircraft could fly at a constant heading for a far shorter distance between turns. During this distance, the aircraft would need to be able to roll out of the first turn to a level orientation and roll back to perform the next turn. Assuming the aircraft would spend this entire period of constant heading rolling, the minimum required roll rate was found with Equation (46).

$$l_{min} = \frac{2\phi V_{cruise}}{h_{field} - 2R_{min}} \tag{46}$$

Where ϕ is the bank angle required for the aircraft's minimum radius turn in radians, V_{cruise} is the cruise velocity in meters per second, h_{field} is the shorter dimension of the airfield and R_{min} is the aircraft's minimum radius of turn.Rudders control the yawing motion of an aircraft. This is achieved by deflecting the control surface by the angle δ_R, with the resulting yawing moment based on the dimensional control derivative N_{δ_R}. The initial size of the rudders was based on values found in literature and then iterated on to provide the desired behavior. Table 16 lists several properties of the rudders of the final aircraft design in comparison to bounds found from research (Sadraey, 2012).

Table 16: Comparison of aircraft rudders to properties from research (Sadraey, 2012)

Property	Minimum Value	Maximum Value	Final Value
Ratio of rudder chord to vertical tail chord, c_R/c_{vt}	0.2	0.62	0.25
Ratio of rudder surface area to vertical tail surface area, S_R/S_{vt}	0.145	0.61	0.4
Maximum rudder deflection in degrees, δ_R	±15	±31.6	±20

One of the primary requirements of the rudders was the ability to correct the heading of the aircraft while flying in a crosswind. Typically, this is done based on the stall speed of the aircraft to ensure the aircraft can takeoff safely. While this aircraft takes off vertically, the ability to correct for crosswinds during the transition up to cruise velocity is a similarly desirable trait to have.

Due to the coupling of roll and yaw, ailerons can induce an undesired yawing moment, while similarly rudders can induce an undesired rolling moment. To ensure the aircraft was sufficiently controllable, the two relations below had to be satisfied:

1. The rolling moment induced by the rudders at maximum rudder deflection had to be less than half the rolling moment induced by the ailerons at maximum aileron deflection, or $L_{\delta_R}\delta_{R,max} < \frac{1}{2}L_{\delta_A}\delta_{A,max}$
2. The yawing moment induced by the rudders at maximum rudder deflection had to be greater than twice the yawing moment induced by the ailerons at maximum aileron deflection, or $N_{\delta_R}\delta_{R,max} > 2N_{\delta_A}\delta_{A,max}$

The dimensional derivatives were all calculated based on the non-dimensional control derivatives, which were calculated with the same source used in Section 3.1 for stability analysis (Napolitano, 2012).

Elevators control the pitching motion of an aircraft. As this aircraft would not need to generate a pitching moment to perform a conventional takeoff, the elevator was sized primarily based on being able to allow for trim at the desired cruise conditions and to fit within a range of the typical sizes found in other aircraft.

Table 17 lists several properties of the elevators of the final aircraft design in comparison to bounds found from research (Sadraey, 2012).

Table 17: Comparison of aircraft elevator to properties from research (Sadraey, 2012)

Property	Minimum Value	Maximum Value	Final Value
Ratio of elevator chord to horizontal tail chord, c_E/c_{ht}	0.22	0.44	0.25
Ratio of elevator surface area to horizontal tail surface area, S_E/S_{ht}	0.185	0.61	0.25
Maximum upward elevator deflection in degrees, δ_{E-}	15.5	25	20
Maximum downward elevator deflection in degrees, δ_{E+}	0	25	20

During horizontal flight, the elevator is required to deflect in order to prevent a net pitching moment on the aircraft. To ensure control authority would still be present to deal with disturbances while also reducing the drag caused by the elevator deflection, it was desired to have this elevator trim angle have an absolute value within both of its maxima. For a horizontal velocity of 12 m/s, trim would require an aircraft angle of attack of 0 degrees and an elevator deflection of 20 degrees, which satisfied this requirement.

3.2.3 Structures

The use of ribs within a wing of this aircraft's size would only prove beneficial in defining the airfoil shape. This is because a majority of the structural support would come from the spar within the wing. A non-tapered wing yields a lower per-square-inch loading at the wing tips and is less likely to reach the conditions under which mainstream flow will separate (Basson, M. M., 2010). Due to being simpler to manufacture, a rectangular wing was selected. With this in consideration with the aircraft's low flight speed, it was also determined that the benefit provided by curved wing tips would not outweigh the cost of their contributed weight.

Matweb.com was used to obtain material specifications for analysis. Expanded polystyrene foam wings were chosen for their measured density and reported yield strength of about 49 MPa. A rectangular piece of this foam (30.6 x 15.3 x 1.4cm) was found to have a mass of 17 grams, yielding an average density of 0.026g/cm^3. This material could not be found within the default SolidWorks® database, so a new custom material was created using this data. In addition to its low cost, expanded polystyrene was chosen for the wings due to the ease with which it could be shaped. Alternative options, such as vacuum bagged composite wings, would take longer to create and thus could not be replaced quickly. Carbon fiber was selected for the

wing supports because of its strength and low density. Other options of support material were limited by the maximum weight of the aircraft, and thus only wooden spars that would not provide as much support were also considered.

It was decided that SolidWorks® would be used to design the aircraft frame. This software was chosen for its fluid and static analyses tools that allow simulation of an aircraft in flight. There is a large amount of community support found online to assist with any complex or unfamiliar design methods. SolidWorks® allows the parts of an assembly to contain the properties of desired materials to accurately represent the model. This capability was used to determine the appropriate size of a frame that would meet the mission's weight limit of 3kg.The WPI 3D printing services recommended that there be a minimum wall thickness of 4 mm in order to produce parts that would not be flexible. This requirement contributed to much of the weight of the aircraft. Despite its advantages, SolidWorks® had difficulty modeling the infill of 3D prints. As per the recommendations of the WPI 3D printing staff, a minimum wall thickness of 4mm was required to provide strong components. The fuselage also had to be separated into several components held together by nuts, bolts, and threaded inserts due to the size limitations of the 3D printers available.

Several components of the aircraft were assembled using slow curing epoxy purchased from West Systems. This was used to hold the tail components within the 3D printed parts, attach nuts to the inside of the support spars, and mount the control surface hinges to the wing. Threaded inserts used in the fuselage and wing links were chosen after research had shown that they could withstand greater forces than printed threads (CNC Kitchen, 2019). These assembly methods were all that was needed to hold the aircraft components together and maintain their orientation during flight.

3.3. Autonomy and Control

3.3.1 Hardware Selection Criteria and Survey

This subsection describes the procedures used to select the hardware components used by the autonomy subsystem first introduced in Section 2.3.

A flight controller is a circuit with sensors and is used to control the orientation, speed, altitude, and the heading of an aircraft. These on-board sensors could include a gyroscope, accelerometers, magnetometer, GPS, and a barometer. A flight controller also uses a receiver module to wirelessly connect with a transmitter module to receive commands from a pilot or user. There are numerous flight controllers on the market, making it necessary to develop a rubric for selecting the best flight controller to accomplish the mission of this project. The rubric developed was divided into four parts:

1. Performance and built-in sensors: Performance of the aircraft depends on the performance of a Microcontroller Unit (MCU) used in a flight controller circuit. A delay in the computations can result in a delayed feedback loop, harming aircraft performance.
2. Dimensions and weight: This portion of the rubric was created to satisfy the project goal of maximizing the payload fraction. Smaller hardware is preferable as it can fit into a smaller, lighter fuselage. Likewise, the more weight devoted to electronics, the less payload can be carried.
3. Power consumption: The endurance of the aircraft was primarily driven by the aircraft's total power consumption. Power consumed by the flight controller and other hardware is power that could otherwise be used by the motors to achieve the mission. Thus, minimizing this quantity serves to achieve the project goal of maximizing the aircraft's flight time.
4. Interfaces and other required features: Additional hardware, as described in the following sections, would be required with the flight controller circuit to accomplish the mission defined in the Section 2.3. Having suitable and enough interfaces will make it easier to assemble the circuit and would not require any circuit extensions to accommodate the additional hardware.
5. Community Support/ Popularity: This hobbyists' community support also played a key role in finalizing the flight controller. Having a large community base with active discussion groups makes the process of troubleshooting more efficient by providing access to already existing solutions for commonly faced problems.

Based on the rubric, a survey of different microcontrollers in the market was conducted to find the most suited flight controller to achieve the goals and objectives of this project. The four parts of the rubric were evaluated for different flight controllers available in the market to finalize the controller that was used for the project. Table 18 compares parts 1 and 4 of the rubric, while Table 19: Comparison of flight controller dimensions, masses and costs compares part 2 of the rubric.

Table 18: Comparison of Flight controller microcontrollers, interfaces, and sensors

Flight Controller	MCU	Interfaces	Sensors
Pixhawk	STM32	C, S, A, PP, SB, DS	B, M
Pixhawk 2	STM32	C, S, A, PP, SB, DS	B, M
PixRacer	STM32	C, PP, SB, DS	B, M
Pixhawk HKPilot 32	STM32	C, S, A, PP, SB, DS	B, M
Pixhawk 4	STM32	C, S, A, PP, SB, DS	B, M
Pixhawk 3 Pro	STM32	C, S, PP, SB, DS	B, M
PX4 FMUv5 and v6	STM32	C, S, A, PP, SB, DS	B, M
Sparky2	STM32	C, PP, SB, DS, DA	B, M
CC3D	STM32	PP, DS, SB	None
FlyMaple	STM32	None	B, M
Beagle Bone Blue	Octavo OSD3358	S, DS, A	B, M
Erle-Brain 3	Raspberry Pi	A	B, M
Atom	STM32	PP, DS, SB	None
APM 2.8	ATmega2560	PP, A	B
Qualcomm Flight Pro	Qualcomm Kryo Quad-core	C, S, A, DS	B, M
Chimera	STM32	C, S, A, DA, PP, SB, DS, X, AU	B, M, P

Interfaces: C- CAN, S- SPI, A – ADC, PP – PPM, SB – SBUS, DS – DSM, DA – DAC, X- XBEE, AU – AUX

Sensors: B – Barometer, M – Magnetometer, P – Pitot Tube

Table 19: Comparison of flight controller dimensions, masses and costs

Flight Controller	Dimensions (mm)	Mass (grams)	Cost ($)
Pixhawk	81.5 x 50 x 55	38	73
Pixhawk 2	38.5 x 38.5 x 23	39	199
PixRacer	36 x 36 *	10.9	119
Pixhawk HKPilot 32	81 x 44 x 15	33.1	120
Pixhawk 4	84 x 44 x 12	15.8	250
Pixhawk 3 Pro	71 x 49 x 23	45	250
PX4 FMUv5 and v6	71 x 50 x 55	45	250
Sparky2	36 x 36*	13.5	30

CC3D	36 x 36*	8	20
FlyMaple	50 x 50 x 12	15	70
Beagle Bone Blue	81.5 x 50 x 55	37	95
Erle-Brain 3	95 x 70 x 23.8	100	199
Atom	15 x 7*	4	16
APM 2.8	70.5 x 45 x 13.5	31	50
Qualcomm Flight Pro	75 x 26*	25	949
Chimera	89 x 60*	-	-

*: Board without any enclosure. Height is the sum of thickness of the PCB and the electronic components.

After the survey, based on the available interfaces and sensors present and the popularity in the hobbyist community, the Pixhawk series flight controllers were shortlisted. Out of the Pixhawk series, the Pixhawk HKPilot 32 and Pixhawk 4 were the most suitable flight controllers for the project. The Pixhawk HKPilot 32 was finalized because it had similar specifications to the Pixhawk 4 but at a lower cost of $120. The Pixracer would have been a good choice but it is modified to be used in small racing quads, which is not the purpose of this project.

A companion computer was used to expand the applications of the flight controller by providing processing power to enable autonomous navigation and robotics technologies. This project, as mentioned in Section 1.2, has the main goal of maximizing the score by showing autonomy capabilities mentioned in Section 2.3. Fulfilling these autonomy capabilities would require the development of software that will run computer vision and trajectory generating algorithms. Choosing the companion computer required a performance analysis, which is done by comparing data from different benchmarking tests for selected companion computers. These tests included measures of:

1. CPU – Single Core Performance
2. CPU – Multi Core Performance
3. RAM – Read and Write Speed
4. Flash Memory – Data Transfer speed
5. Graphics Processing Speed (2D)
6. Power Consumption
7. Deep Learning Interference

Other than benchmark tests, it was important to choose a companion computer that is compatible with the additional hardware, such as the camera and LIDAR. The two companion computers examined was the Jetson Nano and Raspberry Pi 4B. The two companion computers that were most relevant for the application were the Jetson Nano and Raspberry Pi 4B. The two had similar processing and power characteristics. The Jetson Nano, however, is optimized for graphic processing, which helped with the target detection during autonomous flight.

Cameras can be used for applications like aerial photography, object detection, obstacle avoidance, and mapping. Each of these camera applications require different specifications to give optimal results. In this project, the camera was used for target detection with the help of computer vision software. To choose the best camera for this application, different guides on choosing the right computer vision were used and a list of questions was made to find a set of camera specifications suitable for this project. These questions are as follows:

1. What is the aim of inspection?
2. What characteristics are necessary to successfully perform the desired inspection?
3. Which image sensor will be the best for the application?
4. Does it have the communication interface to be able to connect and transfer data to the main system?
5. Is it readily compatible with the companion computer?

These questions aimed to address all the concerns that might increase the work in future and helped to choose the best camera for this project. After going through the questions, the following set of specifications were finalized for a camera selection:

1. Complementary Metal Oxide Semiconductor (CMOS) sensor camera: compared to a Charged Coupling Device (CCD) camera, CMOS cameras tend to be cheaper, while also having better low-light performance. CMOS sensors also have a higher read rate than CCD sensors.
2. High frame rate per second (60 FPS): As the aircraft may be moving a high velocity when the target detection algorithm begins, it is important that the Fiducial Markers can appear in as many frames as possible.

3. Resolution optimized for high frame rate: The aircraft's position cannot be determined if the fiducial markers cannot be resolved. Given the tag must be recognized while the aircraft is at cruise altitude, a high camera resolution is required.
4. CSI interface: This interface between the camera and companion computer would allow for fast image data transfer.
5. Compatibility with Jetson Nano: To reduce the future workload, it was important the camera and companion computer were compatible. This characteristic was given highest priority, since last year's VTOL MQP emphasized on the compatibility factor of peripheral devices.

After considering the compatibility factor, the list of available cameras was reduced from overwhelming numbers to

To maintain the altitude during flight and make decisions based on height measurements, an altitude measurement sensor was used in this project. Different technologies, such as Ultrasonic sensing and Infrared sensing, can be used for measuring distance. To select an optimal sensor for the project the following factors were taken into consideration:

1. Technology being used (Ultrasonic or IR ranging)
2. Accuracy of the sensor: The accuracy of the altimeter should be at least an order of magnitude smaller than the cruise altitude of the aircraft.
3. Compatibility with the companion computer
4. Cost: although a high-performance sensor is preferable, a sensor that is far cheaper or even already available in the lab would better accommodate staying under budget.

These questions were used to find an altitude measurement sensor that was reliable, accurate, and easily integrated with existing prior hardware selections. The largest factor in selecting the sensor was their cost and compatibility with selected companion computer.

3.4. Power and Propulsion

The competition rules constrained several design decisions related to power and propulsion. Quadcopters quickly drain through their battery to sustain flight due to the necessity of constantly running motors to maintain altitude (Xu. 2017). The voltage, power output, and energy capacity of batteries limit the type of motors that can be used on the aircraft and can affect their performance. Based off the Autonomy and Control hardware selections discussed in Section 3.3, a table of power requirements was created, seen in Appendix A. This table was used to determine a compatible battery and motors.

3.4.1 Power

In accordance with the 2020 WPI UAV Competition, several constraints were put on the battery that could be selected for the project. The prior year VTOL MQP used a 4S battery, which had a capacity of 3250 mAh and could provide 14.8 volts to the aircraft (Waterman et al 2019). This year's project was limited to a 3S, 2200 mAh battery, which had a voltage of 11.1V. Additionally, the rules required the use of a 1000W power limiter, which prevented any aircraft from using more than that amount of power. These design constraints limited the batteries that were examined, a list of which is provided in Table 20. The cells highlighted in pink denote power outputs that the batteries could provide but exceeded that allowed by the power limiter. Thus, for the purposes of this project, these batteries could only output 1000W of power.

Table 20: Batteries considered

Battery	Discharge, C	Current. A	Max Power, W	Mass, kg	Length, mm	Width, mm	Height, mm
ZIPPY Compact	40	88	976.8	0.196	109	34	27
Turnigy 40C	40	88	976.8	0.204	104	27	35
Turnigy nano-tech 45~90C	45	99	1098.9	0.201	112	36	26
Turnigy Graphene 45C	45	99	1098.9	0.211	106	35	30

In addition to powering the motors selected for propulsion, which are discussed in Section 3.4.2, the aircraft's battery had to also power the electronics selected for autonomy and other hardware. These power requirements are depicted in Table 22 and Table 23 in Appendix A.

A Power Distribution Board (PDB) was used to supply power to the different components of the circuit. A PDB has several connection ports or soldering pads and a battery eliminating circuit (BEC) for regulating the voltage supplied to different components. There were two criteria for selecting a PDB. The PDB had to be rated above the maximum current drain from the subsystems. This maximum current drain was calculated based on current rating at the peak power drain condition of the electronic components. This quantity is usually listed on the website of the hardware component and can also be found in Appendix A in Table 22. Since there are three main flight modes-take-off/landing, transitioning to horizontal flight, and horizontal flight--the power requirements of each phase were calculated. In addition, the PDB should have enough ports to connect all the components of the system.

3.4.2 Propulsion

Assessing the power consumption of the motors and onboard electronics was necessary to determine the time of flight of the aircraft. A thrust to weight ratio of one and a third was assumed for selection of the vertical motors. Since the load would be distributed between four motors during the VTOL regime, several motors were found that generated 975 grams of thrust around 70% throttle. To reduce the number of different components used on the aircraft, the same motor model was selected for a horizontal pusher motor and the vertical motors. Using this information, several motors were considered, as seen in Table 21. The manufacture thrust stand test data was used for propeller selection. In addition, several propellers were found in the lab and used for the vertical motors.

Table 21: Motors considered

Motor Type	Current, A	Power, W	Efficiency, G/W	Mass, Kg	Thrust, Kg	Throttle, %
EMAX MT2213-935KV	8	88	6.7	0.053	0.59	80
EMAX MT4008-600KV	12	133.2	7.4	0.093	0.98	83.33
EMAX MT3510-600KV	12	133.2	8	0.102	1.02	77.5
Cobra CM-2820/16	16.1	150	6.7	0.146	1	70
T-Motor AT2814	11.45	172.98	5.9	0.108	1.021	60
T-Motor AT2317-1400KV	11.04	211.93	8.8	0.08	1.061	70

Motor Type	Current, A	Power, W	Efficiency, G/W	Mass, Kg	Thrust, Kg	Throttle, %
T-Motor AT2321	16.26	177.18	5.96	0.093	1.055	60

Electronic speed controllers are used to control the speed of the motors. Like the selection of the PDB, it was necessary to ensure that the ESC can handle the peak current drain of the motor. This is usually listed as maximum current rating in the specifications of the motors. At the same time, lightweight ESCs were desirable, as they would have the least impact to the aircraft's payload fraction.

4. Experimental Results

4.1. Glide Testing

As per WPI competition rules, a glide test was conducted prior to the competition flight. Initially, a scale model 40 percent the size of the actual aircraft was made with the intention of being used for glide testing. This aircraft is shown in Figure 42.

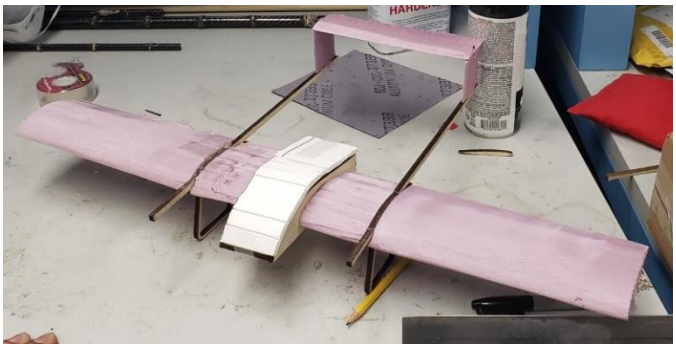

Figure 42: Scale model aircraft

However, it was found that this aircraft was too fragile for practical testing purposes, likely because the wings were not internally reinforced like on the full-scale design. As a result, a full-scale aircraft was created for glide testing, which is depicted in Figure 43. Due to time constraints, the 3D printed fuselage was replaced with pieces of laser-cut plywood and cardboard that were epoxied together.

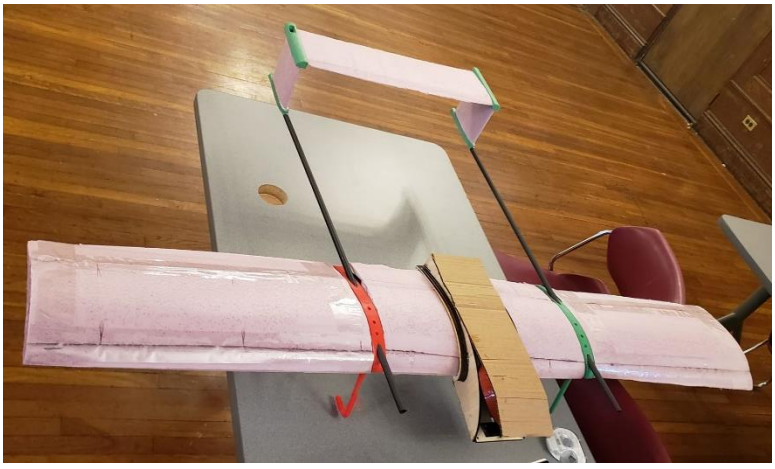

Figure 43: Glide test aircraft

Figure 44 depicts the angular velocities of the aircraft during the glide test. The only axis about which the aircraft spins a significant amount is the pitch axis. This makes sense, as the aircraft pitched down slightly but otherwise did not deviate significantly from its initial heading.

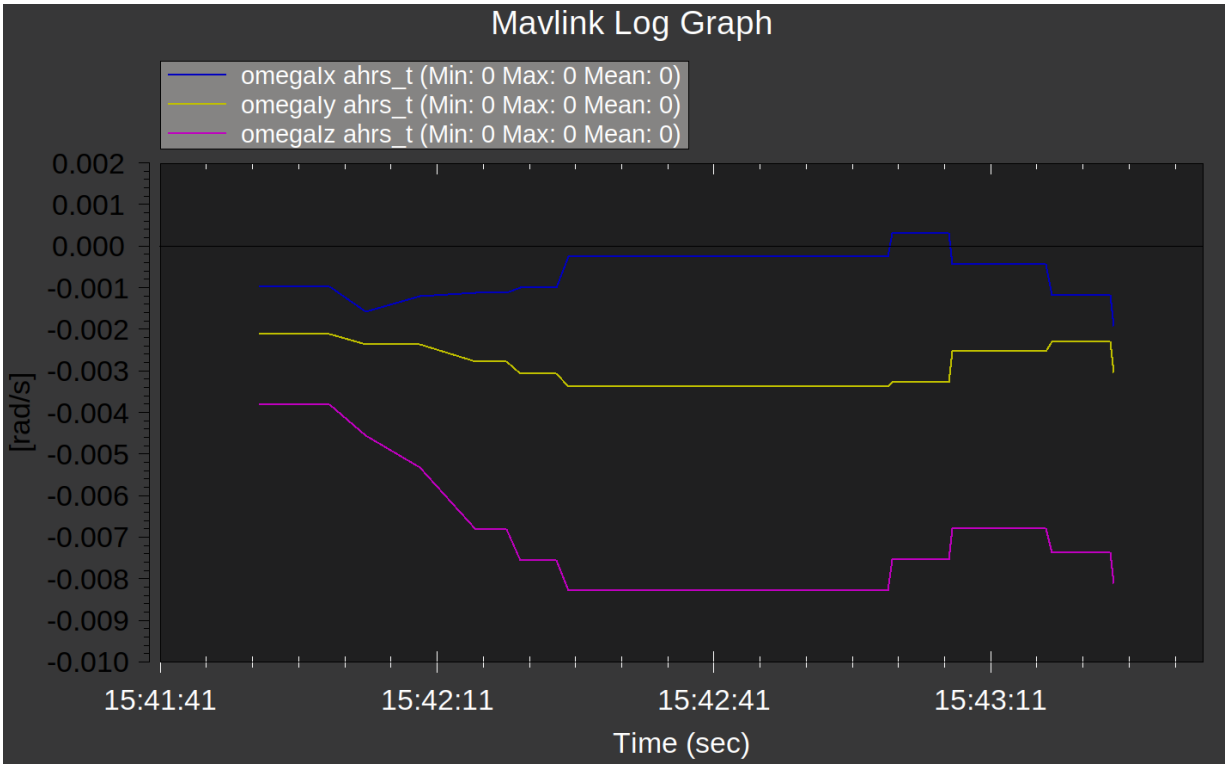

Figure 44: Aircraft angular velocities during the glide test

Figure 45 shows the pitch and roll of the aircraft during the glide and Figure 46 shows the yaw of the aircraft. Both of these plots depict grossly inaccurate attitude measurements of the aircraft. This inaccuracy was attributed to a weak telemetry connection.

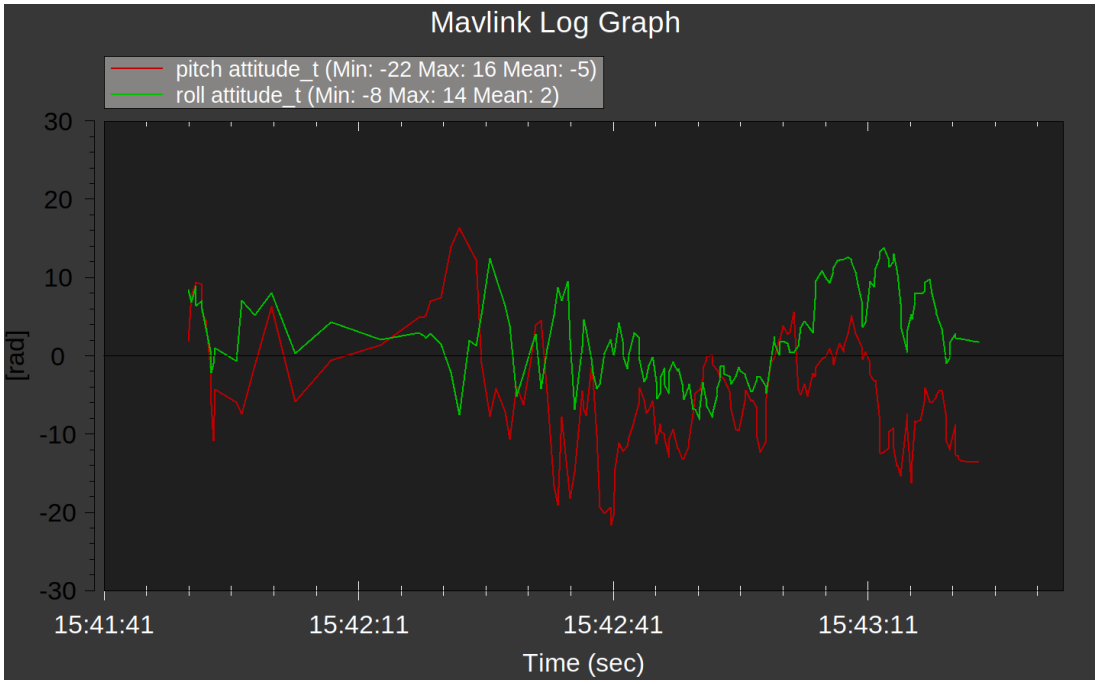

Figure 45: Aircraft pitch and roll attitude during the glide test

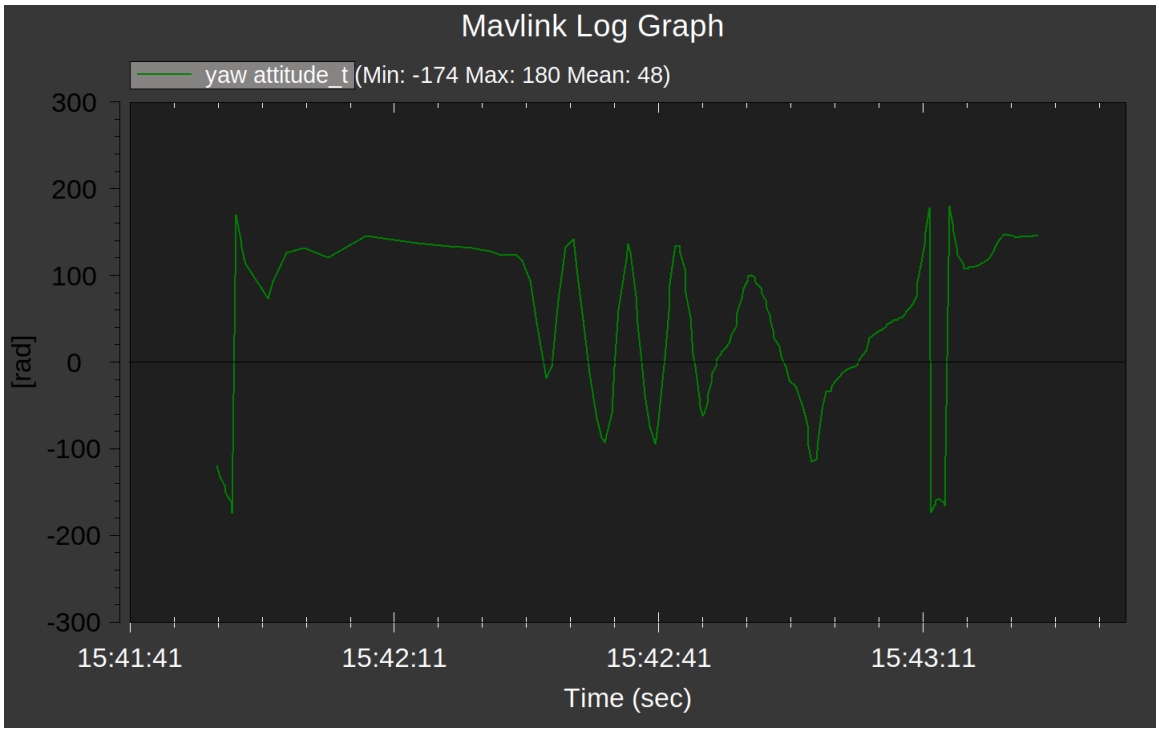

Figure 46: Aircraft yaw attitude during the glide test

Seen below in Figure 47, the Euler angles of the glide test remained small, with only larger magnitudes being experienced in the middle of the test. This may be the result of noisy data collection.

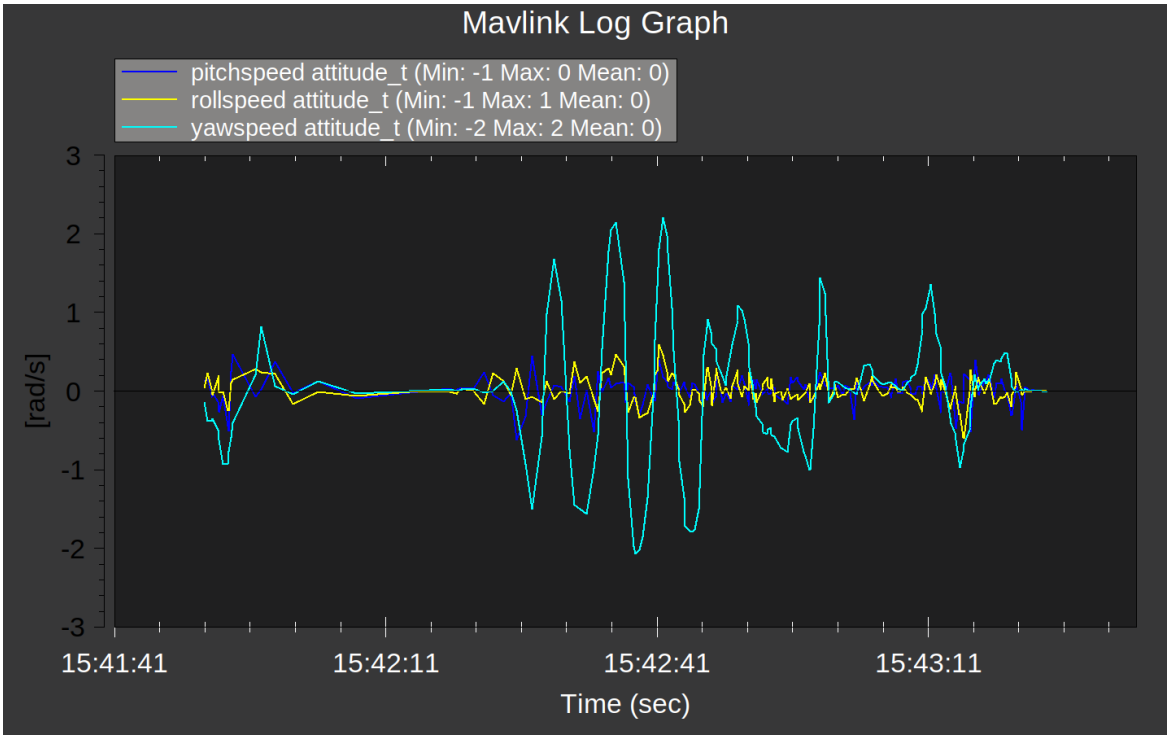

Figure 47: Aircraft rates of change of Euler angles during glide test

4.2. Design Modifications

During the construction of the aircraft, several design modifications where made. During the validation of the aircraft's static stability, a new equation for the Coefficient of Pitching Moment was derived to take into consideration the horizontal tail's position above the center of mass. It was found that this decreased the static margin and caused the aircraft to become statically unstable. Several solutions were examined. Due to the completion of the 3D prints, it was determined that the tail size would not be increased. Moving the tail back would move the neutral point backwards. However, moving the tail by 10 cm would only move the neutral point 1 cm, which was determined to be ineffective. Lastly, the re-arrangement of ballast and onboard electronics was considered. This was selected as the solution to increase the stability of the

aircraft, as it did not require 3D printing new parts. The maximum location of the center of gravity was determined to be .55 the length of the chord on the main wing, as seen in Figure 48.

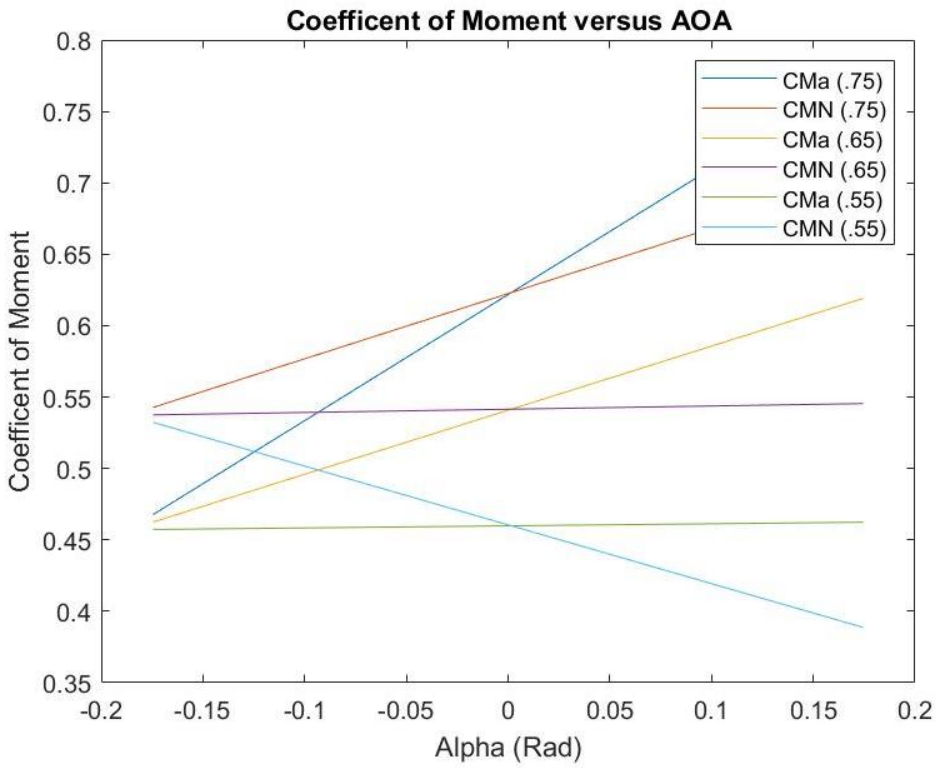

Figure 48: Effect of Varying Center of Gravity Location on Coefficient of Moment vs. Angles of Attack

To achieve this desired center of gravity position, the battery moved forward to under the nose of the aircraft. The internal electronics were also moved forward inside the fuselage. With these adjustments, along with the new center of gravity requirements, it was found that the ballast and its supporting rod were no longer needed, which allowed the empty mass of the aircraft to be reduced.

During the first hover test, the aircraft experienced a fast spin about the yaw axis. To reduce this effect, the airframe of the aircraft was reinforced with PVC piping to prevent the wing carbon fiber tubes from displacing under loads. Additionally, the inner foam wings were adhered to the fuselage to increase the overall structural rigidity. After additional hover tests, it was found that the propeller selection could be optimized to generate higher thrust at lower throttle levels. Using ecalc, a new propeller shape was selected using the project's known battery, ESCs, and motor type. This can be seen in Figure 49. A 10x6 propeller from APCpro

was selected due to its higher thrust to weight ratio. The maximum current per motor is over the ESC limit of 30 A at maximum throttle, but this is only a concern for high throttles above what the aircraft requires for hover.

Motor @ Maximum	
Current:	36.51 A
Voltage:	8.62 V
Revolutions*:	10122 rpm
electric Power:	314.6 W
mech. Power:	254.3 W
Power-Weight:	419.5 W/kg
	190.3 W/lb
Efficiency:	80.8 %
est. Temperature:	48 °C
	118 °F
Wattmeter readings	
Current:	146.04 A
Voltage:	8.91 V
Power:	1301.2 W

Motor @ Hover	
Current:	14.62 A
Voltage:	10.11 V
Revolutions*:	7008 rpm
Throttle (log):	59 %
Throttle (linear):	59 %
electric Power:	147.8 W
mech. Power:	118.6 W
Power-Weight:	216.3 W/kg
	98.1 W/lb
Efficiency:	80.3 %
est. Temperature:	36 °C
	97 °F
specific Thrust:	5.08 g/W
	0.18 oz/W

Figure 49: Propeller Selection

After further hover testing, the propeller replacements were found to be enough to achieve takeoff. However, during one hover test one of the landing legs broke as the aircraft landed with a significant sideslip velocity. As this damage occurred late in the project, there was not enough time to 3D print new legs. Instead, the legs were repaired and reinforced with foam and epoxy. This fix proved effective, as the aircraft was later able to survive several landings without damage. The final aircraft and its mass are depicted in Figure 50. Although the empty mass of 2950 g essentially prevented the aircraft from carrying any payload, it was still below the maximum takeoff mass allowed by the competition.

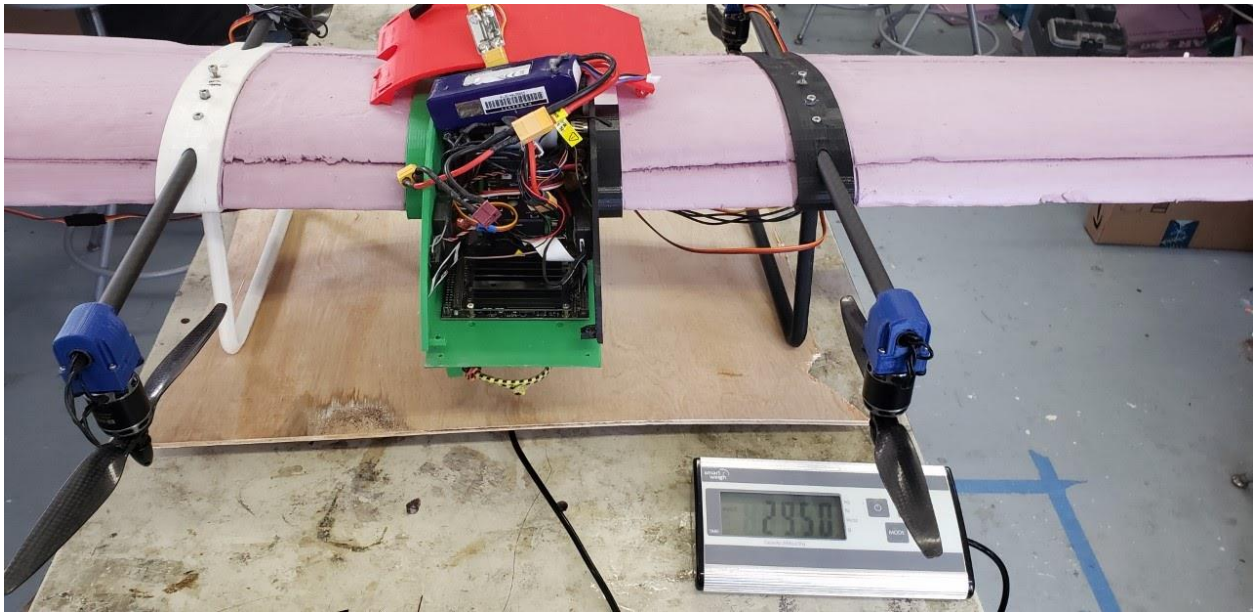

Figure 50: Final Mass of Aircraft

4.3. Bench Testing

These tests were a series of ground tests to validate the aircraft design and onboard electronics. Several tests were conducted to verify the target identification and path planning of the aircraft.

4.3.1 Aruco Markers and 3D Pose Estimation

In order to deliver a payload autonomously, this project team sought to design a system that could identify a target location and give the target's position relative to the aircraft. An Aruco marker was selected as the identifying marker. For the test, the Aruco Marker was held 10 meters way from the camera. The camera was able to identify the Aruco Marker at this range, seen in Figure 51.

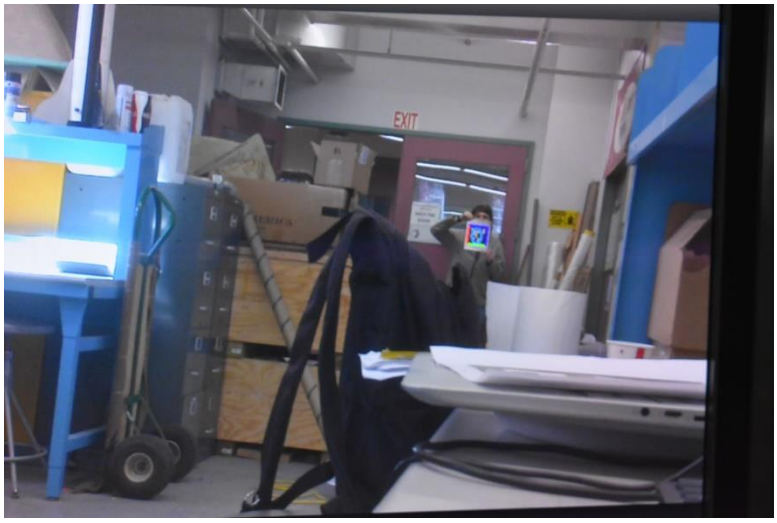

Figure 51: Camera Aruco Marker Bench Test

4.3.2 Payload Drop Test

After mounting the payload deployment system to the aircraft, the deployment system was tested. This test involved closing the support ties and activating the servo for payload deployment. This can be seen in Figure 52.

Figure 52: Payload Drop Test

4.4. Flight Testing

Once the system was verified on the ground, the individual legs of the final mission could be carried out. These tests initially focused on being controlled by a human pilot, with the intention of eventually implementing autonomy where possible.

4.4.1 Hover Testing

This test had a similar structure to the bench test of the aircraft motors. However, in this test the propellers were installed onto the motors. As the ESCs had been previously calibrated, this action was not required again. This was done over several flights to permit the vertical motors to be balanced around the center of gravity. To conduct the test, several 9x4.5 propellers were used, acquired from the project lab. The aircraft was armed and flown outdoors. The first hover test can be seen in: *https://www.youtube.com/watch?v=GDmhadpi9Gs*.

Figure 54 show the results of the flight test, in which the aircraft conducted several hovers about a meter off the ground. A high yaw rate was found, while the pitch rate tended to stay close to zero. This was determined to be the result of a loose airframe and lack of vertical tail. Roll was excluded to the graph due to one spike of -7000 mrad, which expanded the scale of the graph and prevented the other values from being read.

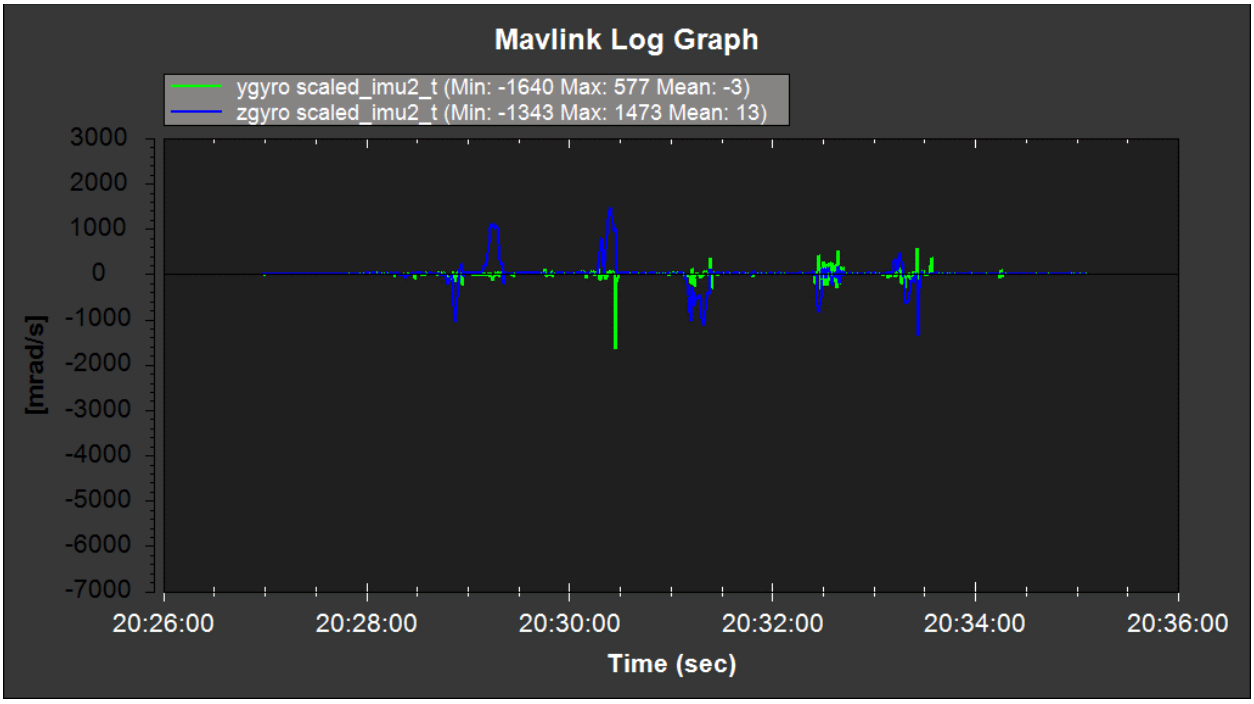

Figure 53: Hover test pitch and roll rates

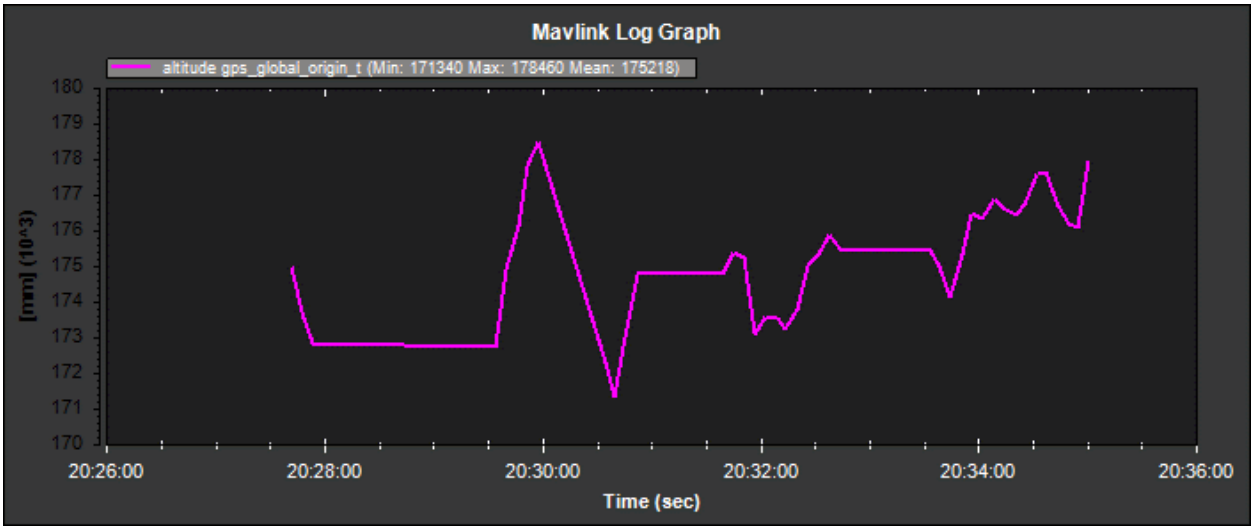

Figure 54: Hover test altitude data

Another flight mode, Quadcopter Hover (QHOVER), was tested by this MQP team. This was done at the RC Field in Medfield, MA. During this flight test, the gains of the throttle controller were also adjusted. The aircraft was flown and put into QHOVER mode by the pilot, which regulates the altitude, pitch, and roll of the aircraft. The aircraft's altitude throughout this flight is depicted in Figure 55, reaching a peak altitude of 10 meters. The attitude behavior of the aircraft during this flight can be seen below in Figure 56. Due to a structural failure during the flight, the yaw rate can be seen suddenly increasing towards the end of the flight until the aircraft reaches the ground.

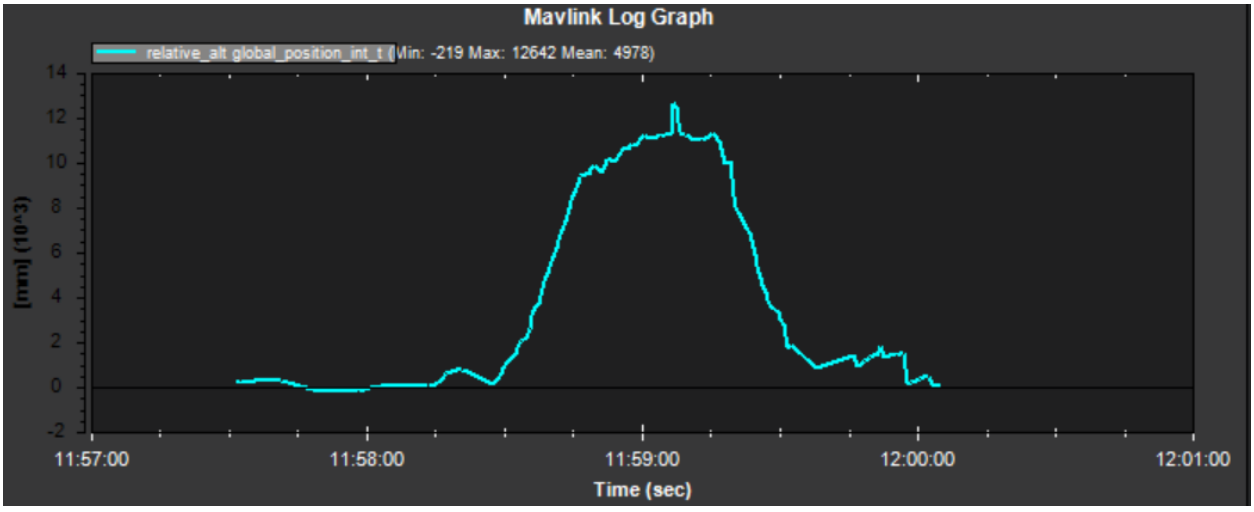

Figure 55: Altitude of aircraft during final hover test

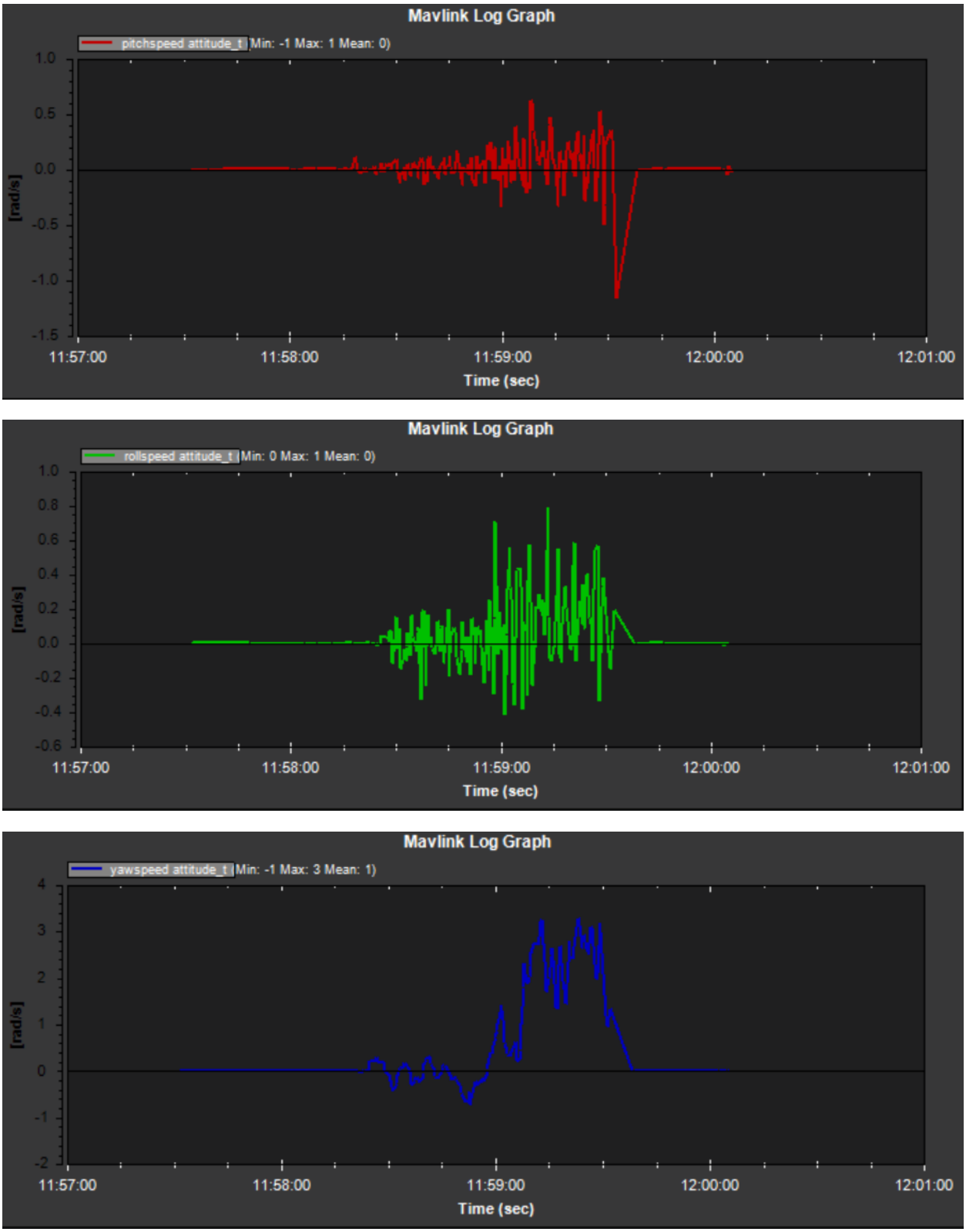

Figure 56: RC Field Test Data. Top to bottom: pitch rate, roll rate, yaw rate

This test showed in This is seen in https://www.youtube.com/watch?v=U_KxrMokt_Q&feature=youtu.be, displayed that the aircraft could maintain a stable altitude. The pilot still had control of the throttle setting and if the throttle was not set to 50% the aircraft would climb or descend in altitude. For most of the flight the aircraft had low pitch, roll, and yaw speeds. Upon landing, it was discovered one of the carbon fiber tubes supporting a front VTOL motor had become loose. As a result, the thrust direction of the motor was tilted outwards by several degrees rather than inwards as intended, reducing the yaw authority of the aircraft. This can be seen in the test video, in Appendix C: Hover Test Information.

The transition to Fly By Wire (FBWA) was tested on the ground. During the test, the aircraft mode was changed from QHOVER to FBWA using the radio transmitter. This began a process that had the horizontal motor spin up as the VTOL motors spun down. Due to the aircraft remaining on the ground stationary, the horizontal motor reached its maximum thrust while the VTOL motors did not stop, since the mode required the aircraft to reach the cruise speed of 12m/s before turning off the vertical motors. This can be seen in Appendix D. Another hover test conducted showed that the aircraft's yaw, pitch and roll rate could be controlled. This is shown in Appendix C, along with additional graphs produced by the test.

4.5. Conclusions

Overall, this project had some success in designing and building a hybrid VTOL aircraft. Due to improper motor selection, the aircraft's ability to hover efficiently was inhibited. The motors that were purchased were both less efficient and capable of a lower maximum thrust, meaning a higher throttle setting was required to takeoff. Additionally, a last-minute redesign was required to address SolidWorks® changes that made the aircraft statically unstable. Had the tail been larger and if the aircraft's center of gravity remained in a more consistent place throughout the iteration process, it is likely this issue would not have occurred. Finally, due to several manufacturing factors, the empty mass of the aircraft exceeded that of the SolidWorks® model by 200 grams, a significant amount relative to the maximum takeoff mass. This was likely due to epoxy and wiring not being adequately accounted for in the model.

Although problems were encountered along the way, the overall design process used in this project had merit. By learning from the compatibility issues of the previous year's MQP and relying on the inherent capabilities of the flight controller rather than designing our own control algorithm, the testing of the aircraft's electronics and software was greatly expedited. Likewise, the toolbox initially designed was useful to predict the score of the aircraft for the mission, but beyond initial determination of the aircraft's airfoils and motors it was not used for its full potential. If a future project creates a similar analysis tool, extensive trade studies that utilize this toolbox—such as finding the cruise speed that can maximize the product of payload fraction, cruise speed and flight time—would use it to its fullest extent.

As the project was drawing to a close, hover tests proved invaluable for identifying issues in the overall aircraft design and ensuring the software worked as intended. While stability analysis could indicate issues with the aircraft during horizontal flight, the easiest to find instability during quadcopter flight was through conducting actual flights.

In general, this project benefitted from selecting a relatively simple design in comparison to previous work. A VTOL aircraft is inherently complex, so a variety of issues still arose during construction.

4.6. Recommendations for Future Work

Making a subscale model can be useful to get a sense of the proportions of the aircraft or to become familiar with the manufacturing techniques involved. However, the wings for the scale model, made of expanded polystyrene, were too thin and resulted in a fragile structure. This project team found that future projects should start prototyping a full-scale model as soon as a basic design has been developed. Future teams should plan to make several design iterations. Gaining experience with cutting foam will improve the quality of wings over time. Several parts had issues initially fitting together, an issue that was only obvious once assembly had started. Likewise, the initial fuselage design was not well-suited to housing the aircraft's electronics, an issue that was not apparent until a prototype of the aircraft circuitry was built.

While 3D printing allowed for parts with complex shapes to be manufactured, parts must be designed to be easily printed. Otherwise, support structures must be employed during the print

which can sometimes be hard to remove. The print bed dimensions and restrictions on the availability of on-campus 3D printers limited the maximum size of parts that could be printed. As a result, the fuselage of the aircraft had to be split into several pieces, while connecting these pieces together required further design changes. Due to these considerations and general time constraints, several parts of the glide test aircraft were made of laser cut birch wood rather than 3D printed PLA. The cost of 3D printing also grew rapidly towards the end of the project, due to rapid design iterations and the need for modified parts. Finally, in the case of the aircraft legs, 3D prints with a low infill proved to be extremely fragile if not reinforced. Overall, future projects could benefit from a thorough review of material properties when designing an aircraft.

The aircraft's empty mass was a persistent concern throughout the duration of the project. This challenge arose when the need for a ballast was considered to adjust the aircraft's static stability. Likewise, during final construction the aircraft was found to have a higher mass than calculated in SolidWorks®. This was possibly due to the cumulative mass of a variety of small components, such as wiring, and the adhesives used to attach bigger pieces together. Future teams should ensure that design modifications in SolidWorks© are verified by stability and structure sub-teams. The aircraft should be weighed regularly during construction, or each sub-section weighed.

A lack of structural rigidity was a frequent issue during this project, especially when trying to fly the aircraft like a quadcopter. Future VTOL projects must be able to balance being able to disassemble the aircraft for repairs or transport with permanently attaching key components together with epoxy or other adhesives. For example, if a future team uses a VTOL motor mounting scheme like this project, they should adhere the motor mounts to carbon fiber tubes once the aircraft center of gravity is well defined.

This team found that flight tests of the aircraft helped to identify manufacturing issues and other defects in the aircraft. Flight testing even a partially assembled aircraft allowed for modifications that made the quad-plane more stable in flight. Future teams should flight test as early as possible to remedy issues as they arise and assume tests will take longer than planned.

In addition, a discussion with members of the RC Club members in Medfield, it was suggested that future aircraft have a wing dihedral to increase roll resistance. The members also

said that checking the center of gravity of the aircraft and ensuring stability were crucial before test flights.

5. References

5 Ways Drones are Being Used for Disaster Relief. Eastern Kentucky University. Retrieved from https://safetymanagement.eku.edu/blog/5-ways-drones-are-being-used-for-disaster-relief/

ALTI Ascend (2019). Retrieved from https://www.altiuas.com/ascend/

Anderson, John D. Fundamentals of Aerodynamics. 5th edition. Mc Graw Hill. 2011.

ArduPilot: QuadPlane Overview (2019). Retrieved from https://ardupilot.org/plane/docs/quadplane-overview.html

Ashley Antoninette Smith, Benjamin Matthew Andrews, Casey Tucker Brown, Christopher James Cahill, Daniel Dean Thiesse. Design and Optimization of a Micro-Aerial Vehicle. Worcester Polytechnic Institute. Digital WPI. April, 2016

Basson, M. M. (n.d.). Stall Prevention Control of Fixed-Wing Unmanned Aerial Vehicles. Retrieved from https://pdfs.semanticscholar.org/738b/923153397ac8dbdb70078845ac634e753db3.pdf

Bouquet, T., & Vos, R. (2017). Modeling the Propeller Slipstream Effect on Lift and Pitching Moment. In 55th AIAA Aerospace Sciences Meeting: Grapevine, Texas [AIAA 2017-0236] AIAA. https://doi.org/10.2514/6.2017-0236

Camera Module V2 (2019). Retrieved from https://www.raspberrypi.org/products/camera-module-v2/

Chen, C., Zhang, J., Zhang, D., & Shen, L. (2017). Control and flight test of a tilt rotor unmanned aerial vehicle. International Journal of Advanced Robotic Systems, 14(1). https://doi.org/10.1177/1729881416678141

Chahl, J. (2015). Unmanned Aerial Systems (UAS) Research Opportunities. Aerospace, 2(2), 189–202. https://doi.org/10.3390/aerospace2020189

Chowdhury, A. B., Kulhare, A., & Raina, G. (2012, May). Back-stepping control strategy for stabilization of a tilt-rotor uav. In 2012 24th Chinese Control and Decision Conference (CCDC) (pp. 3475-3480). IEEE.

Connolly, K. (2016). Drone Delivery Is Ready to Take Flight. Design News, 71(9). Retrieved from http://search.proquest.com/docview/1832994328/

CNC Kitchen. (2019, May22). Threaded Inserts in 3D Prints – How strong are they? [Video File]. https://www.youtube.com/watch?v=iR6OBlSzp7I

D'Andrea, R. (2014). Guest Editorial Can Drones Deliver? IEEE Transactions on Automation Science and Engineering, 11(3), 647–648. https://doi.org/10.1109/TASE.2014.2326952

DHL ParcelCopter (2019). Retrieved from https://www.dpdhl.com/en/media-relations/specials/dhl-parcelcopter.html

Drone Base (2020). Retrieved from https://dronebase.com/

Flinger, Montrallo Daniel, Igor Cherepinsky. *Unique Challenges in VTOL Autonomy*. Lecture. Worcester, WPI. 2019

FAA Continues Progress Towards Integration into the National Airspace. Government Accountability Office. July 2015. Retrieved from https://www.gao.gov/assets/680/671469.pdf

Flores-Colunga, G. R., & Lozano-Leal, R. (2014). A nonlinear control law for hover to level flight for the quad tilt-rotor uav. IFAC Proceedings Volumes, 47(3), 11055-11059.

Holybro Pix32 "PixHawk" Flight Controller Set (2019). Retrieved from https://www.getfpv.com/holybro-pix32-pixhawk-flight-controller-set.html

Jetson Nano Developer Kit (2019). Retrieved from https://developer.nvidia.com/embedded/jetson-nano-developer-kit

Keeney, Tasha. How Can Amazon Charge $1 for Drone Delivery? (May, 2015).

LIDAR-Lite v3 (2019). Retrieved from https://buy.garmin.com/en-US/US/p/557294

Lin, C., Shah, K., Mauntel, L., & Shah, S. (2018). Drone delivery of medications: Review of the landscape and legal considerations. The Bulletin of the American Society of Hospital Pharmacists, 75(3), 153–158. https://doi.org/10.2146/ajhp170196

Loftin, Lawrence K., Jr. (1985). Quest for Performance: The Evolution of Modern Aircraft. United States.

Napolitano, Marcello R. (2012). Aircraft Dynamics: From Modeling to Simulation. Wiley.

Original Airbot 200A PDB Power Distribution Board & 5CM Cable Wire for RC Drone FPV Racing (2019). Retrieved from https://usa.banggood.com/Original-Airbot-200A-PDB-Power-Distribution-Board-5CM-Cable-Wire-for-RC-Drone-FPV-Racing-p-1420470.html?gmcCountry=US&currency=USD&createTmp=1&utm_source=googleshopping&utm_medium=cpc_bgcs&utm_content=frank&utm_campaign=ssc-usg-all-newcustom-1008&ad_id=388194796019&gclid=CjwKCAiA58fvBRAzEiwAQW-hzXVrvJ5EdWU9t0N2ZOPV6jnolPXmcGMP5uz8yq1W2QpZehOHiWosZBoCpWcQAvD_BwE&cur_warehouse=CN

Price wars: counting the cost of drones, planes and satellites (2019). Retrieved from https://droneapps.co/price-wars-the-cost-of-drones-planes-and-satellites/

Ross, P. E. (2018). Iceland's consumers try drone delivery: The startup Aha takes on Amazon with basic drones bearing burgers-[News]. IEEE Spectrum, 55(10), 12-13.

Neutronics: SAE 2020 limiters. (2019). Retrieved from https://neumotors.cartloom.com/storefront/product/24377

Sadraey, M (2012). Aircraft Design: A Systems Engineering Approach. Wiley.

Small Unmanned Aircraft Systems: FAA Should Improve Its Management of Safety Risk. Government Accountability Office. (May 2018). Retrieved from https://www.gao.gov/assets/700/692010.pdf

Stolaroff, J.K., Samaras, C., O'Neill, E.R. *et al.* Energy use and life cycle greenhouse gas emissions of drones for commercial package delivery. *Nat Commun* **9,** 409 (2018). https://doi.org/10.1038/s41467-017-02411-5 Retrieved from: https://www.nature.com/articles/s41467-017-02411-5

Turnigy MultiStar 30A BLHeli-S Rev16 V3 ESC 2~4S (Opto). (2019). Retrieved from https://hobbyking.com/en_us/blheli-s-30a.html

Turnigy nano-tech 2200mah 3S 45~90C Lipo Pack (2019). Retrieved from https://hobbyking.com/en_us/turnigy-nano-tech-2200mah-3s-45-90c-lipo-pack.html?queryID=0fcf46783e560367fbe2ac55f0288f2b&objectID=30641&indexName=hbk_live_magento_en_us_products

Waterman, B. M., Pasculano, B. H., Goldsberry, J. A., Barker, Q., Jack, R., Bergeron, T. P., Weoss, T. M., Zolotarevsky, Z. J. (2019). Vertical Take-off and Landing Autonomous Aircraft Design. (Undergraduate Major Qualifying Project). Retrieved from Worcester Polytechnic Institute Scanned Projects Collection: http://www.wpi.edu/Pubs/E-project/Available/E-project-032119-131229/unrestricted/MQP_Report_Submission.pdf

Wing (2019). Retreated from: https://x.company/projects/wing/

Xu, Jia. (2019). Design Perspectives on Delivery Drones.

Zipline (n.d.) Retrieved from https://flyzipline.com/

6. Appendices

Appendix A: Power Draw Estimates

Table 22: Motor power requirements during various flight regimes

Flight Regime	Horizontal Motor (x1)		Vertical Motor (x4)	
	Power Draw (W)	Current Draw (A)	Power Draw (W)	Current Draw (A)
Takeoff - peak draw	0	0	232	20.9
Takeoff - average draw	0	0	180	16.2
Transition - peak draw	320	28.8	117	10.5
Transition - average draw	262	23.6	80.1	7.22
Hover	0	0	136	12.3
Level Flight	75	6.8	0	0
Turning – min turn radius	158	14.2	0	0

With the above requirements, the maximum motor power requirements are during the peak draw in takeoff, when the motors consume a total of 928 W and draw 83.6 A of current.

Table 23: Net aircraft power requirements

Component	Number of Components	Net Power Draw (W)	Net Current Draw (A)
Jetson Nano	1	10	
Pixhawk Pix32	1	2.5	
Raspberry Pi Cam V2	1	1.25	
LIDAR-Lite 3 Laser Rangefinder	1	0.5	
Servos - HS-5065MG Servo	6	36	
Motors – AT2317	5	928	83.6
Total Requirements		978	83.6
Total Available		1000	90

Appendix B: 2020 WPI UAV Competition Rules

1. Mission Requirements

The aircraft's mission is to take-off from a specified take-off/landing area, deliver payload at a specified target location, and return and land in the take-off/landing area. The aircraft's ability to perform this mission will be scored based on the aircraft's range, maximum payload, accuracy of delivery, autonomy of the mission, and originality of the aircraft design (see scoring metric details in Section 3).

Competing designs are limited to fixed wing aircraft only for Profs Olinger and Jayachandran teams, and rotating wing/blade aircraft for Prof. Cowlagi's team. All parts of the aircraft must be either sourced from salvaged parts of previous WPI projects or purchased through WPI-provided funds for the MQP. Students' personal funds may not be used to purchase any hardware or software parts of the aircraft.

1.1 Venue

The competition will be conducted outdoors and away from the WPI campus, e.g., at an airfield maintained by a model aircraft club or similar airfield. Teams should be prepared to transport the designed aircraft by car to the competition venue. Teams will have the opportunity to scout the venue and/or conduct flight tests at the venue before the day of the competition.

1.2 Payload and Delivery

Payload will be in the form of standard beanbags (Amazon link: https://www.amazon.com/dp/B07DRNLCYD/ref=cm_sw_em_r_mt_dp_U_YSRBDbDN5GMJ5), and must be air-dropped to the target location. Students may not modify the beanbags except by removing some portion of the filling sand, however all sand used as payload weight must be contained in a beanbag. The beanbags used as payload will be weighed just prior to all qualifying and competition flights. The payload beanbags must be fastened together into a single unit for the air-drop. A soft, flexible structure may be used to carry the payload beanbags external to the

aircraft, for example in a ‘sling load’ beneath the aircraft. This structure will count as empty weight (not payload weight).

1.3 Target Demarcation

The target location for payload delivery will be indicated by visibly distinctive markings on the ground. GPS coordinates of the target will be provided, as measured using a typical smartphone GPS receiver, i.e., typical GPS-based localization errors are to be expected. In addition to these two identifiers (visible markings and GPS coordinates), each team will be allowed to place up to one identification aid on the target on the day of the competition. Typical aids include QR codes/April tags, a bright navigation light, and radio beacons. This identification aid must receive approval from the judges no later than January 20, 2019, and must be described in the final project report prior to the day of the competition.

The general airfield layout is shown in the following figure.

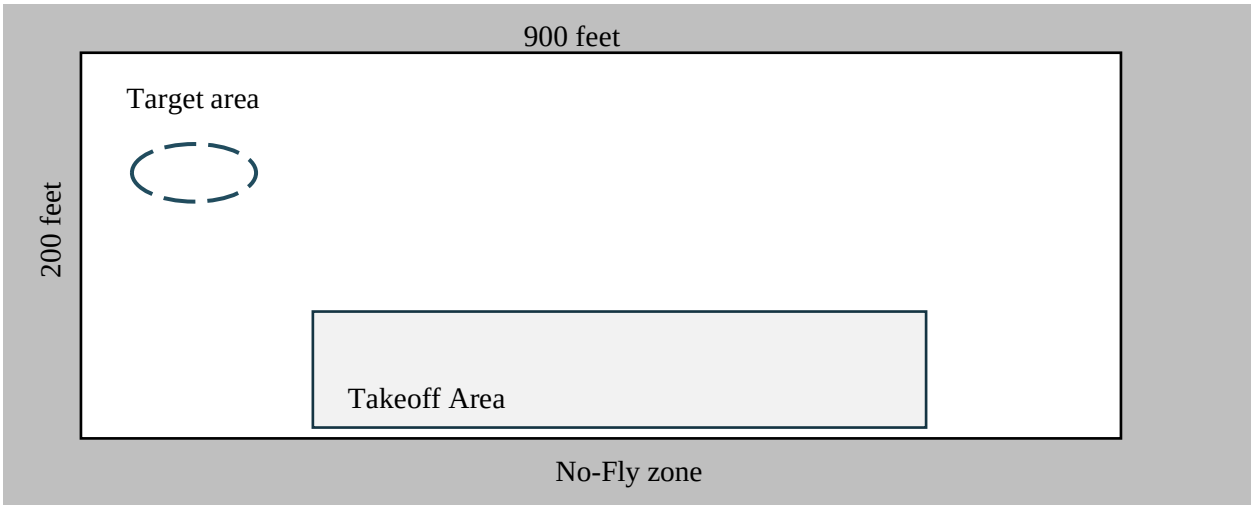

1.4 No-Fly Zones

- Specific no-fly zones will be defined for the competition venue (see figure above).
- At no time will an aircraft enter the no-fly zones, whether under controlled flight or uncontrolled.
- At no time will an aircraft’s altitude exceed 100 m above ground level.
- First infraction for crossing into the no-fly zone will result in an invalidated flight attempt and zero points will be awarded for that flight.

- Second infraction will result in disqualification from the entire event and loss of all points.
- It is the team and team pilot's responsibility to be aware of the venue-specific no-fly zones and to comply with all venue specific rules.
- If a team is unable to directionally control their aircraft and it is headed towards or is in a no-fly zone, the judges may order the pilot to intentionally crash the aircraft to prevent it from endangering people or property. This safety directive must be followed immediately if so ordered.
- GPS coordinates of the corners of the fly zone (green region in the above figure) will be provided.

1.5 Take-off

Allowable methods of take-off include hand launch, ground roll, and catapult launch. The take-off method should account for the possibility of snow cover on the ground. The aircraft must climb to an observable ground clearance (see Section 1.6) by the end of the take-off zone. An aircraft that 'touches down' within the take-off zone after initial launch but still attains this observable take-off ground clearance completes a successful take-off.

1.6 Flight

The aircraft must fly at an observable ground clearance (distance between lowest point on aircraft including external payload and the ground) throughout the flight between take-off and landing. A judge using normal vision standing in the take-off/landing zone must be able to observe this ground clearance OR the team must independently provide clear evidence that this rule is met within 10 minutes after the completion of the flight. A flight will be considered as immediately terminated for scoring purposes the first time this rule is violated outside the take-off/landing zone.

1.7 Landing

- The take-off/landing zone will be visibly marked.
- It is the team and team pilot's responsibility to be aware of the class specific landing zone dimensions at the event site.

- All aircraft must remain within the designated landing zone runway during landing. Any aircraft that leaves their designated landing zone during landing are subject to a penalty of 50% of any points earned during the flight prior to landing.
- Any flight where the aircraft does not make the initial touch down for landing inside the designated landing zone is disqualified and forfeits all points for that flight.
- Any landing where the aircraft is not rolling or sliding on the ground when it leaves the landing zone (i.e., bouncing into the air as it leaves the landing zone) is disqualified. Touch-and-go landings are not allowed and will be judged as a failed landing attempt.
- The criteria for being within the landing zone is that no supporting part of the aircraft that is touching the ground can be outside the landing zone. For example, a wing tip or fuselage is allowed to overhang the edge of the landing zone, as long as no supporting part of the aircraft is physically touching anything outside the landing zone.

1.8 Autonomy

Commercially available systems use? Yes, budget permitting

Autonomous flight may be demonstrated in one or more of the following capabilities of the aircraft while the pilot exerts no remote control. For any of these capabilities to be adjudicated as "autonomous" for any duration of flight, the pilot's hands must remain visible and out of contact with the controls throughout that duration.

1. **Autopilot:** the aircraft maintains steady flight (e.g., constant altitude and/or constant airspeed, or constant rate of climb / descent).

2. **Waypoint guidance:** the aircraft travels through a sequence of spatial waypoints. These waypoints may be specified in terms of geographic coordinates (e.g., latitude-longitude) encoded in software, or indicated on a map through a graphic user interface, or indicated by ground-based markers to be detected by the aircraft during flight.

3. **No-fly zone avoidance:** the aircraft plans and executes maneuvers to avoid no-fly zones. Autonomous traversal along a preplanned sequence of waypoints that already avoid the no-fly zone will not be counted as a demonstration of no-fly zone avoidance capability.

4. **Target detection:** the aircraft detects the target location on the ground using visibly distinctive markings to identify the target.

5. **Payload drop:** the payload is autonomously released from the aircraft without the pilot's manual activation of a switch.

1.9 Originality of Design

Originality of the design will be judged based on differences in overall aircraft configuration compared to WPI SAE micro-aircraft or WPI VTOL drones that have been developed in previous WPI MQP projects or graduate project work.

1.10 On the Day of the Competition

No changes to aircraft except ballast adjustments and replacement of batteries and/or propellers will be allowed after reaching the competition venue on the day of the competition. To qualify for the competition, teams must demonstrate before the day of the competition:

- Take-off and landing (as described in Sections 1.5 and 1.6) and at least one minute of flight time with an empty aircraft.
- Take-off and landing (as described in Sections 1.5 and 1.6) and at least one minute of flight time with half of the design payload (see Section 5.6).

See Section 5.8 for flight test reporting requirements.

1.11 Judges

The faculty advisors on the UAV MQP projects will serve as judges during the flight competition and to interpret competition rules throughout the MQP projects.

2 Design Constraints

2.1 Empty CG

All aircraft must meet the following Center of Gravity (CG) related requirements:

- All aircraft must be flyable at their designated Empty CG position (no payload, ready to fly).

- All aircraft must have the fuselage clearly marked on both sides with a classic CG symbol (below) that is a minimum of 0.5 inches in diameter centered at the Empty CG position (Wing type aircraft may place the two CG markings on the bottom of the wing.)

2.2 Gross Weight Limit

Aircraft gross take-off weight including payload may not exceed 3 kg.

2.3 Controllability

All aircraft must be remotely controllable at all times during flight.

2.4 Radio Control System

The use of a 2.4 GHz radio control system is required for all aircraft. The 2.4 GHz radio control system must have a functional fail-safe system that will reduce the throttle to zero if the radio signal is lost.

2.5 Spinners or Safety Nuts Required

All powered aircraft must utilize either a spinner or a rounded model aircraft type safety nut.

2.6 Metal Propellers

Metal propellers are not allowed.

2.7 Lead is Prohibited

The use of lead in any portion of any aircraft (payload included) is strictly prohibited.

2.8 Payload Distribution

The payload cannot contribute to the structural integrity of the airframe.

2.9 Aircraft Ballast

Aircraft ballast, defined as non-payload weight needed to alter CG location, is allowed with the following conditions:

- Ballast cannot be used in a closed payload bay
- Ballast locations must be clearly indicated on the 2D drawings in MQP report.

- Ballast must be secured so as to avoid shifting or falling off the aircraft, thereby shifting the CG.
- Ballast will not be counted as payload.

2.10 Stored Energy Restriction

Aircraft must be powered by electric motors on board the aircraft. No other internal forms of stored potential energy allowed on the aircraft Stored potential or elastic energy is allowed in a catapult launch mechanism.

2.11 Control Surface Slop

Aircraft control surfaces and linkage must not feature excessive slop. Sloppy control surfaces lead to reduced controllability in mild cases, or control surface flutter in severe cases.

2.12 Servo Sizing

Analysis and/or testing must be described in the Design Report that demonstrates the servos are adequately sized to handle the expected aerodynamic loads during flight.

2.13 Clevis Keepers

All control clevises must have additional mechanical keepers to prevent accidental opening of the control clevis in flight.

2.14 Red Arming Plug

All electric powered aircraft must use a discrete and removable red arming plug to arm and disarm the aircraft propulsion system. This red arming plug must be integrated into the electrical circuit between the battery and the electronic speed controller (ESC).

- The red arming plug must physically be located at 40% to 60% of the aircraft length from the aircraft propeller. This is to allow arming and disarming the aircraft at a safe distance from the propeller.
- The red arming plug must be located on top of the fuselage or wing and external of the aircraft surface.
- The location of the red arming plug must be clearly visible.

- The non-removable portion of the arming plug interface may not have more than one male lead.
- Disconnecting wiring harnesses to arm and disarm a system will not be allowed.

2.15 Battery Protection

- All batteries in the aircraft must be positively secured so that they cannot move under normal flight loads.
- The battery bay or location in the aircraft must be free of any hardware or other protrusions that could penetrate the battery in the event of a crash.

2.16 Power Limiter

All aircraft must use a 1000 W power limiter such as the one available here: https://neumotors.cartloom.com/storefront/product/24377.

2.17 Aircraft Systems Requirements

- Propulsion requirements: aircraft are restricted to electric motor propulsion only.
- Propeller and gearbox: gearboxes on an aircraft where the propeller RPM differs from the motor RPM are allowed. Multiple motors, multiple propellers, propeller shrouds, and ducted fans are allowed.
- The aircraft should use Lithium Polymer batteries. The maximum size propulsion system battery allowed is a 3-cell 2200 mAh lithium polymer battery. Batteries having fewer cells and lower capacity are permitted.
- Gyroscopic assist and other forms of stability augmentation are allowed.
- Aircraft empty weight definition: All aircraft parts that are not payload contribute to the empty aircraft weight, including, but not limited to: airframe, receiver, electronics, batteries, hardware, brackets, straps and other associated features.

3 Scoring Metric

To receive a score on the day of the competition, teams must demonstrate the following flight sequence: take-off, complete range leg (flight time t_{flight} from take-off to drop used in scoring equation), drop payload, return and land. The flight score S is given by the following

equation. The highest flight score among at most three attempts on the day of the competition will be considered.

$$Score = \lambda_1 \frac{W_{payload}}{W_{empty}} t_{flight} v_{avg} + \lambda_2 \Delta + \lambda_3 \sum_n A_n + P$$

Symbol Meaning

$W_{payload}$, W_{empty}: Weight of the payload carried by the aircraft and of the aircraft without payload, respectively

t_{flight}: Time of flight in range leg in secs

V_avg: Average groundspeed during flight, computed using onboard GPS-based speed measurements in meters/sec.

Δ: Define δ to be the distance between the target location and actual payload drop point. Then

$$\Delta = \begin{cases} 1, 0 < \delta < 1\,m \\ 0, 1\,m \leq \delta < 3.5m \\ -1, 3.5m < \delta \end{cases}$$

A_n: Points for demonstrating autonomy capabilities n = 1...,5 (see Section 1.8)

$$A_1 = A_2 = A_5 = 1, A_3 = 3, A_4 = 5.$$

P Originality points on a scale of $0 - 10$.

λ_i: Constants $\lambda_1 = 0.01$, $\lambda_2 = 35$, and $\lambda_3 = 35$.

4 Operational Safety Requirements

4.1 Ground Safety and Flight Line Safety Equipment

- No open toe shoes allowed. All team participants, including faculty advisors and pilots, will be required to wear closed-toe shoes during flight testing and during flight competition.
- All students involved at the flight line launching aircraft must wear safety glasses and hard hats.

- The University name must be clearly displayed on the wings or fuselage.
- The University initials may be substituted in lieu of the University name provided the initials are unique and recognizable.

4.2 Team Pilots

All pilots must be current members of the Academy of Model Aeronautics or the Model Aircraft Association of Canada (AMA has an agreement with MAAC).

A current WPI student who meets this requirement is available to MQP teams. If an MQP student on a team is an experienced RC pilot and AMA member, they can serve as the pilot. However, MQP teams should not plan on training an inexperienced student.

4.3 Aircraft Configuration during Flight

The aircraft must remain intact during a flight attempt to receive full flight score. A flight attempt includes activities at the starting line, the take-off roll, takeoff, flight, landing and recovery after landing.

A 25% deduction from the flight score will be assessed if any of the following items are observed to completely detach from the aircraft during a flight attempt.

- Stickers
- Tape
- Coverings

With the exception of a broken prop during landing, if any other components fall off the during a flight attempt, the flight will be disqualified.

5 Reporting Requirements

5.1 2D Drawing Requirements

Updated 2D drawings should be provided by each team to faculty advisors periodically throughout the project and in all draft MQP report submissions.

5.2 2D Format and Size

The 2D drawing must be ANSI B sized page (PDF) format (11 x 17 inches). The drawing shall consist of one (1) page.

5.3 Views Required

Drawings shall include at a minimum, a standard aeronautical 3-view orthographic projection arranged as described:

- Left side view, in lower left, with nose pointed left.
- Top view, above and aligned with the left side view, also with nose pointed left (wing-span break-view permitted).
- Front view aligned to side view, located in the lower right (projection view nonstandard movement as noted by projection view arrows in accordance with ANSIY14.5M 1994).

5.4 Dimensions Required

Drawing dimensions and tolerance shall be in SI units, decimal notation accordance with ANSI-Y14.5M 1994 to an appropriate level of precision to account for construction tolerances (allowable variation from analyzed prediction to account for fabrication) (i.e. X.X = ± .1 cm; X.XX = ± .03 cm; X.XXX = ± .010 cm). The minimum required dimensions/tolerances are: Aircraft length, width, and height.

5.5 Summary Data Required

The drawing shall contain a summary table of pertinent data to include but not limited to:

- Wingspan
- Empty weight
- Battery(s) capacity
- Motor make and model
- Motor KV (micro and Regular Class only)
- Propeller manufacturer, diameter, and pitch
- Servo manufacturer, model number and torque specification in ounce-inches for each servo used on the aircraft. Identify servo being used at each position on the aircraft.

5.6 Weight and Balance Information

The 2D drawing shall contain the following weight, balance and stability information:

- A clearly marked and labeled aircraft datum.
- A weight and balance table containing pertinent aircraft equipment. Each item listed must show its location from the aircraft datum in centimeters (the moment arm), the force, and resultant moment. The minimum list of pertinent equipment includes:
    - Motor
    - Battery(s)
    - Payload
    - Ballast (if used)
    - Electronics

    • Design maximum payload, and design payload for maximum range

- Aircraft mean aerodynamic chord, stability margin and CG information listed below must be clearly shown on drawing:
    - Aircraft mean aerodynamic chord
    - Stability margin for loaded CG and empty CG
    - Empty CG location (flightworthy)
    - Fully loaded CG (flightworthy, with payload, if applicable)

5.7 Tech Data Sheet: Weight Buildup

Updated Weight Buildup List should be provided by each team to faculty advisors periodically throughout the project and in all draft MQP report submission.

The Micro Class Weight & Balance Build-up List will help teams understand the importance of managing aircraft weight to achieve safety of flight at the desired payload fraction. Each team shall supply a one (1) sheet summary list of aircraft parts, part weight, and part weight percentage) that contribute to the overall empty weight of the aircraft.

5.8 Flight Tests

A flight test is an experiment conducted to study/demonstrate the real-world characteristics of an aircraft. For this competition, flight test evidence must be recorded by both of the following means:

- Video recorded from the ground.
- Inertial measurements recorded from an onboard inertial measurement unit. The following quantities must be recorded: body-axis angular velocities, body-axis accelerations, angular orientations, GPS position, GPS velocity.

In addition, optionally, video from an onboard camera may be recorded. Any flight experiment with only video evidence (i.e., inertial measurements log absent) will not be considered for reporting or qualifying requirements.

An unpowered glide flight test is required for the B-term MQP report. In addition, the following flight tests are required for a team to qualify for the competition:

- Take-off and landing (as described in Sections 1.5 and 1.6) and at least one minute of flight time with an empty aircraft.
- Take-off and landing (as described in Sections 1.5 and 1.6) and at least one minute of flight time with half of the design payload.

Appendix C: Hover Test Information

Video URL: https://www.youtube.com/watch?v=GDmhadpi9Gs

https://www.youtube.com/watch?v=qs5EfVxxM5U&feature=youtu.be

https://www.youtube.com/watch?v=U_KxrMokt_Q&feature=youtu.be

Testing Procedure

1. The circuit between the battery and the rest of the aircraft was completed. As the arming plug was not yet obtained when this test was initially performed, this action instead involved simply plugging the battery into the power limiter.
2. The safety switch on the GPS modules was pressed to arm the system. It was made sure that no one was close to the aircraft and that the aircraft was in "QSTABILIZE" before proceeding. This is essentially a manual control mode where the flight controller is not trying to hold position.
3. The aircraft throttle was slowly increased until the aircraft took off. The throttle was then adjusted until the aircraft was hovering less than a meter off the ground.
4. Altitude was maintained for approximately 15(?) seconds before the throttle was lowered again to allow the aircraft to touchdown. If the attitude of the aircraft began to differ significantly from a level hover (for example, if a significant spin about the yaw axis was observed), this touchdown was performed earlier.
5. If the previous hover was successful (i.e. it was not aborted early due to an attitude issue), steps 3 and 4 were repeated, increasing the target altitude by 1 meter each time until the cruise altitude of 6 meters was reached.

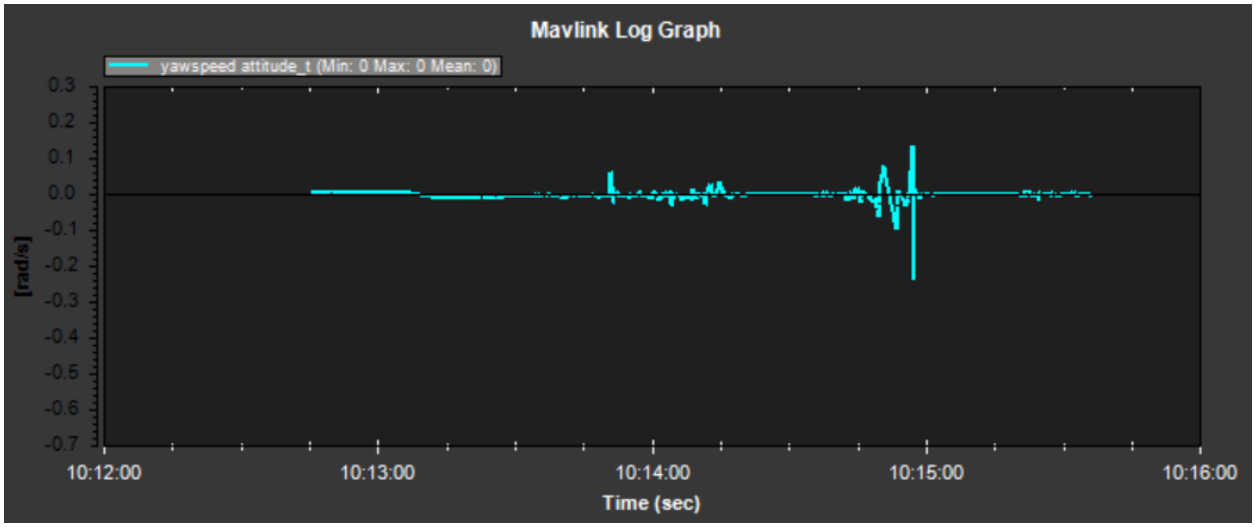
Mavlink Log Graph
yawspeed attitude_t (Min: 0 Max: 0 Mean: 0)
[rad/s]
0.3
0.2
0.1
0.0
-0.1
-0.2
-0.3
-0.4
-0.5
-0.6
-0.7
10:12:00
10:13:00
10:14:00
10:15:00
10:16:00
Time (sec)

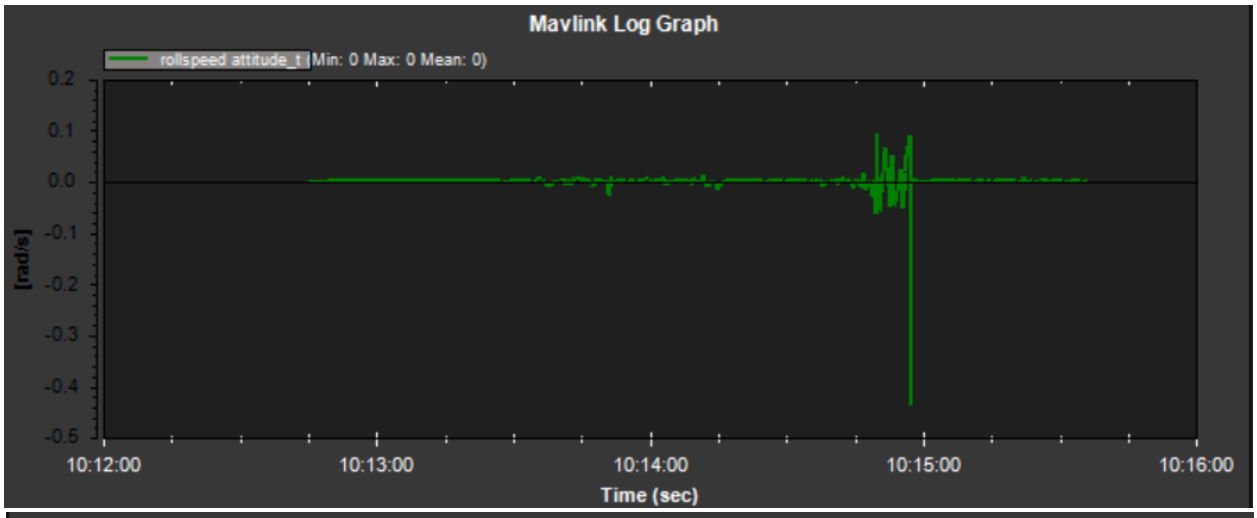
Mavlink Log Graph
rollspeed attitude_t (Min: 0 Max: 0 Mean: 0)
[rad/s]
0.2
0.1
0.0
-0.1
-0.2
-0.3
-0.4
-0.5
10:12:00
10:13:00
10:14:00
10:15:00
10:16:00
Time (sec)

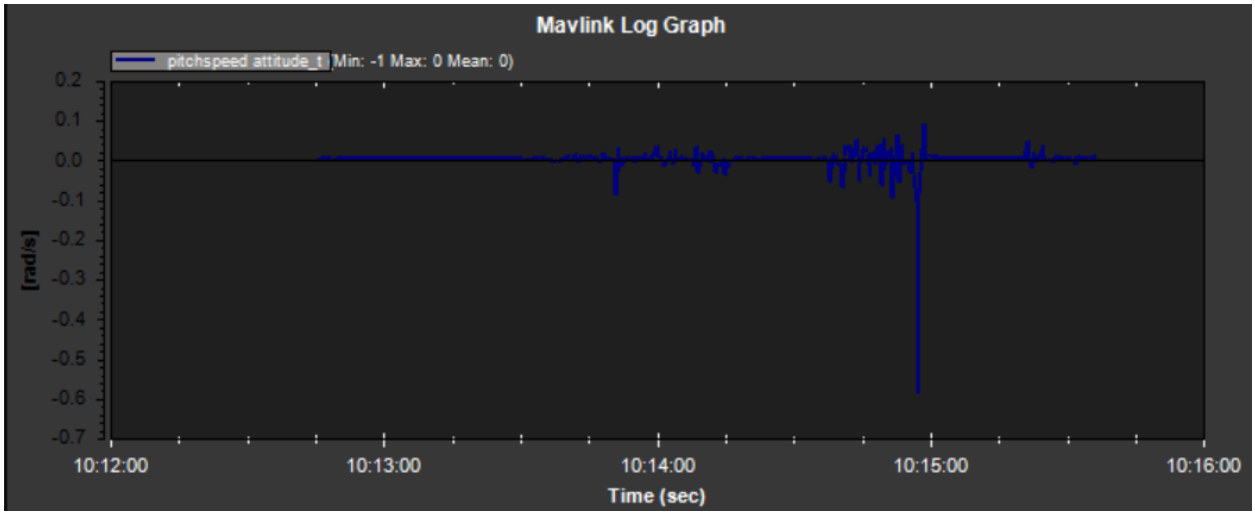
Mavlink Log Graph
pitchspeed attitude_t (Min: -1 Max: 0 Mean: 0)
[rad/s]
0.2
0.1
0.0
-0.1
-0.2
-0.3
-0.4
-0.5
-0.6
-0.7
10:12:00
10:13:00
10:14:00
10:15:00
10:16:00
Time (sec)

Appendix D: Bench Test Information

Fly-By-Wire Transition

url: https://www.youtube.com/watch?v=15f-wnz_O98&feature=youtu.be